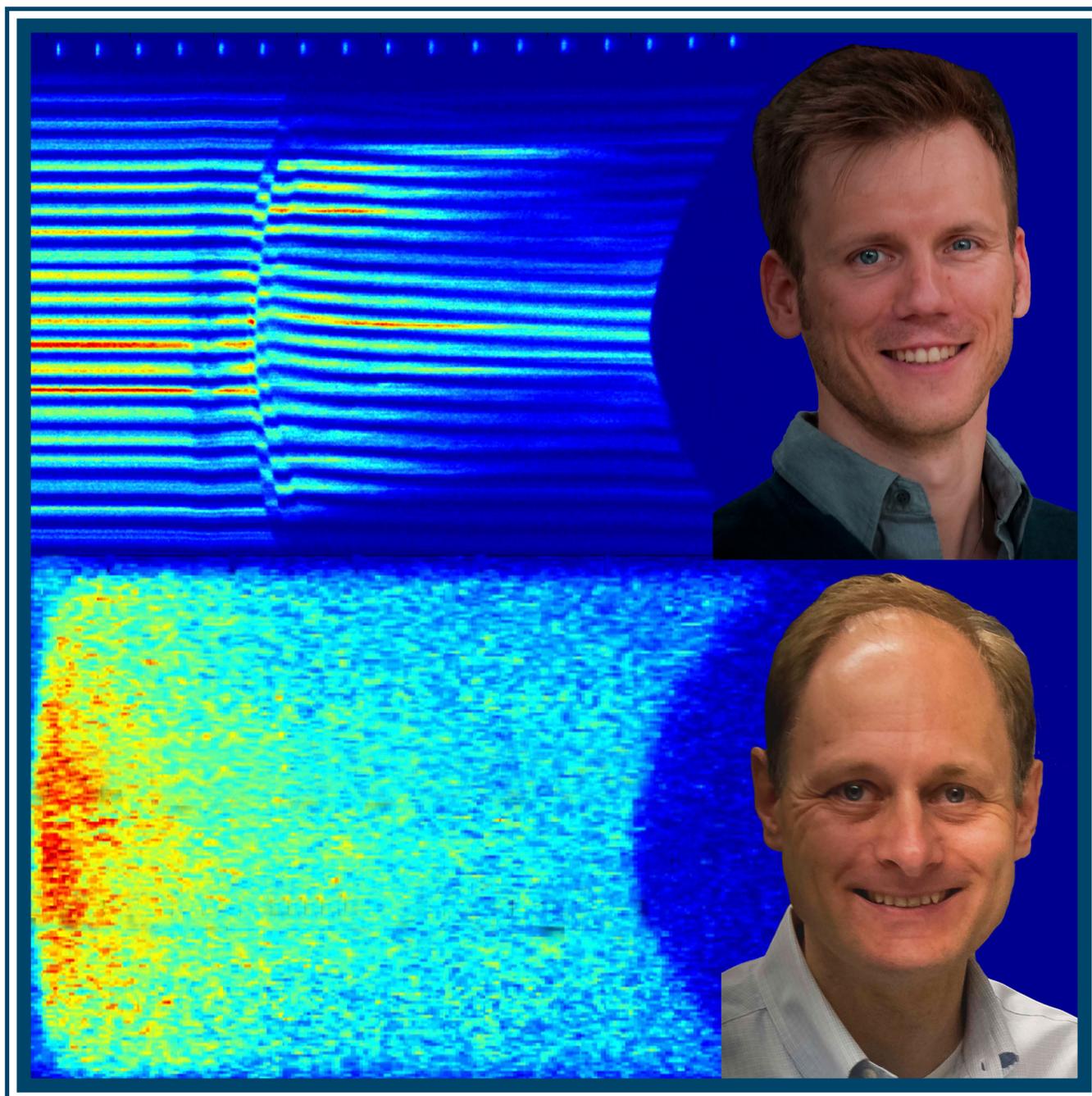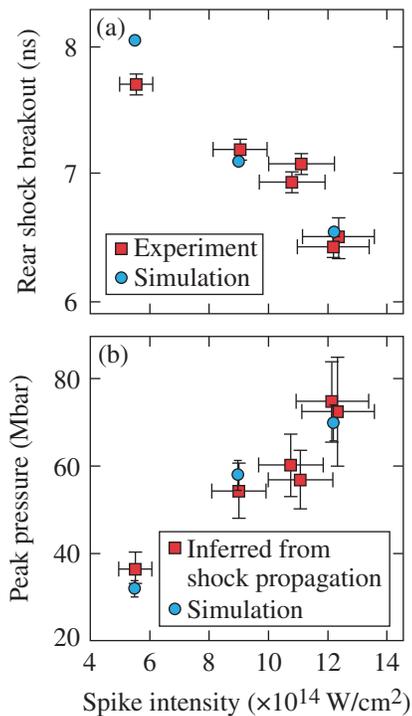# LLE Review

Quarterly Report

UR
LLE

About the Cover:

E20784JR

The cover photo highlights LLE's scientists Dr. Matthias Hohenberger and Dr. Wolfgang Theobald, who have led shock-ignition (SI) experiments on the OMEGA Laser System. In contrast to the conventional central-hot-spot–ignition concept, shock ignition separates the fuel-assembly and ignition stages by using shaped high-intensity laser spikes at the end of the compression pulse. The ablatively driven strong shock of a few hundred Mbar, launched by the high-intensity spike, converges in the central hot spot of the fusion capsule and raises the hot-spot pressure to ignition conditions. To explore the viability of this ignition scheme, it is essential to understand how strong shocks can be generated in long-scale-length plasmas by high-intensity laser spikes. The article on p. 137 presents experimental and simulation results on strong-shock generation with planar targets closely relevant to the SI concept. The background of the photo shows an example of experimental data from the velocity interferometer system for any reflector (VISAR) and streaked optical pyrometer (SOP) diagnostics.

The figure shows (a) the experimental data for shock break-out time at the rear surface of a planar target (squares) in comparison with radiation–hydrodynamic simulations (circles) and (b) the inferred peak pressure as a function of the laser spike intensity. Based on these results, at an intensity of 1.2×10^{15} W/cm^2, a 70-Mbar shock was generated in the presence of a 350-μm pre-plasma. This is the highest pressure reported at SI-relevant conditions and an important step toward experimentally validating the SI concept.

LLE Review

Quarterly Report

UR
LLE

Contents

In Brief

This volume of the LLE Review, covering April–June 2012, features "Shock-Ignition Experiments with Planar Targets on OMEGA" by M. Hohenberger, W. Theobald, S. X. Hu, K. S. Anderson, R. Betti, T. R. Boehly, M. Lafon, T. C. Sangster, W. Seka, C. Stoeckl, and B. Yaakobi (LLE); D. D. Meyerhofer, (LLE and Departments of Mechanical Engineering and Physics, University of Rochester); A. Casner (CEA); D. E. Fratanduono (LLNL); and X. Ribeyre and G. Schurtz (Université Bordeaux). In this article (p. 137), the authors report on strong-shock generation in the presence of pre-plasmas with relevance to shock ignition using the OMEGA Laser System. A planar target was irradiated with a laser pulse consisting of a pre-plasma–generating foot followed by a high-intensity spike, driving a strong shock into the target. The observed shock dynamics inferred from VISAR (velocity interferometer system for any reflector) and SOP (streaked optical pyrometer) measurements have been reproduced well using two-dimensional (2-D) *DRACO* simulations, indicating the generation of plastic-ablator shocks of up to 70 Mbar.

Additional highlights of research presented in this issue include the following articles:

- S. P. Regan, P. B. Radha, S. X. Hu, T. R. Boehly, and T. C. Sangster (LLE); D. D. Meyerhofer (LLE and Departments of Mechanical Engineering and Physics, University of Rochester); K. Falk, G. Gregori, and C. D. Murphy (University of Oxford); B. Crowley (AWE); S. H. Glenzer, O. L. Landen, and T. Doeppner (LLNL); and D. O. Gericke and J. Vorberger (Warwick University) report on the first x-ray Thomson-scattering (XRTS) measurement of shock-compressed liquid deuterium at Fermi-degenerate plasma conditions (p. 143). The noncollective, spectrally resolved, inelastic XRTS employs Cl Ly_α line emission at 2.96 keV. The microscopic property measurements of shocked deuterium show an inferred spatially averaged electron temperature of 8±5 eV, an electron density of 2.2×10^{23} cm^{-3}, and an ionization of 0.8 (–0.25, +0.15). Two-dimensional hydrodynamic simulations using equation-of-state models suited for the extreme parameters also occurring in inertial confinement fusion (ICF) research and planetary interiors are consistent with experimental results.

- H. P. Howard, A. F. Aiello, J. G. Dressler, N. R. Edwards, T. J. Kessler, A. A. Kozlov, I. R. T. Manwaring, K. L. Marshall, J. B. Oliver, A. L. Rigatti, A. N. Roux, A. W. Schmid, N. P. Slaney, C. C. Smith, B. N. Taylor, and S. D. Jacobs summarize a low-temperature chemical-cleaning approach developed to remove manufacturing residues from multilayer-dielectric (MLD) pulse-compressor gratings to be used on the OMEGA EP Laser System (p. 149). The method strips baked-on photoresist, metal contaminants, and debris without damaging the grating's delicate surface structure. Because targeted cleaning steps remove specific families of contaminants (heavy organics, light organics, metals, and oxides), the process can be adjusted to strip known quantities and types of material. The technique was optimized to clean hafnia/silica MLD gratings manufactured with a bottom antireflective coating (BARC)—a hardened organic polymer layer that is especially difficult to remove. After cleaning, grating samples showed excellent performance in short-pulse (10-ps) laser-damage testing at 1054 nm. Average in-air damage thresholds were 4.06±0.19 J/cm^2 and 3.32±0.22 J/cm^2 (beam normal) in the 1-on-1 and *N*-on-1 regimes, respectively, for a set of nine gratings cleaned at processing temperatures in the range 40°C to 70°C. Post-cleaning diffraction efficiencies were consistently above 96%.

- L. Gao, P. M. Nilson, I. V. Igumenshchev, S. X. Hu, J. R. Davies, C. Stoeckl, D. H. Froula, and R. Betti, (LLE); D. D. Meyerhofer (LLE and Departments of Mechanical Engineering and Physics, University of Rochester); and M. G. Haines (Imperial College) describe the measurement of magnetic fields induced by Rayleigh–Taylor (RT) instability in planar plastic foil with ultrafast proton radiography (p. 159). Thin plastic foils were irradiated with ~4-kJ, 2.5-ns laser pulses focused to an intensity of ~10^{14} W/cm^2. Target modulations were seeded by laser nonuniformities and amplified during target acceleration by RT instability. The experimental data show the hydrodynamic evolution of the target and the generated MG-level magnetic fields in the broken foil, which are in good agreement with predictions from 2-D magnetohydrodynamic simulations.

- C. J. Forrest, P. B. Radha, V. Yu. Glebov, V. N. Goncharov, J. P. Knauer, A. Pruyne, M. Romanofsky, T. C. Sangster, M. J. Shoup III, and C. Stoeckl (LLE); D. T. Casey, and M. Gatu-Johnson (MIT); and S. Gardner (Constellation Energy Nuclear Group) report on the high-resolution spectroscopy that is used to measure ICF neutron spectra to infer the areal density (ρR) of cryogenic DT implosions on OMEGA (p. 165). Neutron time-of-flight (nTOF) techniques were used to measure the spectrum of neutrons that elastically scatter off the dense deuterium (D) and tritium (T) fuel. High signal-to-background data have been recorded on cryogenic DT implosions using a well-collimated, 13.4-m line of sight and an nTOF detector with an advanced liquid scintillator compound. An innovative method to analyze the elastically scattered neutron spectra was developed using well-known cross sections of the D–T nuclear reactions. The measured areal densities are consistent with alternative ρR measurements and 1-D simulations.

- D. T. Michel, A. V. Maximov, R. W. Short, S. X. Hu, J. F. Myatt, W. Seka, A. A. Solodov, B. Yaakobi, and D. H. Froula report on experimental demonstration of the two-plasmon–decay (TPD) common-wave process (p. 172). The total energy in hot electrons produced in a planar target was measured to be the same when using one or two laser beams and significantly reduced with four beams for a constant overlapped intensity. This is caused by multiple beams sharing the same common electron plasma wave in the TPD instability. A model, consistent with the experimental results, predicts that multiple laser beams can drive a resonant common TPD electron plasma wave only in the region of wave numbers bisecting the beams. In this region, the gain is proportional to the intensity of overlapped laser beams.

- J. Katz, R. Boni, C. Sorce, R. Follett, M. J. Shoup III, and D. H. Froula describe a reflective optical transport system for ultraviolet Thomson scattering from electron-plasma waves on OMEGA (p. 178). A Schwarzschild objective that uses two concentric spherical mirrors coupled to a Pfund objective provides diffraction-limited imaging across all reflected wavelengths. This enables the operator to perform Thomson-scattering measurements of ultraviolet (0.263-μm) light scattered from electron plasma waves.

Suxing Hu
Editor

Shock-Ignition Experiments with Planar Targets on OMEGA

In inertial confinement fusion (ICF), a capsule containing cryogenic deuterium–tritium fusion fuel is rapidly compressed to high temperatures and areal densities sufficient for thermonuclear fusion. If the α particles generated via D–T fusion reactions in the central hot spot of an imploded capsule deposit their energy in the compressed core, the capsule ignites. Provided the confinement time determined by the fuel-mass inertia is sufficiently long, the energy released via the fusion burn can exceed the incident driver energy and the fusion gain exceeds unity. The demonstration of this concept is the main goal of ICF research.[1] In laser-driven ICF the compression drive is provided by coupling laser energy into an ablator surrounding a spherical fuel capsule, either directly through symmetric irradiation of the fusion target or indirectly via a thermal x-ray bath generated from laser illumination of the inner walls of a cavity (hohlraum). In the shock-ignition (SI) concept,[2] the fuel-assembly and ignition stages are separated by using shaped, nanosecond laser pulses. During the compression stage of the laser, the fuel is assembled to a high areal density (ρR) at sub-ignition velocity, resulting in a central hot-spot temperature insufficient for ignition. A high-intensity laser spike at the end of the assembly pulse then launches a strong shock wave, the timing of which is such that the return shock, caused by the rising hot-spot pressure, collides with the strong shock inside the fuel.[3] This results in two new shocks, one of which propagates inward, heating and compressing the hot spot to ignition conditions and causing a *non-isobaric* pressure profile peaked at the center. This is energetically favorable compared to the *isobaric* distribution in conventional hot-spot ignition, where both hot spot and fuel are compressed to the same pressure p_{iso}, and is a key advantage of shock ignition. It can be shown that the energy required to achieve shock ignition decreases as $\sim(p/p_{iso})^3$, where the non-isobaric hot-spot pressure p directly depends on the initial laser-driven shock strength at the ablator and its amplification through spherical convergence in the fuel.[4]

Taking full advantage of the SI scheme requires laser-generated shocks at the ablator of ~300-Mbar, launched in the presence of a long-scale-length pre-plasma generated by the assembly laser pulse. For such strong shocks, on-target intensities exceeding 10^{15} W/cm^2 are necessary and laser–plasma instabilities (LPI's) play an important role in the coupling of laser energy to the target. These lead to energy losses through stimulated Raman and Brillouin scattering (SRS and SBS, respectively) and hot-electron generation and potential fuel preheat by fast electrons produced through SRS and two-plasmon decay. Hot electrons are predominantly generated by the laser spike late in the target evolution when the areal density grows rapidly. Provided the electron stopping distance is within the shell thickness, they can even augment the ignitor shock strength and enhance the target performance.[5]

The idea of separating fuel assembly and ignition is conceptually similar to fast ignition.[6] For SI, however, complicated cone-in-shell targets are not necessary, and SI can use the pulse-shaping capabilities of existing facilities designed for hot-spot ignition rather than requiring an additional short-pulse, multipetawatt ignitor laser. This significantly relaxes the technical and financial constraints on fielding this concept experimentally or in a fusion-energy context.

SI has received considerable attention as an alternative path to ignition, e.g., for the National Ignition Facility,[7] HiPER,[8] and the LMJ project.[9] Theoretical studies have investigated target design and robustness,[10] but only a few experimental studies have been performed. Preliminary work on the OMEGA Laser System[11] using warm, spherical plastic targets driven by a SI-type laser pulse showed ~30% higher ρR, larger neutron yields, and better implosion stability than hydrodynamic- and energy-equivalent implosions without a high-intensity shock spike.[4]

This article presents experimental results on LPI and laser-driven shock propagation in planar geometry and at SI-relevant intensities performed using OMEGA. To infer initial shock properties, the data are compared to two-dimensional (2-D) radiative–hydro-dynamic simulations that show very good agreement with the experiment. Based on the numerical results, the experiment discussed here represents the first demonstration of a laser-driven, 70-Mbar shock in the presence of a long-scale-length pre-plasma.

Figure 131.1(a) shows a schematic of the experimental setup. The planar targets consisted of three layers: a 40-μm plastic ablator onto which the laser was focused, followed by 30 μm of Mo and 140 μm of SiO_2. The Mo was used to shield hot electrons from propagating into the final layer and to infer the hot-electron population through time-integrated recording of the Mo-K_α emission with an absolutely calibrated x-ray spectrometer. The final SiO_2 layer was used to observe the shock temperature through streaked optical pyrometry (SOP)[12] and the shock propagation via two VISAR (velocity interferometer system for any reflector) diagnostics with different velocity responses (10.4 and 6.4 μm/ns/fringe) (Ref. 13). Since the Mo is opaque to optical wavelengths, the laser-driven shock could be observed only after entering the SiO_2 layer. The quartz also acted as a "get-lost" layer that prevented refluxing of hot electrons in the Mo. In addition, a CH washer was attached to the front of the target to stop diffracted laser light from hitting the target's sides and to stop electrons from streaming around the target. Further diagnostics included a four-channel, time-resolved, hard x-ray detector that measured the hot-electron temperature[14] and backscattering diagnostics that determined SRS and SBS levels within the focal cone of two beams in the strong-shock drive as well as one location between two strong-shock beams.[15]

Figure 131.1(b) shows an example for the temporal on-target intensity profile of the 351-nm-wavelength laser light at the position of the unperturbed target surface. With an on-target energy between ~5 kJ and 7.2 kJ, the total irradiation profile [dashed line in Fig. 131.1(b)] was achieved by stacking three laser cones in time with individual focusing parameters. Beam smoothing was achieved with polarization smoothing[16] and distributed phase plates (DPP's).[17] Beams in Cones 2 and 3 (blue and green, respectively) were focused to a 1/e intensity radii of 412 μm and 310 μm, respectively, using "SG8" and defocused "SG4" DPP's. These two cones formed a pre-plasma for ~1.6 ns, while the overlap between Cones 1 (red) and 2 provided the high-intensity spike driving a strong shock into the target. Beams in Cone 1 were focused to a 302-μm radius using defocused "IDI300" DPP's. Cone 3 consisted of eight beams at an incidence angle of 62.3°; Cones 1 and 2 comprised six spatially overlapping beams at 23.4° and 47.8°, respectively. While Cones 2 and 3, and therefore the pre-plasma conditions, were kept the same throughout the experiment, the energy contained in Cone 1 was varied to give an overlapped "spike intensity" ranging from ~0.6 to 1.4 $\times$ 10^{15} W/cm^2.

Results for the hot-electron temperature and population as a function of the nominal spike intensity are displayed in
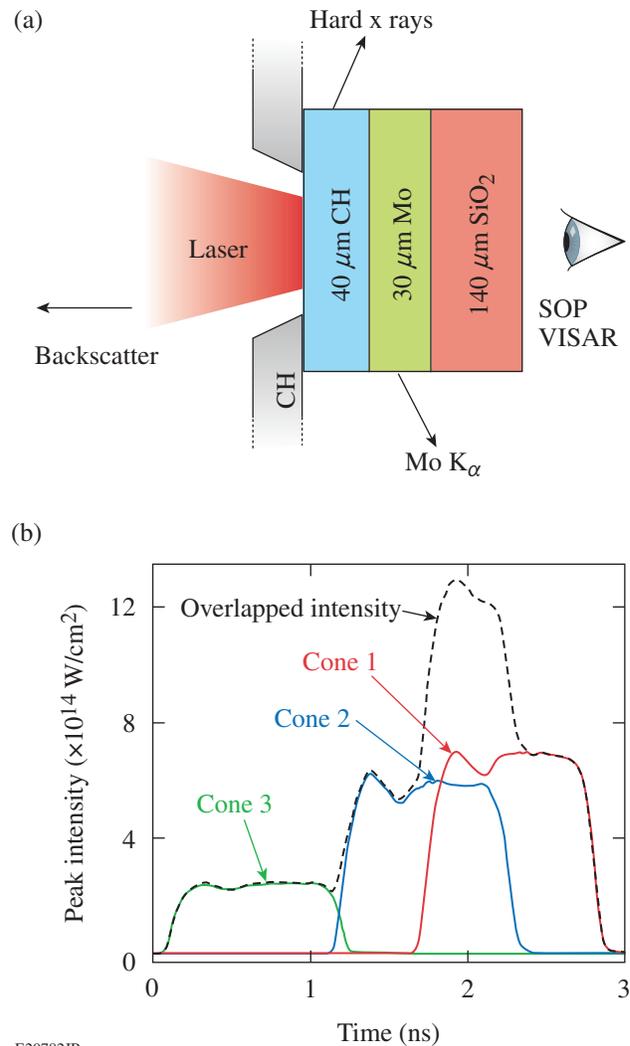
Figure 131.1
(a) Schematic of the planar target driven by a laser pulse as shown in (b). The pulse was generated by stacking three laser cones in time and space, each with its own energy and focusing parameters. SOP: streaked optical pyrometry; VISAR: velocity interferometer system for any reflector.

Fig. 131.2. The electron temperature [Fig. 131.2(a)] rises with intensity, indicating an increase in LPI, and reaches a peak of ~70 keV at the highest-intensity case considered here. The total energy in the hot-electron component [Fig. 131.2(b)] was inferred from comparing the time-integrated Mo-K_α yield to Monte Carlo simulations.[18] The emission of hard x rays was strongly correlated to the high-intensity spike of the drive laser. Therefore, the hot-electron conversion efficiency, plotted on the right y axis of Fig. 131.2(b), is given by comparing the energy contained in the hot-electron component to that in the laser spike, i.e., the energy incident on target during the overlap between Cones 1 and 2. As expected, it increased with
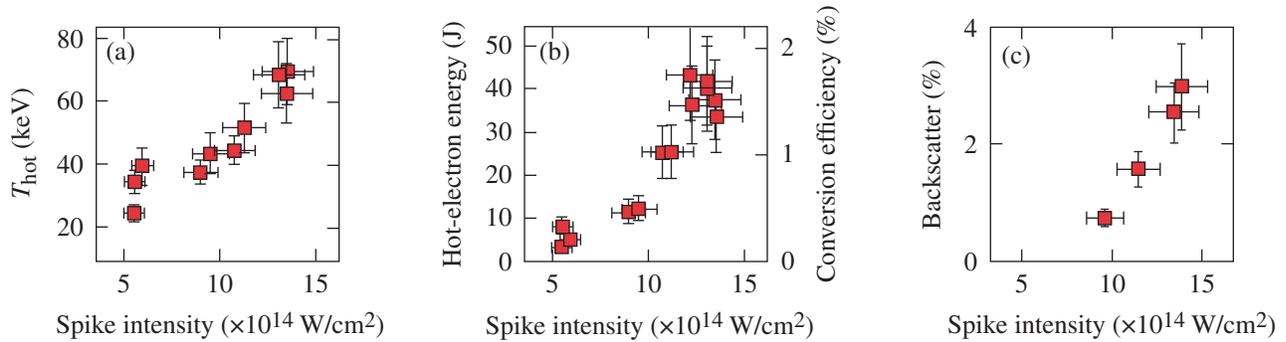
E20783JR

Figure 131.2
(a) Hot-electron temperature as a function of peak laser intensity; (b) laser conversion efficiency and total energy contained in the hot-electron component; (c) fraction of backscattered laser energy (SRS + SBS) within the strong-shock beam cones as a function of peak intensity.

rising intensity, and at the highest intensity, 1.8% of the spike energy was converted to hot electrons. The error bars in these data are dominated by the precision of the measured K_α yield (~25%) (Ref. 18).

Results for the backscattered laser light (SRS and SBS) within the shock-beam focal cones are plotted as a function of peak intensity in Fig. 131.2(c). This also increased with incident intensity, reaching ~3% for the highest-intensity case. Sidescatter was also observed but was not fully quantified and is not included in Fig. 131.2(c). Since the light reflection is nonuniform, and there are too few diagnostics to infer a full scattering profile, so the interpretation of the data with respect to a total backscattered energy in these planar experiments is difficult. The sidescatter is not expected to exceed the in-beam scattering, giving an upper limit for the total amount of scattered light of ~10% at 1.4×10^{15} W/cm^2.

Examples for shock-evolution data obtained with VISAR and SOP diagnostics are shown in Figs. 131.3(a) and 131.3(c),
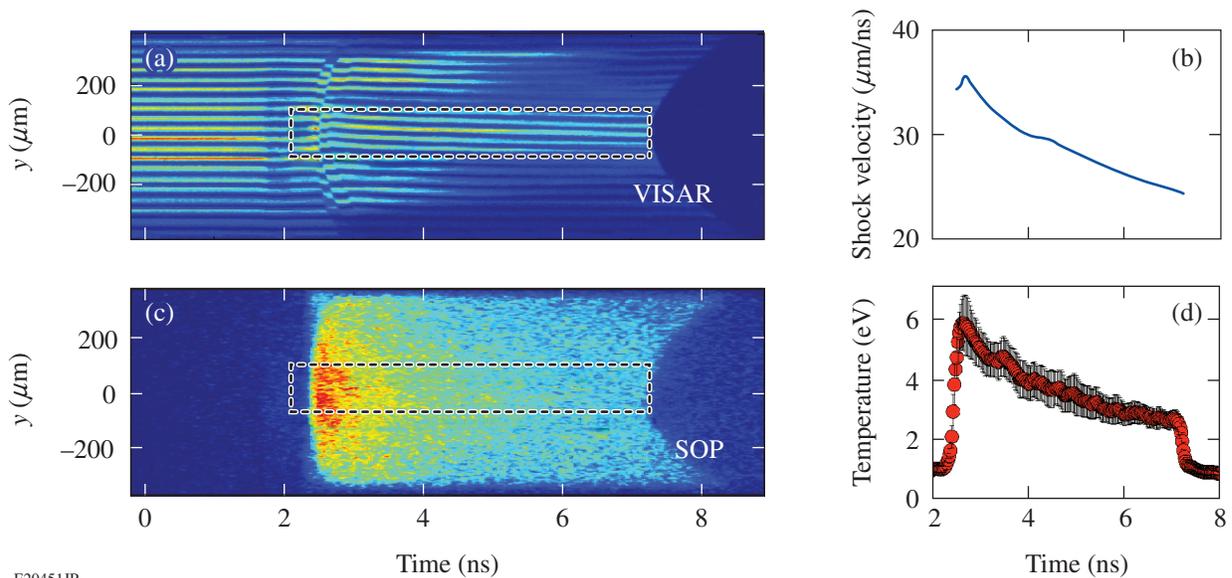
E20451JR

Figure 131.3
Experimental shock-propagation data obtained with (a) VISAR and (c) SOP at a peak intensity of 9×10^{14} W/cm^2; (b) and (d) show extracted shock velocity and temperature, respectively.

respectively. These data were taken with a spike intensity of $\sim 9 \times 10^{14}$ W/cm^2, and all figures are plotted as a function of time with $t = 0$ corresponding to the onset of the laser pulse [see Fig. 131.1(b)]. The slight drop in signal strength of the VISAR data at $\sim$1.7 ns is caused by the laser spike hitting the target. This results in the generation of hot electrons, some of which reach the SiO$_2$ layer and alter the refractive index of the material through ionization, causing partial absorption of the probe laser. Since the Mo layer is opaque, no shock front can be observed until its breakout from the Mo into the SiO$_2$ at $\sim$2.5 ns. This causes a strong fringe shift in the VISAR and a signal onset in the SOP. The subsequent slowly varying fringe shift in Fig. 131.3(a) is indicative of a decelerating shock. At $\sim$7.2 ns the shock breaks out into vacuum through the rear of the target, as evidenced by the pronounced signal drop in both data sets. The shock is strongest and fastest in the center, where the drive laser's intensity is at its peak, and edge rarefactions cause a strong curvature of the shock front and the breakout feature. These data can be used to extract a shock velocity in the range of 30 μm/ns [Fig. 131.3(b)] and an emission temperature of a few eV [Fig. 131.3(d)] inside the SiO$_2$ layer.

The incident laser pulse launched multiple shocks into a target, but the primary goal was to characterize the strong shock driven by the high-intensity spike. The conditions inside the ablator cannot be observed directly. Instead, the strong shock's initial conditions were inferred by matching numerical simulation results to the experimental data. For this purpose the 2-D radiative hydrocode *DRACO* was used[19] Note that a 2-D treatment is strictly necessary as evidenced by the curvature of the rear shock-breakout feature in Figs. 131.3(a) and 131.3(c). Figure 131.4 shows snapshots of the pressure distribution from a simulation using the experimental conditions for the data in Fig. 131.3. The x axis denotes the target's thickness; the y axis is the lateral extent of the target. The simulations assumed azimuthal symmetry and $y = 0$ corresponds to the point of peak laser intensity. The laser drives the target from the left and the shocks propagate to the right. A schematic of the initial target layout is shown at the top of Fig. 131.4(a), and the dashed lines indicate unperturbed interface positions.

At 2.5 ns [Fig. 131.4(a)] the foremost shock reaches the Mo/SiO$_2$ interface, which agrees well with the data in Fig. 131.3. At this time, $\sim$200 ps after the end of the high-intensity drive, the strong shock is already starting to decrease in strength and has almost caught up with the weaker shock generated by the pre-plasma laser pulse. This is also in good agreement with the VISAR data, which exhibit two subsequent fringe jumps within $\sim$100 ps: the first upon the breakout of the pre-plasma shock into the SiO$_2$ layer, quickly followed by the coalescence with the trailing strong shock. At 7.1 ns of the simulated target evolution [Fig. 131.4(b)], the shock front reaches the target/vacuum interface at the rear, also agreeing very well with the experimental data, which exhibit this event at 7.2 ns.
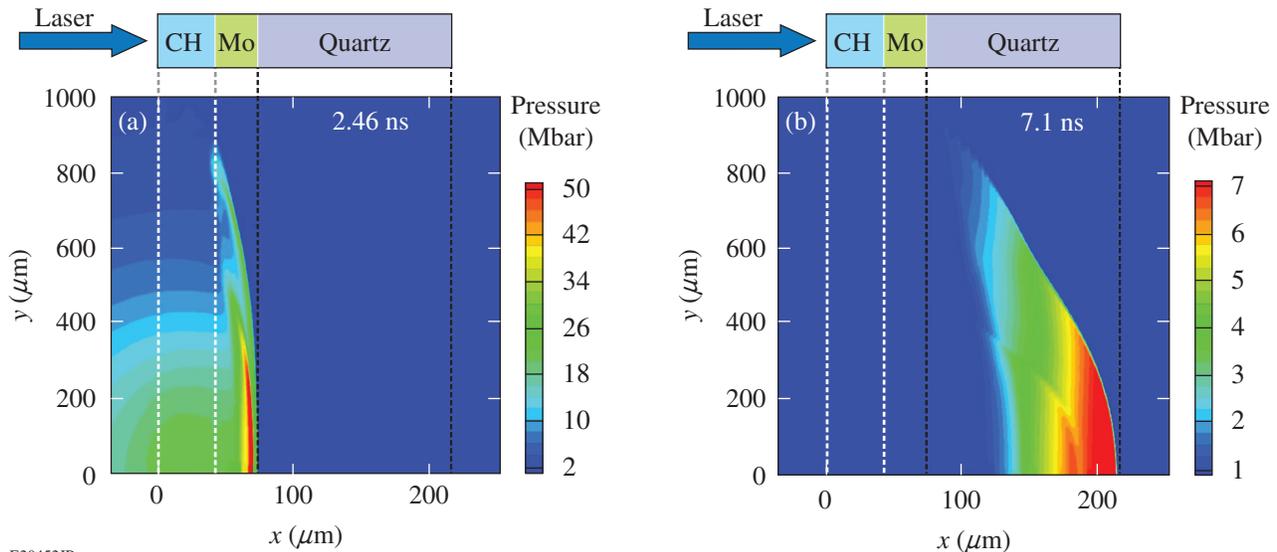

E20452JR

Figure 131.4
Snapshots of the pressure distribution at (a) 2.46 ns and (b) 7.1 ns from *DRACO* simulations using the experimental conditions for the data in Fig. 131.3. A schematic of the initial target layout is shown above (a) and (b). The dashed lines indicate initial interface positions.

The simulated target evolution is reproduced well over the range of intensities used in the experiment. Figure 131.5(a) shows the rear shock-breakout time as a function of spike intensity, with the squares denoting experimental data and the circles numerical results. The lowest-intensity case corresponds to no energy in Cone 1, i.e., no laser spike is incident on the target. The agreement between the simulated shock-propagation time to the experimentally measured one is better than 5% over the full intensity range, indicating a good numerical treatment of the laser–target interaction and ablator physics.

To extract the ablatively driven shock strength in the plastic layer from these simulations, the impedance mismatch between the plastic and Mo needs to be taken into account. The heavier Mo causes a partial shock reflection that overlaps with the laser-driven one, leading to an increase of the observed strong-shock strength in the ablator at the time of peak intensity. The purely ablatively driven shock strength was inferred through simulations using the same laser conditions, but an all-CH target. This results in a reduction of ~25% in the peak pressure, when compared to the CH/Mo/SiO$_2$ targets. The simulated ablation pressures corrected for the impedance mismatch are plotted as the blue circles in Fig. 131.5(b). The simulation results provide a scale relating shock propagation and ablation pressure, which was then used to infer ablation pressures via the experimentally observed shock-propagation time [red squares in Fig. 131.2(b)]. The error bars for the numerical results reflect temporal variations of the simulated pressure. This, in addition to the experimental uncertainty in the shock-propagation time, determines the error for the inferred pressures. Based on these results, a peak ablation pressure of ~70 Mbar was achieved with a drive intensity of ~1.2×10^{15} W/cm^2 in the presence of a long-scale-length pre-plasma. The simulated plasma density scale length at quarter-critical in these experiments is ~350 μm at the time of the high-intensity spike, with coronal temperatures between 2.0 keV and 2.9 keV, depending on the spike intensity. This compares well to previous experimental and numerical results for laser intensities of mid-10^{14} W/cm^2 (Refs. 18 and 20) but is lower than expected for a NIF-scale shock-ignition target (~450 μm, ~8 keV). The scale length in these experiments is limited by the focal-spot size, and the temperature by the spike intensity.

In Ref. 21 the stationary ablation pressure in a pure plastic target was derived to be $p_a = 40\left(I_{15}/\lambda_{\mu m}\right)^{2/3}$, where I_{15} denotes the absorbed laser intensity in units of 10^{15} W/cm^2 and $\lambda_{\mu m}$ is the laser wavelength in microns. The absorption fraction of the high-intensity spike observed in the simulations is typically ~90%. The simulations do not include hot electrons,
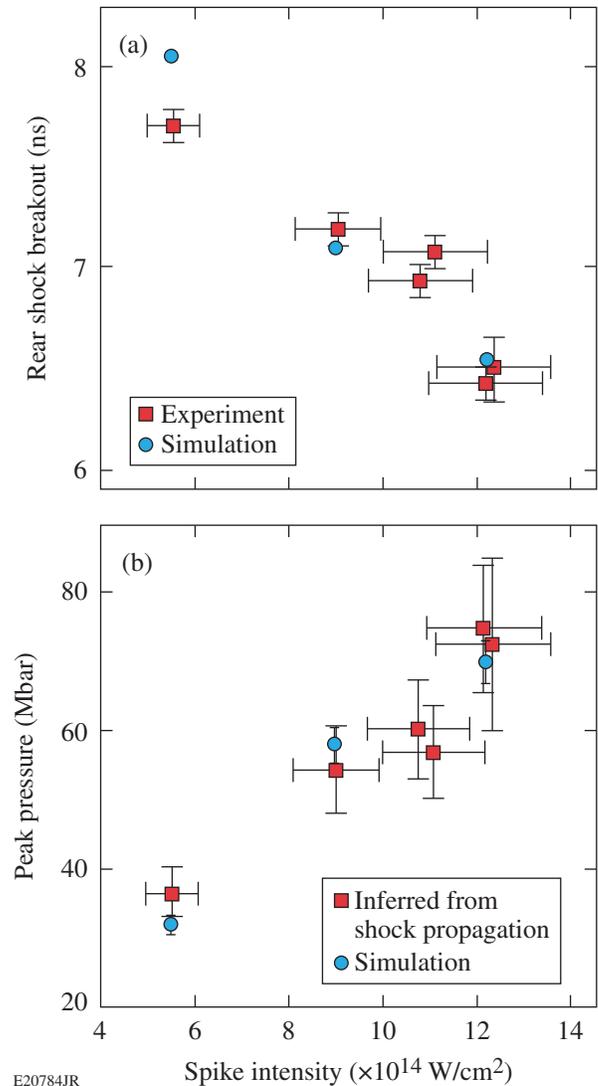
Figure 131.5
(a) Simulated (circles) and experimental (squares) shock-propagation time as a function of peak intensity; (b) laser-driven ablation pressure inferred from all-CH target simulations as a function of peak intensity.

but this contributes, at most, a few percent [Fig. 131.2(b)], and the agreement between simulated and observed target evolution gives confidence in the numerical treatment of the laser–target interaction. Applying the numerical absorption fraction to the pressure scaling overestimates the ablation pressure by 20% to 50%. This mismatch is not surprising since the pressure scaling makes the simplified assumption that laser absorption is limited to the critical surface, and therefore cannot be expected to capture the absorption physics correctly.

The simulations may be used to calculate the expected target conditions at full shock-ignition intensities. With a spike

intensity of $\sim 10^{16}$ W/cm^2, pressures of ~ 300 Mbar should be achieved for a simulated 70% absorption of the high-intensity spike—sufficient to drive a shock-ignition experiment. As before, the simulations do not include a treatment of hot electrons, and whether this extrapolation is valid needs to be investigated. The impact of the hot-electron component on the strong-shock strength is still under investigation and will depend on the temperature of the electron distribution.[5] Clearly, more experiments are required to characterize the plasma and shock conditions at such high intensities.

In conclusion, experiments investigating shock strength and the impact of LPI at SI-relevant laser conditions have been performed. Planar targets were irradiated with laser pulses comprising a pre-plasma–generating foot and a high-intensity spike to launch a strong shock. At a peak intensity of 1.4×10^{15} W/cm^2, an electron temperature of 70 keV was measured with $\sim 1.8\%$ of the spike energy being converted to hot electrons, and $\lesssim 10\%$ of the laser energy was scattered. Simulations using the radiative 2-D hydrocode *DRACO* show very good agreement with the observed shock propagation. Based on these results, at an intensity of 1.2×10^{15} W/cm^2, a 70-Mbar shock was generated in the presence of a 350-μm pre-plasma. This is the highest pressure reported at SI-relevant conditions, and these experiments constitute an important step toward validating the shock-ignition concept experimentally.

ACKNOWLEDGMENT

REFERENCES

1. S. Atzeni and J. Meyer-ter-Vehn, *The Physics of Inertial Fusion: Beam Plasma Interaction, Hydrodynamics, Hot Dense Matter*, International Series of Monographs on Physics (Clarendon Press, Oxford, 2004).

2. R. Betti, C. D. Zhou, K. S. Anderson, L. J. Perkins, W. Theobald, and A. A. Solodov, Phys. Rev. Lett. **98**, 155001 (2007).

3. R. Nora and R. Betti, Phys. Plasmas **18**, 082710 (2011).

4. W. Theobald, R. Betti, C. Stoeckl, K. S. Anderson, J. A. Delettrez, V. Yu. Glebov, V. N. Goncharov, F. J. Marshall, D. N. Maywar, R. L. McCrory, D. D. Meyerhofer, P. B. Radha, T. C. Sangster, W. Seka, D. Shvarts, V. A. Smalyuk, A. A. Solodov, B. Yaakobi, C. D. Zhou, J. A. Frenje, C. K. Li, F. H. Séguin, R. D. Petrasso, and L. J. Perkins, Phys. Plasmas **15**, 056306 (2008).

5. R. Betti, W. Theobald, C. D. Zhou, K. S. Anderson, P. W. McKenty, S. Skupsky, D. Shvarts, V. N. Goncharov, J. A. Delettrez, P. B. Radha, T. C. Sangster, C. Stoeckl, and D. D. Meyerhofer, J. Phys., Conf. Ser. **112**, 022024 (2008).

6. M. Tabak *et al.*, Phys. Plasmas **1**, 1626 (1994).

7. L. J. Perkins, R. Betti, K. N. LaFortune, and W. H. Williams, Phys. Rev. Lett. **103**, 045004 (2009).

8. X. Ribeyre *et al.*, Plasma Phys. Control. Fusion **51**, 015013 (2009).

9. B. Canaud and M. Temporal, New J. Phys. **12**, 043037 (2010).

10. S. Atzeni, A. Schiavi, and A. Marocchino, Plasma Phys. Control. Fusion **53**, 035010 (2011); O. Klimo *et al.*, Phys. Plasmas **18**, 082709 (2011); M. Lafon, X. Ribeyre, and G. Schurtz, Phys. Plasmas **17**, 052704 (2010); X. Ribeyre *et al.*, *ibid.* **18**, 102702 (2011); C. Riconda *et al.*, *ibid.* **18**, 092701 (2011); A. J. Schmitt *et al.*, *ibid.* **17**, 042701 (2010).

11. T. R. Boehly, D. L. Brown, R. S. Craxton, R. L. Keck, J. P. Knauer, J. H. Kelly, T. J. Kessler, S. A. Kumpan, S. J. Loucks, S. A. Letzring, F. J. Marshall, R. L. McCrory, S. F. B. Morse, W. Seka, J. M. Soures, and C. P. Verdon, Opt. Commun. **133**, 495 (1997).

12. J. E. Miller, T. R. Boehly, A. Melchior, D. D. Meyerhofer, P. M. Celliers, J. H. Eggert, D. G. Hicks, C. M. Sorce, J. A. Oertel, and P. M. Emmel, Rev. Sci. Instrum. **78**, 034903 (2007).

13. P. M. Celliers, D. K. Bradley, G. W. Collins, D. G. Hicks, T. R. Boehly, and W. J. Armstrong, Rev. Sci. Instrum. **75**, 4916 (2004).

14. C. Stoeckl, V. Yu. Glebov, D. D. Meyerhofer, W. Seka, B. Yaakobi, R. P. J. Town, and J. D. Zuegel, Rev. Sci. Instrum. **72**, 1197 (2001).

15. W. Seka, D. H. Edgell, J. P. Knauer, J. F. Myatt, A. V. Maximov, R. W. Short, T. C. Sangster, C. Stoeckl, R. E. Bahr, R. S. Craxton, J. A. Delettrez, V. N. Goncharov, I. V. Igumenshchev, and D. Shvarts, Phys. Plasmas **15**, 056312 (2008).

16. T. R. Boehly, V. A. Smalyuk, D. D. Meyerhofer, J. P. Knauer, D. K. Bradley, R. S. Craxton, M. J. Guardalben, S. Skupsky, and T. J. Kessler, J. Appl. Phys. **85**, 3444 (1999).

17. Y. Lin, T. J. Kessler, and G. N. Lawrence, Opt. Lett. **20**, 764 (1995).

18. B. Yaakobi, P.-Y. Chang, A. A. Solodov, C. Stoeckl, D. H. Edgell, R. S. Craxton, S. X. Hu, J. F. Myatt, F. J. Marshall, W. Seka, and D. H. Froula, Phys. Plasmas **19**, 012704 (2012).

19. P. B. Radha, V. N. Goncharov, T. J. B. Collins, J. A. Delettrez, Y. Elbaz, V. Yu. Glebov, R. L. Keck, D. E. Keller, J. P. Knauer, J. A. Marozas, F. J. Marshall, P. W. McKenty, D. D. Meyerhofer, S. P. Regan, T. C. Sangster, D. Shvarts, S. Skupsky, Y. Srebro, R. P. J. Town, and C. Stoeckl, Phys. Plasmas **12**, 032702 (2005).

20. D. H. Froula, B. Yaakobi, S. X. Hu, P.-Y. Chang, R. S. Craxton, D. H. Edgell, R. Follett, D. T. Michel, J. F. Myatt, W. Seka, R. W. Short, A. Solodov, and C. Stoeckl, Phys. Rev. Lett. **108**, 165003 (2012).

21. J. D. Lindl, Phys. Plasmas **2**, 3933 (1995).

Inelastic X-Ray Scattering from Shocked Liquid Deuterium

Extreme states of matter existing in astrophysical objects (e.g., stars and planetary interiors) can be created in the laboratory with high-intensity laser beams, particle beams, and Z-pinch generators.[1] High-energy-density physics (HEDP) encompasses the research of matter having energy densities of $\sim 10^{11}$ J/m^3 or more or, equivalently, pressures greater than 1 Mbar (Refs. 1 and 2). A subset of this field involves the study of warm, dense matter (WDM)[1,2] with electron temperatures around the Fermi temperature and the ratio of the potential energy to the kinetic energy of the ions greater than unity. The latter can be quantified by an ion–ion coupling parameter[2] $\Gamma_{\text{ii}} = (Ze)^2 / d_{\text{i}} k_{\text{B}} T > 1$, where Ze is the electric charge of the ion, d_{i} is the mean ion spacing, k_{B} is the Boltzmann constant, and T is the temperature. In shock-compressed matter at these extreme conditions, the determination of the system properties, in particular the equation of state (EOS), is complicated by the highly correlated nature of the medium, consisting of a system of strongly coupled ions immersed in a fluid of partially degenerate electrons. Understanding the physical properties (e.g., opacity,[3] conductivity,[4] EOS,[5] and compressibility[6]) of WDM is, however, very important for inertial confinement fusion (ICF) research[7,8] and the study of planetary interiors[9] because theoretical models differ by factors of several when predicting these quantities. In the past decade, developments in laser-produced plasma sources and detector efficiencies have made inelastic x-ray scattering a powerful diagnostic providing electron temperature (T_{e}), electron density (n_{e}), and ionization (Z) for critical EOS measurements in ICF and planetary science research.[10–14]

This article describes the first experimental observation of noncollective, inelastic x-ray Thomson scattering from liquid deuterium driven by a laser-produced $\sim$10-Mbar shock wave. The average electron temperature, electron density, and ionization are inferred from spectral intensity of the elastic (Rayleigh) and inelastic (Compton) components of the scattered Cl Ly$_\alpha$ emission at 2.96 keV. Two-dimensional (2-D) hydrodynamic simulations using EOS models designed for the extreme conditions found in ICF research and planetary interiors predict an average state of the plasma that is consistent with the x-ray scattering measurements.

The EOS of hydrogen for pressures <10 Mbar along the Hugoniot remains uncertain,[15–17] where detailed validation of experimental techniques and numerical modeling is of utmost importance. While the present work has not obtained density measurements with accuracy below a few percent, it provides a needed alternative experimental platform where such validation could take place. The reason is twofold: X-ray scattering experiments at near solid densities or above ($n_{\text{e}} > 10^{22}$ cm^{-3}) have been successfully performed at laser facilities[10] because of the high initial density. In the case of deuterium, as described here, a significant technological advance was necessary to observe the x-ray Thomson scattering with the development of dedicated cryogenic target hardware for the x-ray scattering experimental platform. This allowed liquid deuterium to be shock heated to reach densities comparable to previous x-ray scattering experiments. Since an elastic scattering cross section goes as Z^2, cryogenic liquid deuterium scatters significantly less x rays than previous experiments using room-temperature solids. To overcome the reduction in scattering fraction and achieve a reasonable signal-to-noise ratio, a target geometry with a large collection volume inside the cryogenic cell was adopted for this proof-of-principle experiment at a cost of spatial resolution and accuracy in the density measurements.

This research provides an experimental platform for the detailed study of compressed deuterium and is an important step toward measuring all the thermodynamic variables needed for EOS research, i.e., pressure (p), mass density (ρ), electron density (n_{e}), electron temperature (T_{e}), and ionization (Z), by combining inelastic x-ray scattering with shock-velocity and optical pyrometry measurements.[5,15–17]

The platform to measure the spectrally resolved inelastic x-ray scattering from shocked deuterium was developed on the 60-beam, 30-kJ, 351-nm OMEGA Laser System.[18] Inelastic x-ray scattering is predominantly collective or noncollective, depending on the scattering parameter $\alpha_{\text{s}} = 1/k\lambda_{\text{s}}$, where the wave number of the scattered x ray is given by $k = 4\pi/\lambda_0 \sin(\theta/2)$ with the incident wavelength $\lambda_0 = 4.188$ Å, λ_{s} is electron screening length of the plasmas, and θ is the scattering angle. For the

partially ionized conditions in WDM, the screening length may be calculated from the Fermi distribution via a single integral.[19] An easier fourth-order interpolation between the classical Debye length and the Thomas–Fermi screening length valid for $T = 0$ yields the correct results within 2% (Ref. 19). If $\alpha_s < 1$, the scattering is dominated by independent electrons and is referred to as noncollective.[12] In this case, the free-electron contribution experiences a significant Compton shift $\Delta E_C = \hbar^2 k^2 / 2m_e$ and is Doppler broadened. The width of this scattering feature is sensitive to the electron temperature for nondegenerate plasmas. If $\alpha_s \gg 1$, the scattering by the collective modes, which are known as plasma waves or plasmons, is dominant and the scattering is referred to as collective.[2,10] To lowest order, the position of the energy-downshifted plasmon feature is related to the electron plasma frequency $\omega_{pe} = \sqrt{n_e e^2 / \varepsilon_0 m_e}$, providing an electron-density diagnostic. The Compton downshift for this experiment is 16.5 eV, and the plasma conditions and scattering geometry result in a scattering parameter of $\alpha_s \sim 1$. Since the electrons are partially degenerate, this implies that this inelastic scattering geometry is sensitive to both electron density and temperature, which is a novel regime for inelastic x-ray scattering.[10] Additional information on the plasma temperature is given by the height of the elastic scattering feature.[20]

The experimental setup is shown in Fig. 131.6(a). The 8-μm-thick plastic ablator containing a planar layer of liquid
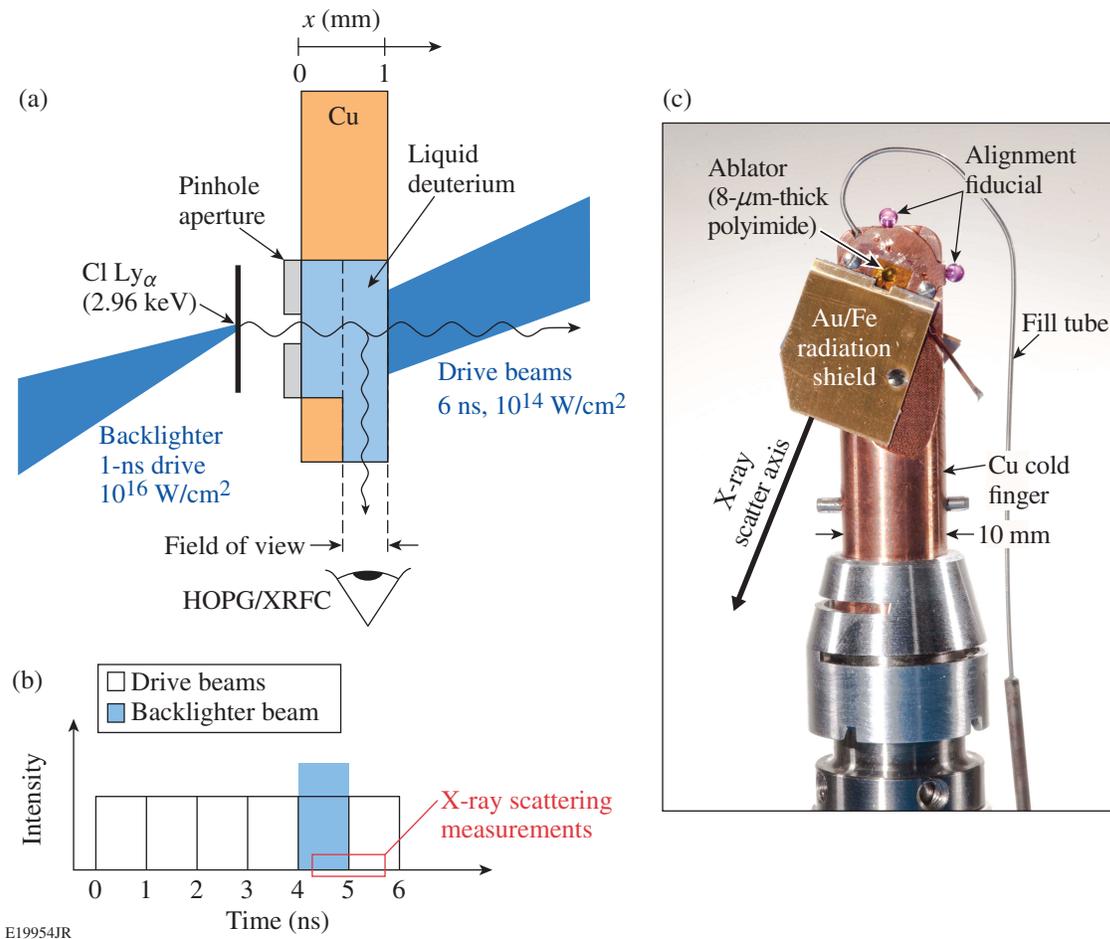
Figure 131.6

(a) Schematic of the x-ray Thomson-scattering (XRTS) experiment. An 8-μm CH ablator was irradiated with a constant-intensity, 6-ns UV laser drive, launching a shock wave through a cryogenic cell filled with liquid deuterium and creating warm, dense matter. Sixteen tightly focused beams irradiated a parylene D backlighter at 10^{16} W/cm^2, producing Cl Ly$_\alpha$ emission; this was scattered at ~90° and detected with an x-ray framing camera outfitted with a HOPG (highly oriented pyrolytic graphite) crystal spectrometer. (b) Timing of the drive and backlighter beams and the x-ray scattering measurements. (c) Photograph of the cryogenic XRTS target. The fill tube directs deuterium gas into the cryogenic cell, where it condenses into liquid. The ruby tooling balls on the top and right side of the Cu cold finger are target-alignment fiducials. The Au/Fe shield blocks a direct line of sight between the laser-produced plasmas and the detector, which is positioned ~90° to the laser drive axis.

deuterium was irradiated with a constant-intensity UV laser drive with 10^{14} W/cm^2. The laser drive, formed with six pairs of beams staggered in time as shown in Fig. 131.6(b), was uniform over a 0.5-mm diameter. Each laser beam was smoothed with a phase plate, producing a super-Gaussian spatial-intensity profile $I(r) = I_0 \exp\left[-(r/\delta)^n\right]$, with a 1/$e$ half-width $\delta = 438$ μm and super-Gaussian power $n = 4.5$. A laser-ablation–driven shock wave was launched through the liquid deuterium, creating warm, dense compressed matter. Sixteen tightly focused beams irradiated a parylene D backlighter with 10^{16} W/cm^2, generating a source of Cl Ly$_\alpha$ emission ($\lambda_0 = 4.188$ Å, $h\nu = 2960$ eV) (Ref. 21). These x rays were then scattered at $\theta = 87.8°$ from the shocked liquid deuterium and detected with an x-ray framing camera (XRFC) outfitted with a highly oriented pyrolytic graphic (HOPG) crystal spectrometer.[22] The backlighter x rays were collimated with a 200-μm-diam pinhole. The timing of the backlighter beams is shown in Fig. 131.6(b). The integration time of the x-ray scattering measurements is ~0.25 ns. A photograph of the cryogenic target with x-ray Thomson scattering (XRTS) capabilities mounted on the OMEGA planar cryogenic system is shown in Fig. 131.6(c), with the main components highlighted. The fill tube directs deuterium gas into the cryogenic cell, where it condenses into liquid. The ruby tooling balls on the top and right side of the Cu cold finger structure are target alignment fiducials. The Au/Fe shield blocks a direct line of sight between the laser-produced plasmas and the detector, which is positioned ~90° to the laser drive axis.

Two-dimensional hydrodynamic simulations of the experiment were performed with the *DRACO* code, which uses the *SESAME* EOS, a three-dimensional (3-D) laser ray trace model that calculates the laser absorption via inverse bremsstrahlung, a flux-limited thermal-transport approximation with a flux limiter of 0.06, and a multigroup diffusion radiation transport approximation using opacity tables created for astrophysics.[23] The simulation results shown in Fig.131.7, with the laser irradiation side and the location of the Cu wall indicated, predict at peak compression a mass density of $\rho \sim 0.8$ g/cm^3, a temperature of $T_e \sim 5$ to 15 eV, and an ionization stage of $Z \sim 0.5$ to 0.8 for the shocked liquid deuterium 5 ns after the drive beams were incident on the target ($t = 5$ ns). The shock front was predicted to have advanced ~375 μm at $t = 5$ ns and the shocked liquid deuterium had a compressed thickness of ~90 μm. As seen in Fig. 131.7, the spatial-intensity profile of the laser drive creates a curved shock front. The uniformly shocked liquid deuterium region occurs within $r < 0.25$ mm (see Fig. 131.7), and the underdriven shocked liquid deuterium is located at $r > 0.25$ mm. The predicted plasma conditions in the underdriven shocked portion of the target are lower than the uniform drive portion. The measured spectrum of the scattered x rays is spatially integrated and weighted to the shocked liquid deuterium region, which has the highest density. The field of view of the x-ray scattering channel either extends from $z = 0.5$ mm to $z = 1.0$ mm (see horizontal scale in Fig. 131.7) or is reduced to $z = 0.5$ mm to $z = 0.75$ mm by positioning a 250-μm-wide slit in
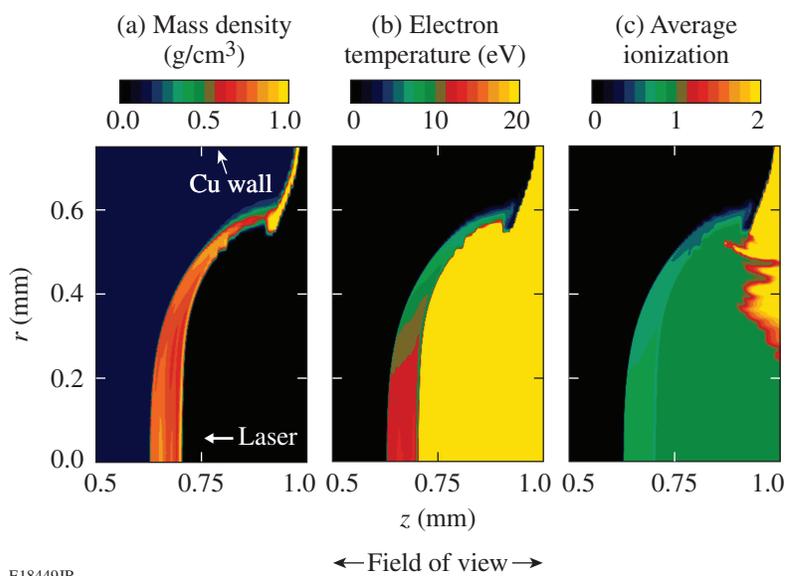
E18449JR

Figure 131.7
Contour plots of (a) mass density, (b) electron temperature, and (c) average ionization of shocked liquid deuterium at 5 ns, predicted using *DRACO*.

the scattering channel. The slit reduces the field of view of the scattering diagnostic to primarily the portion of the shocked liquid deuterium with uniform plasma conditions and blocks the scattering signal from the underdriven portion of the target.

The estimated number N of detected scattered photons[24] is calculated using

$$N = \left(\frac{E_T \eta_T}{h\nu}\right)\left(\frac{\Omega_T}{4\pi}\right)\left(\frac{n_e \sigma_T x}{\alpha_s^2 + 1}\right)\left(\frac{\Omega_x R}{4\pi}\right)\eta_d,$$

where, $E_T = 8$ kJ is the total UV laser energy incident on the parylene D backlighter foil, $\eta_T = 0.003$ is the UV to Cl Ly$_\alpha$ emission conversion efficiency, $h\nu = 2.96$ keV is the backlighter photon energy, $\Omega_T = 0.06$ steradian is the solid angle of the backlighter plasma sampled by the pinhole, $n_e = 2.2 \times 10^{23}$ cm^{-3} is the electron density of the shocked liquid deuterium, $\sigma_T = 6.6525 \times 10^{-25}$ cm^2 is the Thomson-scattering cross section, $x = 90$ μm is the thickness of the shocked liquid deuterium, $\alpha_s = 1.3$ is the scattering parameter, $\Omega_x = 0.02$ rad is the angle subtended by the detector in the direction perpendicular to the plane of dispersion, $R = 3$ mrad is the integrated reflectivity of the HOPG Bragg crystal, and $\eta_d = 0.01$ is the detector efficiency including filter transmissions. For a sampling time of ~0.25 ns, the total number of detected photons is $N \sim 700$. The thickness of the shocked liquid deuterium is an order of magnitude

smaller than the radiatively heated Be targets studied in earlier XRTS experiments;[11,14] consequently, the number of scattered photons in the shocked liquid deuterium experiment is at least an order of magnitude less than the Be experiment.

The scattered spectrum of the Cl Ly$_\alpha$ emission taken at $t = 5$ ns with a 250-μm slit in the scattering channel is shown in Fig. 131.8(a). The measurement taken without the slit is shown in Fig. 131.8(b), and the incident spectrum is shown in Fig. 131.8(c). The observed noise in the measured scattered x-ray spectrum is consistent with the estimated signal level. The incident spectrum is measured by irradiating a parylene D foil target on a separate laser shot. The scattered spectrum has a strong Rayleigh peak around 2960 eV and a Compton-downshifted feature. Scattered x-ray spectra were calculated using the x-ray scattering (XRS) code, which uses the finite-temperature random-phase approximation with static local field corrections to obtain the spectral shape of the inelastic (Compton) feature caused by scattering from free electrons.[25] The elastic scattering intensity strongly depends on the degree of ion–ion correlations in the plasma via the structure factor S_{ii} (Ref. 20). To constrain the value for S_{ii}, density functional theory molecular dynamics (DFT-MD) simulations were performed using the VASP package.[26,27] The simulations indicate weak ionic correlations for the conditions similar to the average of the plasma probed. This means the ion–ion structure factor S_{ii} at the relevant scattering wave number is close to unity for
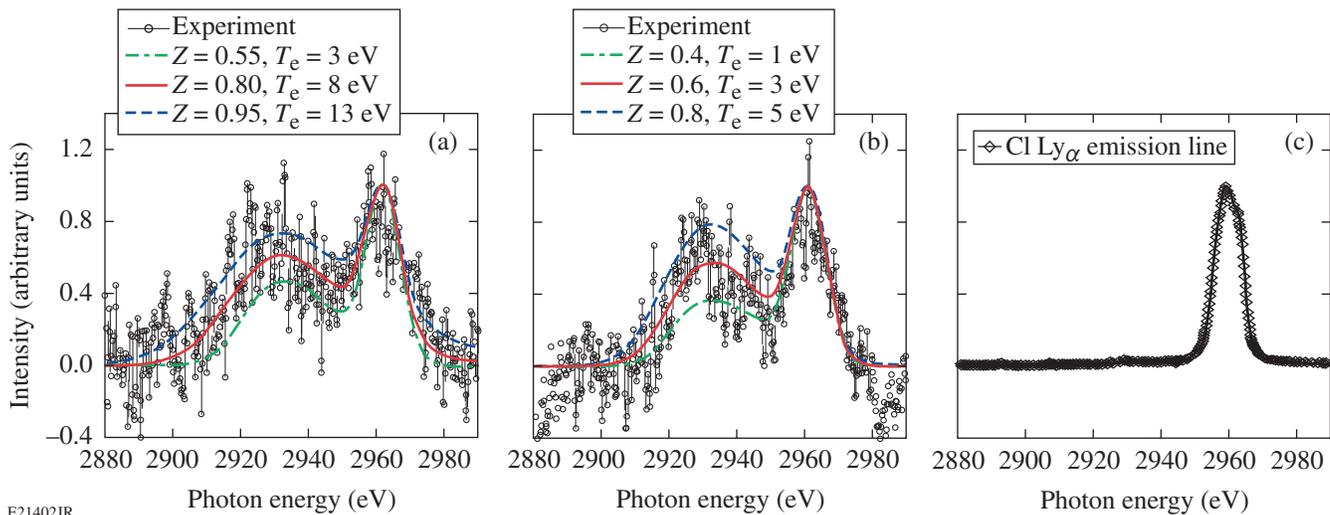
Figure 131.8
Measurement of (a) Cl Ly$_\alpha$ emission scattered from shocked liquid deuterium with a 250-μm slit in the scattering channel and simulated scattering spectra; (b) Cl Ly$_\alpha$ emission scattered from shocked liquid deuterium without a 250-μm slit in the scattering channel and simulated scattering spectra; and (c) Cl Ly$_\alpha$ emission incident on the shocked liquid deuterium. The inferred plasma conditions in (a) are $T_e = 8 \pm 5$ eV, $Z \sim 0.8$ (–0.25, +0.15), and $n_e = 2.2(\pm 0.5) \times 10^{23}$ cm^{-3} and in (b) are $T_e = 3 \pm 2$ eV, $Z \sim 0.6 \pm 0.2$, and $n_e = 2.0(\pm 0.5) \times 10^{23}$ cm^{-3}.

E21402JR

most of the conditions probed. With this information, the elastic scattering feature can be used to constrain the temperature and the ionization degree of the system. Structure factors close to unity are also found for the unshocked deuterium liquid. In addition to Doppler broadening, the width and position of the inelastic feature depend on the density for $\alpha_s \sim 1$. This fact allows us to bracket the electron density and estimate the ionization charge based on the initial mass density of the sample. The simulated scattering spectra computed using XRS provided the best fit to the spectrum measured with the slit for the following plasma conditions: $T_e = 8\pm5$ eV, $Z \sim 0.8$ (–0.25, +0.15), and $n_e = 2.2(\pm0.5) \times 10^{23}$ cm^{-3}. The *DRACO* simulations are in close agreement with the experimental results. These plasma conditions were repeatable on a subsequent laser shot. The plasma conditions inferred from the spectrally resolved x-ray spectrum recorded without the slit in the x-ray scattering channel are lower with $T_e = 3\pm2$ eV, $Z \sim 0.6\pm0.2$, and $n_e = 2.0(\pm0.5) \times 10^{23}$ cm^{-3}. The lower plasma pressure created by the lower-intensity portion of the laser drive causes the bowing of the shock front, as observed in Fig. 131.7. When the slit is placed in the scattering channel, the x rays scattered from this underdriven portion of the target are blocked from the detector. This leads to higher inferred values of T_e, Z, and n_e more representative of the uniformly shocked region.

In conclusion, this article reports the first experimental observation of noncollective, inelastic x-ray scattering from shocked liquid deuterium. An electron temperature of $T_e = 8\pm5$ eV, ionization $Z \sim 0.8$ (–0.25, +0.15), and electron density $n_e = 2.2(\pm0.5) \times 10^{23}$ cm^{-3} are inferred from the shapes and intensities of the elastic (Rayleigh) and inelastic (Compton) components in the scattering spectra. These plasma conditions are Fermi degenerate with similar electron and Fermi temperatures $\left(T_e / T_F \sim 1\right)$. Two-dimensional hydrodynamic simulations using EOS models suited for the extreme conditions indicate that the predicted average state of the probed plasma are consistent with the x-ray scattering measurements. Differently from previous VISAR measurements, the x-ray scattering experimental platform offers the considerable advantage of probing off-Hugoniot states. This experimental result is a significant step toward achieving accurate measurements of all thermodynamic variables needed to provide stringent tests of EOS models, which would require at least three thermodynamic variables like pressure, mass density, and temperature.

REFERENCES

1. National Research Council (U.S.) Committee on High Energy Density Plasma Physics, *Frontiers in High Energy Density Physics: The X-Games of Contemporary Science* (National Academies Press, Washington, DC, 2003).

2. S. Ichimaru, Rev. Mod. Phys. **54**, 1017 (1982).

3. J. E. Bailey *et al.*, Phys. Rev. Lett. **99**, 265002 (2007).

4. K. Widmann *et al.*, Phys. Rev. Lett. **92**, 125002 (2004).

5. J. Eggert, S. Brygoo, P. Loubeyre, R. S. McWilliams, P. M. Celliers, D. G. Hicks, T. R. Boehly, R. Jeanloz, and G. W. Collins, Phys. Rev. Lett. **100**, 124503 (2008).

6. S. X. Hu, V. A. Smalyuk, V. N. Goncharov, J. P. Knauer, P. B. Radha, I. V. Igumenshchev, J. A. Marozas, C. Stoeckl, B. Yaakobi, D. Shvarts, T. C. Sangster, P. W. McKenty, D. D. Meyerhofer, S. Skupsky, and R. L. McCrory, Phys. Rev. Lett. **100**, 185003 (2008).

7. R. L. McCrory, D. D. Meyerhofer, R. Betti, R. S. Craxton, J. A. Delettrez, D. H. Edgell, V. Yu Glebov, V. N. Goncharov, D. R. Harding, D. W. Jacobs-Perkins, J. P. Knauer, F. J. Marshall, P. W. McKenty, P. B. Radha, S. P. Regan, T. C. Sangster, W. Seka, R. W. Short, S. Skupsky, V. A. Smalyuk, J. M. Soures, C. Stoeckl, B. Yaakobi, D. Shvarts, J. A. Frenje, C. K. Li, R. D. Petrasso, and F. H. Séguin, Phys. Plasmas **15**, 055503 (2008).

8. J. D. Lindl *et al.*, Phys. Plasmas **11**, 339 (2004).

9. D. Saumon and G. Chabrier, Phys. Rev. A **44**, 5122 (1991).

10. S. H. Glenzer and R. Redmer, Rev. Mod. Phys. **81**, 1625 (2009).

11. S. H. Glenzer *et al.*, Phys. Rev. Lett. **90**, 175002 (2003).

12. G. Gregori *et al.*, Phys. Rev. E **67**, 026412 (2003).

13. H. Sawada, S. P. Regan, D. D. Meyerhofer, I. V. Igumenshchev, V. N. Goncharov, T. R. Boehly, R. Epstein, T. C. Sangster, V. A. Smalyuk, B. Yaakobi, G. Gregori, S. H. Glenzer, and O. L. Landen, Phys. Plasmas **14**, 122703 (2007).

14. S. H. Glenzer *et al.*, Phys. Rev. Lett. **98**, 065002 (2007).

15. G. W. Collins *et al.*, Science **281**, 1178 (1998).

16. P. M. Celliers *et al.*, J. Appl. Phys. **98**, 113529 (2005).

17. K. Falk, S. P. Regan, J. Vorberger, M. A. Barrios, T. R. Boehly, D. E. Fratanduono, S. H. Glenzer, D. G. Hicks, S. X. Hu, C. D. Murphy, P. B.

Radha, S. Rothman, A. P. Jephcoat, J. S. Wark, D. O. Gericke, and G. Gregori, High Energy Density Phys. **8**, 76 (2012).

18. T. R. Boehly, D. L. Brown, R. S. Craxton, R. L. Keck, J. P. Knauer, J. H. Kelly, T. J. Kessler, S. A. Kumpan, S. J. Loucks, S. A. Letzring, F. J. Marshall, R. L. McCrory, S. F. B. Morse, W. Seka, J. M. Soures, and C. P. Verdon, Opt. Commun. **133**, 495 (1997).

19. D. O. Gericke *et al.*, Phys. Rev. E **81**, 065401(R) (2010).

20. E. García Saiz *et al.*, Nat. Phys. **4**, 940 (2008).

21. M. K. Urry *et al.*, J. Quant. Spectrosc. Radiat. Transf. **99**, 636 (2006).

22. A. Pak *et al.*, Rev. Sci. Instrum. **75**, 3747 (2004).

23. P. B. Radha, V. N. Goncharov, T. J. B. Collins, J. A. Delettrez, Y. Elbaz, V. Yu. Glebov, R. L. Keck, D. E. Keller, J. P. Knauer, J. A. Marozas, F. J. Marshall, P. W. McKenty, D. D. Meyerhofer, S. P. Regan, T. C. Sangster, D. Shvarts, S. Skupsky, Y. Srebro, R. P. J. Town, and C. Stoeckl, Phys. Plasmas **12**, 032702 (2005).

24. O. L. Landen *et al.*, J. Quant. Spectrosc. Radiat. Transf. **71**, 465 (2001).

25. G. Gregori *et al.*, High Energy Density Phys. **3**, 99 (2007).

26. G. Kresse and J. Furthmüller, Phys. Rev. B **54**, 11169 (1996).

27. J. Vorberger *et al.*, Phys. Rev. B **75**, 024206 (2007).

Enhancement of the Laser-Induced–Damage Threshold in Multilayer Dielectric Diffraction Gratings Through Targeted Chemical Cleaning

Introduction

Chirped-pulse amplification (CPA) has been an enabling technology in the development of ultrashort-pulse, high-power laser systems.[1–5] In a CPA setup, a pair of diffraction gratings is used to "chirp" the signal by stretching it in time, reducing the laser pulse to a much lower intensity before the beam travels through the amplifier. The amplified pulse passes through another set of gratings to recompress it to its original pulse duration. At LLE, eight sets of tiled multilayer dielectric (MLD) gratings are used in pulse compressor chambers for OMEGA EP's two short-pulse beamlines. Each grating segment is 10 cm thick, 47 cm wide, and 43 cm tall; a complete tiled-grating assembly (TGA) is 1.4 m wide and includes three grating segments. The requirements on these critical, large-aperture optics are rigorous: laser-induced damage thresholds greater than 2.7 J/cm^2 (beam normal) for a 10-ps pulse at 1054 nm incident at 61° and a minimum diffraction efficiency of 97%. Because these demands have not yet been met, OMEGA EP's short-pulse beamlines are currently operated at ~60% of their design energy.

Surface contamination can dramatically reduce a grating's resistance to laser-induced damage.[5–13] OMEGA EP pulse compressor gratings are fabricated by etching a periodic groove structure (1740 lines/mm) into the top layer of a hafnia/silica multilayer mirror using interference lithography. Optionally, a bottom antireflective coating (BARC) is applied to the multilayer mirror to mitigate standing-wave effects during lithography and to improve fidelity. The grating fabrication process leaves large quantities of manufacturing residues and debris on the grating's surface that must be removed before the optic can go into service. Residues of hardened organic polymer BARC, in particular, are especially difficult to remove during final grating cleaning. Any photoresist or BARC residues, metal contaminants, surface debris, or light organic matter ultimately left on the grating can absorb energy during laser irradiation, initiating intense local heating and catastrophic laser-induced damage. Therefore, a final grating cleaning process that removes a broad spectrum of contaminant materials is essential. Mechanical contact with the delicate, microtextured grating surface must be absolutely avoided during cleaning, and cleaning techniques must not be so aggressive that they cause damage or defects. Additionally, short processing times and low temperatures are desirable for practical implementation on large parts and to mitigate thermal stress concerns.

MLD Grating Cleaning

Although surface contamination is a well-known cause of poor optical performance and laser-damage resistance, relatively few papers on cleaning methods for MLD gratings are available in the literature. Ashe et al.[9,10] were among the first to publish on this topic. They compared a number of chemical wet-cleaning methods commonly used in the semiconductor industry. Acid piranha, a mixture of sulfuric acid (H$_2$SO$_4$) and hydrogen peroxide (H$_2$O$_2$), was identified as the most-promising chemistry for MLD grating cleaning based on post-cleaning diffraction efficiency (DE) and laser-induced–damage threshold (LIDT) results. Other groups[11–14] have reported on the successful use of acid piranha to clean MLD gratings. Britten and Nguyen[13] developed a cleaning method for diffraction gratings that involved stripping bulk photoresist with an aqueous base and employing an oxidizing acid solution to remove residues; oxygen plasma was used as an intermediate step to remove fluorinated hydrocarbon residues. Plasma cleaning with oxygen and other gases has been suggested as a method for removing bulk organic layers of BARC[9,14] and photoresist[15,16] from gratings.

Britten et al.[17,18] demonstrated that briefly exposing an MLD grating to dilute buffered hydrofluoric acid (HF) solution after cleaning could increase resistance to laser-induced damage. HF lightly etches the silica pillars, simultaneously enhancing grating performance by removing surface residues and reducing the duty cycle (linewidth/period). Low duty cycles (tall, thin pillars) can enhance a grating's LIDT by minimizing electric-field enhancement.[19] Because low-duty-cycle gratings are considerably more difficult to fabricate than those having a traditional surface profile, the discovery of HF linewidth tailoring was a major advancement. The authors reported an average LIDT increase of 18.5% after etchback for 10-ps, 1053-nm damage

testing at 76.5° incidence. Britten *et al.* indicated that the HF linewidth-tailoring treatment "requires densified coating layers,"[18] but did not elaborate.

A few grating cleaning methods[10,17,19] have been shown to meet the OMEGA EP grating LIDT requirement of 2.7 J/cm^2 for a 1054-nm, 10-ps pulse using small grating samples.(a) Attempts to achieve similarly high damage thresholds on full-size OMEGA EP pulse compressor gratings and witness optics have so far been unsuccessful. One problem is that most damage-testing data have been reported for an air environment, while OMEGA EP gratings are operated in high vacuum. The testing environment can have a significant effect on results, especially for nondensified, porous MLD coatings (such as those used by LLE) because humidity and the volatility of contaminant materials in the vacuum chamber can play important roles. A second consideration is that the next generation of OMEGA EP gratings will, preferably, be fabricated with a BARC layer over the multilayer stack to minimize interference effects and distortion of the grating line structures at low duty cycles. Since many grating manufacturers do not use BARC, little information is available on stripping it from MLD gratings during final cleaning. Finally, wet-cleaning of MLD gratings has typically been performed at high temperatures (60°C to 110°C), especially when acid piranha is used to strip photoresist.[9–12] Such elevated processing temperatures have recently raised concerns about thermal-stress–induced defects, such as blistering and localized coating delamination, that can occur during cleaning. Two examples of coating failure observed in our lab on hafnia/silica MLD's and MLD gratings following elevated-temperature cleaning are given in Fig. 131.9. Figure 131.9(a) shows a group of ~40-μm-diam "blister" defects that nucleated near scratches on an MLD during piranha cleaning at 90°C. Figure 131.9(b) is a tiled micrograph showing localized delamination of an MLD grating after piranha cleaning at 70°C. To compound concerns about thermal stresses, the behavior of small witness gratings may not be representative of full-scale pulse compressor gratings. Large optics may be susceptible to modes of thermal-stress–induced failure not predicted by small witness parts.[20]

To resolve the above issues, we sought a grating cleaning process that (1) meets OMEGA EP's specifications for DE and in-vacuum LIDT; (2) is compatible with standard, nondensified reactive-evaporation MLD coatings; (3) effectively strips both

(a)Only Ashe[10] reported LIDT data for 61° beam incidence (OMEGA EP specification). Neauport's[19] and Nguyen's[17] data were reported for 77.2° and 76.5° incidences, respectively.

(a)

(b)

G9579JR
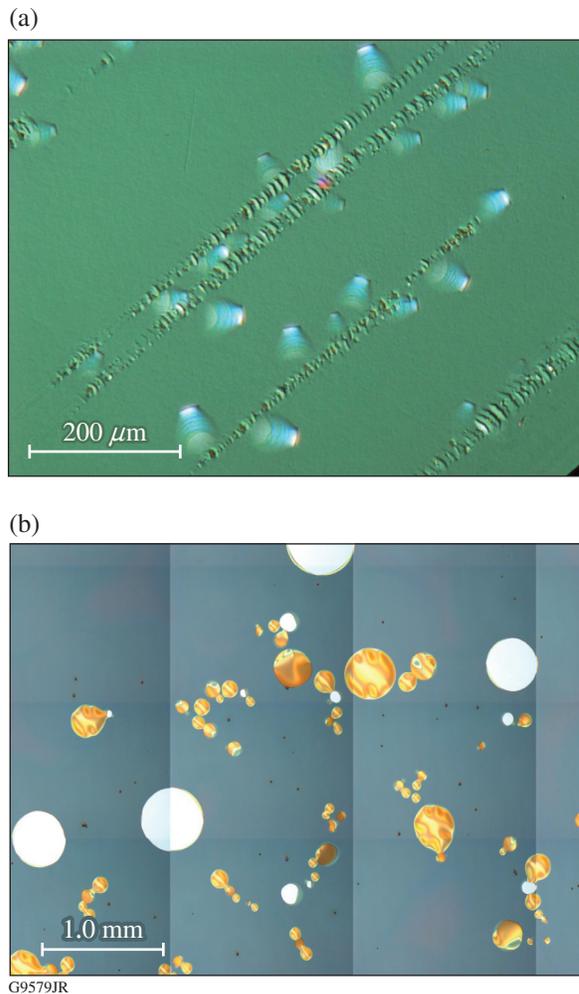
Figure 131.9
Coating failure observed after elevated-temperature acid piranha cleaning: (a) formation of "blister" defects observed on a multilayer dielectric (MLD) coating (no grating) after acid piranha cleaning at 90°C; (b) localized delamination observed on an MLD grating after acid piranha cleaning at 70°C.

photoresist and BARC; and (4) requires no chemical processing at temperatures above 40°C, to reduce thermal-stress concerns.

Experimental

1. MLD Grating Samples

Cleaning experiments were performed on small-scale MLD grating coupons. Ten 100-mm-diam, 3-mm-thick, round hafnia/silica MLD gratings were broken into eight equally sized, wedge-shaped coupons (80 samples total). Figure 131.10 shows the sample geometry. The multilayer coating was a modified quarter-wave thin-film stack[21] with hafnia (HfO$_2$) and silica (SiO$_2$) used as the high- and low-index materials, respectively. The total coating thickness was 4.8 μm. The MLD was deposited by reactive evaporation at 150°C using oxygen backfill

pressures of 2.0×10^{-4} Torr for hafnia deposition and zero for silica layer deposition. A BARC layer was applied over the multilayer to mitigate interference effects during photolithography. Grooves (1740 lines/mm) were etched into the top silica layer of the MLD. The samples were "identical" in that they were produced in the same coating run and processed together up until the final cleaning stage. Except as noted, all cleaning experiments described in this article were performed on *uncleaned* gratings with BARC and photoresist still intact (that is, they were not subjected to any photoresist stripping or other cleaning operations other than those described here).
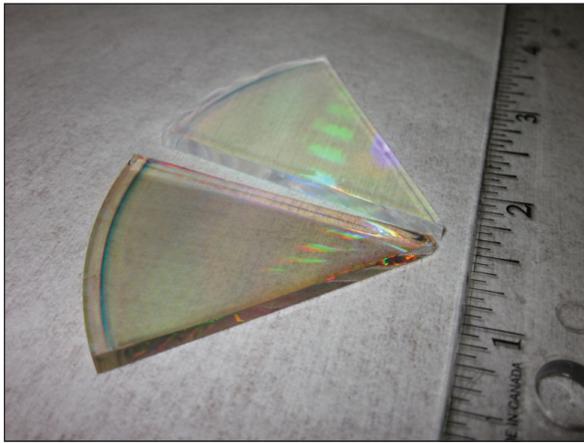
G9650JR

Figure 131.10
Grating wedge samples used in cleaning experiments, shown before (bottom) and after cleaning (top).

2. Laser-Induced–Damage Testing

Damage testing was performed at LLE's Damage Testing Facility on the short-pulse (10-ps) system, which can be operated in both air and high-vacuum (4×10^{-7} Torr) environments. MLD grating samples were tested using *s*-polarized light at 1054 nm, with an incident beam angle of 61° and an irradiation spot size of 370 μm (e^{-1} in intensity) in the far field. Laser-damage assessment was performed *in situ* using a white-light imaging system (~100× magnification). Damage was defined as a feature on the sample's surface that was not observed before laser irradiation. When switching between testing environments, samples were allowed to reach equilibrium with the environment (air or vacuum) for 24 h before testing continued. Damage thresholds are reported as beam normal fluences.

Each sample was tested in both 1-on-1 and *N*-on-1 testing regimes. The 1-on-1 damage threshold is determined by irradiating a sample site with one pulse and observing the sample

for damage. This is then repeated with increasing fluences on nonirradiated sample sites until damage is observed. The 1-on-1 threshold is the average of the fluence for the last site that did *not* damage the sample and the fluence for the first site that *did* damage, and the measurement error recorded is half the difference between these two numbers. *N*-on-1 damage testing is conducted by irradiating the sample site at a fluence significantly below the 1-on-1 threshold for ten shots. If no damage is detected, the fluence is increased and the same site is irradiated with five more shots. If no damage is observed after these shots, the fluence is increased again and another five shots are taken. This is continued until damage is observed in white light, at which point the damage onset fluence is recorded as the *N*-on-1 threshold for that site. The *N*-on-1 test is repeated for five sites on each MLD grating sample to generate an average and a standard deviation, which are reported as the *N*-on-1 threshold and measurement error, respectively.

3. Acid Piranha Cleaning at Low Temperatures

Many of the techniques used to clean MLD gratings have been developed from methods used for wafer cleaning in the semiconductor industry. Acid piranha, for example, has been known as a photoresist stripper since at least 1975 (Ref. 22), and its use is prevalent in the semiconductor industry. Standard operating procedure for acid piranha varies, but typical acid/peroxide ratios are in the range 2:1 to 7:1 (2 to 7 parts 99% sulfuric acid to 1 part 30% hydrogen peroxide) and typical processing temperatures are in the range 90°C to 140°C (Refs. 23 and 24). Optimized piranha-cleaning processes for MLD gratings documented in the open literature have been consistent with these ranges.[10–12] Ashe *et al.*[10] found that laser-damage resistance was maximized when high cleaning temperatures were used and when the proportion of H_2O_2 in the piranha solution was high. Piranha 2:1 (two parts sulfuric acid, one part hydrogen peroxide) at 100°C gave the best LIDT results. The authors recorded *N*-on-1 damage thresholds as high as 3.27 J/cm^2 in air after piranha cleaning—exceeding the OMEGA EP pulse compressor grating performance specification of 2.7 J/cm^2. Thresholds above 2.7 J/cm^2, however, were observed only for grating samples cleaned at temperatures of 80°C or higher, and these were in-air values only.

Because of thermal stress concerns, we chose to work at temperatures of 40°C or below. Table 131.I shows cleaning parameters and post-cleaning DE and LIDT results for a group of grating samples cleaned for 30 min at 40°C in an acid piranha bath. Some experiments involved two piranha treatments. This methodology was motivated by Beck *et al.*,[22] who suggested a two-step photoresist strip that employed first

Table 131.I: Treatments and results for 30-min acid piranha soak cleaning experiments, illustrating that acid piranha alone does not clean MLD gratings effectively at 40°C.

Part ID	Ratio $H_2SO_4:H_2O_2$/duration		Cleaning temperature	Post-cleaning DE	Post-cleaning LIDT (J/cm^2) *in vacuum*	
	Treatment 1	Treatment 2			1-on-1	*N*-on-1
555-2	10:1/15 min	5:1/15 min	40°C	84.6±0.8%	0.66±0.01	0.97±0.03
555-1	5:1/15 min	2:1/15 min	40°C	91.7±1.5%	0.84±0.06	1.08±0.11
555-6	10:1/30 min		40°C	90.8±1.2%	0.76±0.02	1.00±0.05
555-5	5:1/30 min		40°C	81.3±1.0%	0.94±0.05	1.04±0.04
556-3	2:1/30 min		40°C	91.0±1.6%	0.95±0.04	1.08±0.06

an acid-rich dehydrating bath, followed by a peroxide-rich oxidizing bath, to exploit the complementary material-removal mechanisms of acid piranha (dehydration and oxidation).

The experiments clearly demonstrated that at these low temperatures, acid piranha cleaning was inadequate. During damage testing, the unamplified laser beam used for alignment "wrote a track" onto the grating as it scanned across the samples, indicating that photoresist was not completely removed. A scanning electron microscope (SEM) observation of sample #555-5 (5:1 piranha, 30 min, 40°C) revealed intact photoresist over the entire grating surface. In areas irradiated during damage testing, the photoresist was deformed and/or stripped away, as shown in Fig. 131.11. The laser treatment provided a "cleaning" effect in the center of the damage site, where the photoresist was entirely removed by the incident laser beam. Near the edges of the region there was significant scatter from partially removed, deformed, and peeling strands of photoresist.

4. Targeted Chemical Cleaning

While acid piranha may be an effective solitary cleaning chemistry for MLD gratings at high temperatures, such was not our experience at 40°C. The intentionally low processing temperature necessitated a new approach. Because gratings are sensitive to surface pollutants of many different types, we developed a multistep technique to ensure broadband removal of performance-limiting contaminants. Cleaning techniques were adapted and combined from various sources to develop the optimized method detailed in Table 131.II. Drawn from semiconductor wafer processing and grating cleaning literature, the references describe other applications for each cleaning technique.

The cleaning process includes six major steps: First, acid piranha is used to strip photoresist and BARC. The piranha strip is followed by plasma cleaning in room air to clear away partially removed BARC and photoresist. Microscopic

G9651JR
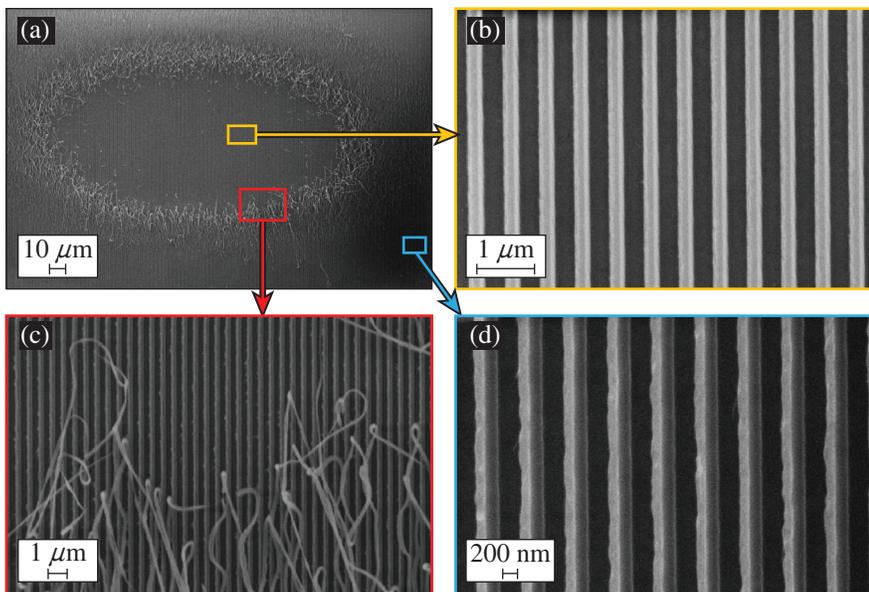
Figure 131.11
Scanning electron microscope (SEM) images of damage site on sample #555-5 irradiated at 1.40 J/cm^2 (1-on-1, 1054 nm, 10 ps, in vacuum, 61° incidence): (a) entire damage site; (b) intact pillars at center of site where all photoresist has been removed via laser irradiation ("cleaning" effect); (c) photoresist peeling away from pillars near the edge of the central region; (d) grating pillars near the edge of the damage site, where the photoresist layer is tilted over and partially detached from the grating pillars due to the 61° incident angle of the laser beam.

Table 131.II: Optimized cleaning method.

Process	Purpose	Method	Chemistry	Duration	Temperature
1. Piranha strip (Refs. 9–12, 22–24)	Strips/softens photoresist and BARC.	Spray onto optic; DI water rinse	$H_2SO_4{:}H_2O_2$ (5:1, 2:1)	5:1/15 min, 2:1/15 min	40° to 70°C
2. Plasma clean (Refs. 13,15, 16,23,24)	Removes light organics and partially removed material.	Room air used as process gas	n/a	10 min	Room temperature
3. Ionic clean (SC-2) (Refs. 23,24)	Eliminates remaining ionic/metallic contamination.	Beaker soak; DI water rinse	$HCl{:}H_2O_2{:}H_2O$ (1:1:6)	10 min	40° to 70°C
4. Plasma clean (Refs. 13,15, 16,23,24)	Removes light organics and partially removed material.	Room air used as process gas	n/a	10 min	Room temperature
5. Oxide etch (Refs. 18, 23,24)	Removes a thin layer of SiO_2 along with any stubbornly adhered contaminants; thins pillars slightly, reducing duty cycle.	Beaker soak; DI water rinse	HF:buffers (1:2500 to 1:3000)	5 min	Room temperature
6. Plasma clean (Refs. 13,15, 16,23,24)	Removes light organics and partially removed material.	Room air used as process gas	n/a	10 min	Room temperature

examination of samples suggested that BARC flakes off rather than gradually dissolving in piranha solution, and the plasma treatment ensures that material has been completely removed before proceeding to the next cleaning step. The third step in the cleaning process is an ionic clean with a Standard Clean 2 (SC-2) solution, a mixture of hydrochloric acid and hydrogen peroxide commonly used in the microelectronics industry to remove metallic contamination from silicon wafers. The inclusion of an ionic clean was motivated by the detection of molybdenum, a metal, on grating samples (see the next section). The ionic clean is followed by a second plasma treatment to clear away light organic matter collected on the sample. The next step is the oxide etch, which reduces the grating duty cycle and eliminates any remaining contaminants on the grating by removing a thin layer of silica.[17] Grating performance was quite sensitive to the concentration of the buffered oxide etch used. We found that dilutions in the range of 2500 to 3000 parts water/buffers to one part hydrofluoric acid were optimal for a 5-min etch (results discussed later in this section). The final step is a third air plasma treatment, which cleans the surface by removing light organics.

A total of 14 grating samples were cleaned according to the process steps shown in Table 131.II. The samples were then evaluated for damage threshold and diffraction efficiency; results are listed in Table 131.III. Average in-air damage thresholds were 4.01 J/cm^2 and 3.40 J/cm^2 in the 1-on-1 and N-on-1 regimes, respectively. For the five samples tested in a vacuum environment, average damage thresholds were 3.36 J/cm^2 (1-on-1) and 2.76 J/cm^2 (N-on-1) for 10-ps pulses at

1054 nm in vacuum. The data show good repeatability. For all samples except for the one having the lowest LIDT (562-7), the 1-on-1 threshold exceeded the N-on-1 threshold. This is not a typical result. N-on-1 thresholds are generally higher because contamination and debris on the grating surface are cleared away by low-fluence laser shots as beam fluence is ramped up, an effect known as "laser conditioning."[5] The absence of a laser-conditioning effect for the samples cleaned using the optimized method indicates that these gratings were already quite clean when damage testing began.

To our knowledge, this is the first time laser-induced–damage thresholds exceeding the OMEGA EP requirement of 2.7 J/cm^2 *in vacuum* have been reported for MLD gratings. These may also be the highest-reported 10-ps, 1054-nm damage thresholds for gratings fabricated using BARC. The average DE was 97.6%, meeting the OMEGA EP requirement on grating diffraction efficiency. Figure 131.12 compares SEM cross sections of a grating sample before and after cleaning, showing that BARC and photoresist were completely removed and that pillars were slightly narrowed.

The steps shown in Table 131.II were optimized using the set of 80 grating samples described in **MLD Grating Samples** (p. 150). Damage thresholds were found to be especially sensitive to the dilution of HF used in the oxide etch step. As shown in Fig. 131.13, LIDT results were best for grating samples prepared using buffer:HF ratios in the range 2500:1 to 3000:1. An 1800:1 ratio (not shown) led to total delamination of the grating MLD during the 5-min etch.

A major advantage of the targeted cleaning approach is its effectiveness at low temperatures. Lower temperatures lessen

G9652JR

Figure 131.12
SEM images showing MLD grating cross section (a) before chemical cleaning, with BARC and photoresist layers intact and (b) after cleaning, with BARC and photoresist stripped and grating pillars narrowed.

concerns about thermal stresses and reduce susceptibility to blistering and delamination defects. Initial piranha-cleaning experiments at low temperatures (see **Acid Piranha Cleaning at Low Temperatures**, p. 151) suggested that at temperatures

G9653JR
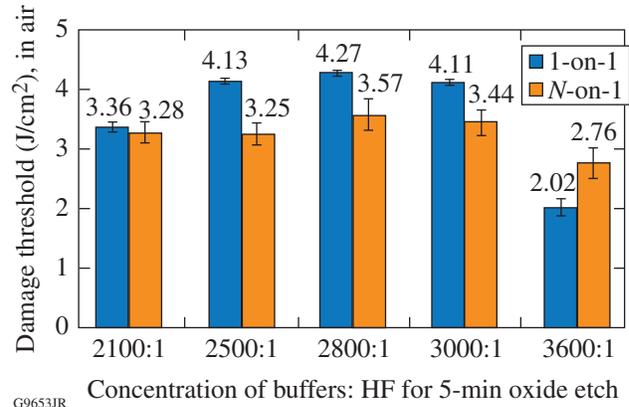
Figure 131.13
Effect of oxide etch concentration on laser-induced–damage threshold of MLD gratings.

Table 131.III: LIDT and DE results for grating samples cleaned using the optimized method.

Part ID	HF dilution (HF:buffers)	Cleaning temperature (piranha strip, ionic clean)	Post-cleaning DE	Post-cleaning LIDT (J/cm^2) *in air*		Post-cleaning LIDT (J/cm^2) *in vacuum*	
				1-on-1	N-on-1	1-on-1	N-on-1
562-6	2500:1	40°C	98.1±0.4%	4.40±0.17	3.49±0.17	3.30±0.19	2.74±0.14
566-1	2800:1	40°C	97.3±0.4%	3.87±0.13	3.32±0.18		
566-2[*]	2800:1	40°C	97.4±0.5%	3.32±0.13	3.20±0.12		
564-8[**]	2800:1	40°C	97.4±0.2%	4.24±0.18	3.44±0.21		
562-7	2500:1	50°C	97.4±0.4%	3.11±0.10	3.19±0.19	3.32±0.02	2.69±0.07
566-6	2800:1	50°C	97.4±0.5%	3.90±0.12	3.51±0.07		
557-2[***]	2800:1	50°C	96.4±0.7%	4.50±0.08	3.55±0.26	3.29±0.10	2.66±0.07
566-7	2800:1	60°C	97.5±0.3%	3.91±0.15	3.33±0.18		
555-5[***]	3000:1	60°C	97.0±0.3%	4.11±0.05	3.44±0.21		
564-7[*]	2500:1	70°C	98.7±0.3%	4.25±0.16	3.54±0.12		
564-6[**]	2500:1	70°C	97.6±0.3%	4.28±0.20	3.06±0.25		
562-3	2500:1	70°C	97.0±0.3%	4.07±0.01	3.39±0.10	3.19±0.16	2.90±0.04
566-8	2800:1	70°C	98.3±0.5%	3.89±0.20	3.56±0.31	3.70±0.16	2.82±0.20
555-2[***]	2800:1	70°C	97.8±0.4%	4.27±0.05	3.57±0.26		
Average (14 samples)			97.6%	4.01	3.40	3.36	2.76
Standard deviation (14 samples)			0.55%	0.40	0.16	0.20	0.10

[*]Piranha 2:1 only (30 min)

[**]Piranha 5:1 only (30 min)

[***]A re-used grating sample was used for this experiment. The earlier cleaning experiment did not remove photoresist/BARC.

of 40°C and below, acid piranha could not remove BARC and photoresist from an MLD grating. The cleaning approach shown in Table 131.II is much less temperature sensitive. Figure 131.14 shows in-air damage testing results for six samples cleaned using the optimized method at cleaning temperatures ranging from room temperature to 70°C. Differences in damage threshold results for the four samples cleaned in the range of 40°C to 70°C were not statistically significant, suggesting that cleaning temperatures can be safely reduced to the goal temperature of 40°C without negatively impacting grating performance.
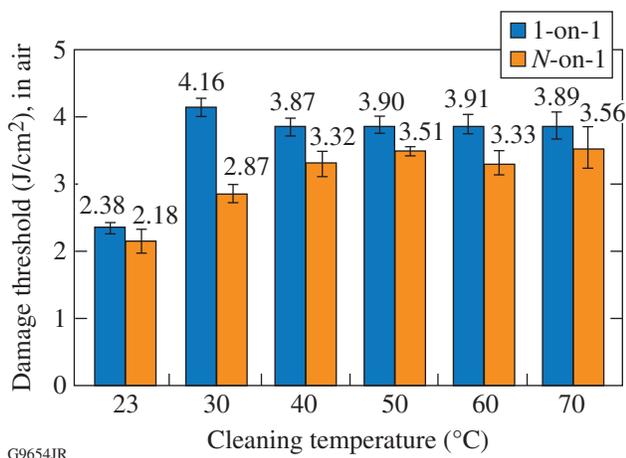

Figure 131.14
Relationship between in-air LIDT and cleaning temperature.

A unique aspect of the grating cleaning process shown in Table 131.II is the use of room air as the process gas in our plasma-cleaning setup. Plasmas generated from oxygen gas (O_2) are more commonly used.[13–16] We found oxygen plasma to be over aggressive, however, and using room air provides a gentler alternative. Figure 131.15 compares plasma-cleaning results for the two process gases. Grating samples were initially cleaned according to the method of Table 131.II and then plasma cleaned for 1, 3, 5, or 10 min using either oxygen or room air as the process gas in a Harrick PDC-32G plasma cleaner. All samples treated with room-air plasma saw an increase in diffraction efficiency (average, +0.43%) and met the OMEGA EP specification of 97% after cleaning, while all samples treated with oxygen plasma saw a drop in DE (average, –0.63%) and only two of four met the OMEGA EP specification. Shorter treatment times (15 and 30 s) were considered for oxygen plasma. The 15-s treatment improved diffraction efficiency modestly (+0.45%), but precise timing was a challenge for such short process durations because initial adjustments to generate a stable plasma require several seconds. The 30-s
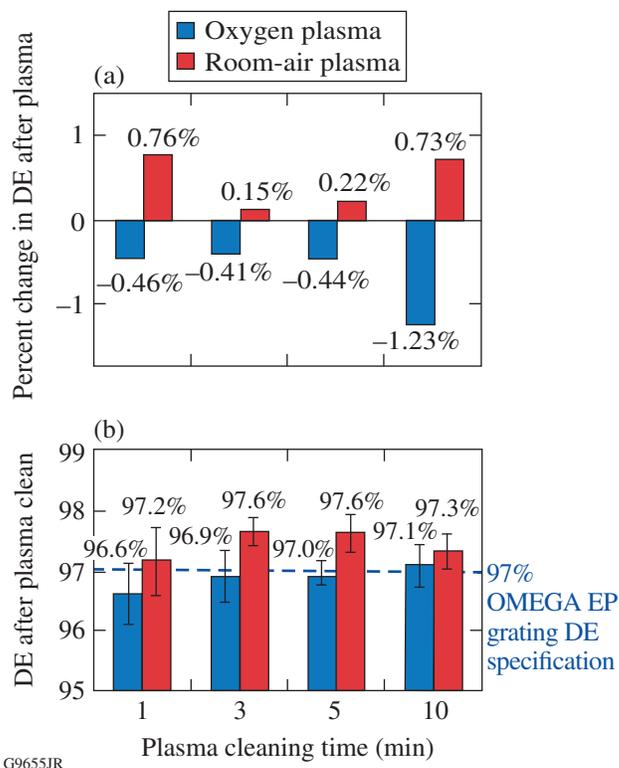
Figure 131.15
Comparison of oxygen and room-air plasma cleaning at room temperature. (a) Oxygen plasma cleaning for 1 to 10 min had a negative effect on diffraction efficiency, whereas room-air plasma cleaning enhanced DE. (b) All four samples treated with room-air plasma exceeded the 97% OMEGA EP grating DE specification, while only two of the four samples treated with oxygen plasma met this specification.

treatment had a negative effect on DE (–0.39%). Because room-air plasma was gentler, process control was superior because cleaning times could be longer.

Room-air plasma was found to be useful in "cleaning up" grating surfaces that failed to meet DE specifications after initial cleaning. Figure 131.16 shows the effect of a 15-min plasma treatment on three piranha-cleaned samples having initially poor diffraction efficiencies. Each of the three samples was improved from 86% to 87% to greater than 95% efficiency. We hypothesize that the air plasma treatment cleared away BARC and photoresist material that may have been softened or been partially removed in previous cleaning steps. Air plasma cleaning is effective at removing organic materials accumulated on the surface during storage and handling. In the optimized clean (Table 131.II), a plasma treatment is included after each wet-processing step to ensure that contaminants introduced (or partially removed) during previous cleaning steps are stripped away before moving on to the next cleaning phase.

Figure 131.16
Diffraction efficiency enhancement of MLD gratings after room-air plasma cleaning.

G9656JR

5. X-Ray Photoelectron Spectroscopy Results

X-ray photoelectron spectroscopy (XPS) was used to evaluate the composition of materials on the grating surface at different phases in the cleaning process. Grating samples were prepared according to Table 131.II, with acid piranha and ionic cleaning steps performed at 70°C and an HF ratio of 3000:1. A piece of grating was reserved for XPS analysis after each process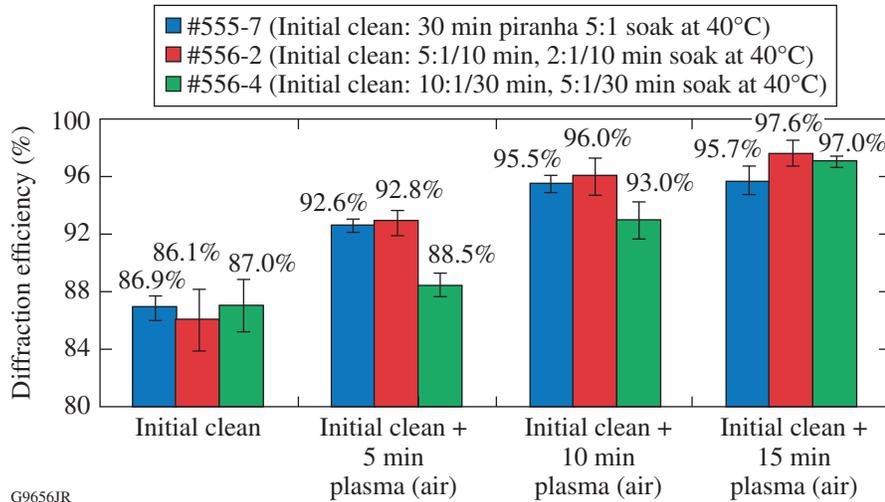. XPS testing was performed by the Penn State Materials Characterization Lab (sample #555-4), the University of Dayton Research Institute (samples #562-4A, #562-4B, #562-4C, and #562-4D), and the Cornell Center for Materials Research (sample #555-5). Identically prepared samples were also submitted for laser-induced–damage testing. Results are shown in Table 131.IV.

Since the top layer of the grating is SiO_2, the "ideal" XPS result for a well-cleaned grating would be 33% Si, 67% O, and nothing else. However, because samples are quickly contaminated with organic materials from the environment, some carbon is also expected. The detection of other elements (or large amounts of carbon) is undesirable and indicates insufficient removal of BARC, photoresist, and/or contaminants. In addition to silicon and oxygen (from the SiO_2 top layer), 42% carbon, 8% fluorine, and 3% molybdenum were detected on the uncleaned grating sample (#555-4). Much of the carbon is attributed to the organic photoresist/BARC layers still intact on the part. Fluorine contamination most likely occurred during reactive-ion beam etching of the grating's groove structure, as has been reported by others.[9,11,12] The detection of molybdenum was surprising and motivated the inclusion of a hydrochloric-acid–based ionic cleaning step to specifically target metallic contamination (see Table 131.II). The ionic clean may also remove trace contaminants such as potassium, sodium, chromium, iron, and aluminum. While not identified in XPS scans of our grating

Table 131.IV: Elements detected on MLD gratings at various stages of cleaning and corresponding damage-testing results.

Processing	Sample ID (XPS)	Elements detected by XPS (at. %)							Sample ID (damage testing)	LIDT *in air* (J/cm²)	
		O	Si	C	F	Mb	Hf	N		1-on-1	*N*-on-1
Uncleaned	555-4	35.2	12.0	41.8	8.00	2.60	–	–	555-4	<0.13	
Piranha	562-4A	45.6	16.4	32.4	1.63	–	–	4.0	560-3	1.41±0.06	1.87±0.11
Piranha + plasma	562-4B	60.3	26.7	13.1	–	–	–	–	560-3	2.13±0.11	2.27±0.09
Piranha + plasma + ionic clean	562-4C	61.0	26.6	12.4	–	–	–	–	560-3	2.28±0.05	2.45±0.12
Piranha + plasma + ionic clean + plasma	562-4D	61.3	26.8	11.9	–	–	–	–	560-3	2.13±0.04	2.34±0.13
Piranha + plasma + ionic clean + plasma + oxide etch + plasma	555-5	60.1	23.8	14.2	–	–	1.0	1.0	555-5	4.11±0.05	3.44±0.21

samples, Ashe *et al.*[9,10] detected these ions on similarly prepared MLD grating samples using the much more sensitive ToF-SIMS (time-of-flight secondary ion-mass spectrometry) technique. Metals absorb strongly at 1054 nm, so damage resistance is quite sensitive to this type of contaminant.

After the piranha and plasma treatments, fluorine and molybdenum levels were below the XPS detection limit and carbon levels had dropped to 13.1%. The biggest drop in carbon level occurred after the plasma treatment (rather than the piranha step), supporting our hypothesis that room-air plasma strips partially removed BARC and photoresist. The remaining cleaning steps (ionic clean, plasma, oxide etch, and plasma) did not have significant effects on the XPS spectra. Figure 131.17 shows contaminants detected side-by-side with LIDT results. After bulk removal of photoresist and BARC, XPS may not be sensitive enough to identify trace contaminants that limit resistance to laser-induced damage.

Conclusions

A low-temperature cleaning method was developed to remove manufacturing residues from MLD pulse-compressor gratings manufactured with polymer BARC. The process,

which is effective at processing temperatures as low as 40°C, targets specific families of contaminants in a sequence of cleaning operations. Samples cleaned using the optimized method had outstanding performance: laser-induced–damage thresholds averaged 4.01 J/cm^2 in air and 3.36 J/cm^2 in vacuum (1-on-1 testing regime, 10 ps, 1054 nm, 61°), and average diffraction efficiency was 97.6%.

REFERENCES

1. L. J. Waxer, D. N. Maywar, J. H. Kelly, T. J. Kessler, B. E. Kruschwitz, S. J. Loucks, R. L. McCrory, D. D. Meyerhofer, S. F. B. Morse, C. Stoeckl, and J. D. Zuegel, Opt. Photonics News **16**, 30 (2005).

2. D. Strickland and G. Mourou, Opt. Commun. **56**, 219 (1985).

3. G. A. Mourou, in *Encyclopedia of Modern Optics*, edited by R. D. Guenther, D. G. Steel, and L. P. Bayvel (Elsevier Academic Press, Amsterdam, 2005), pp. 83–84.
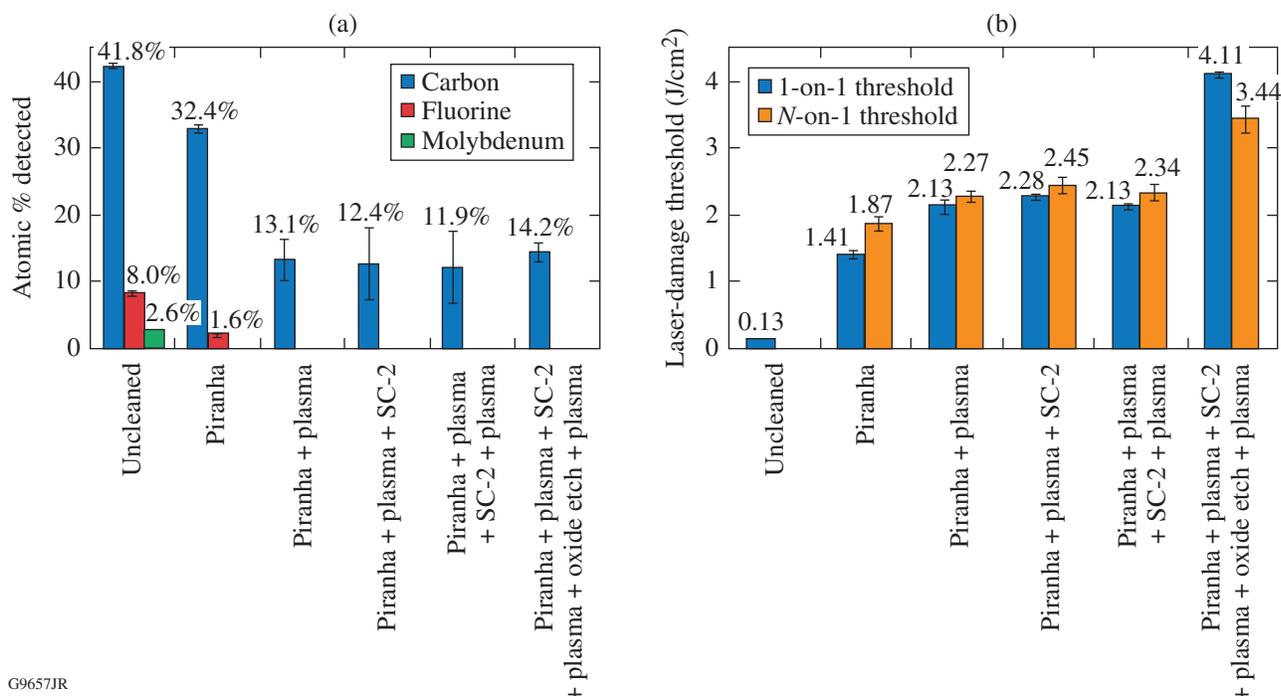
Figure 131.17
(a) Levels of carbon, fluorine, and molybdenum detected after each cleaning step; (b) corresponding laser-induced–damage thresholds.

4. J. A. Britten *et al.*, in *Laser-Induced Damage in Optical Materials: 1995*, edited by H. E. Bennett *et al.* (SPIE, Bellingham, WA, 1996), Vol. 2714, pp. 511–520.

5. I. Jovanovic *et al.*, in *Laser-Induced Damage in Optical Materials: 2004*, edited by G. J. Exarhos *et al.* (SPIE, Bellingham, WA, 2005), Vol. 5647, pp. 34–42.

6. B. Ashe, K. L. Marshall, D. Mastrosimone, and C. McAtee, in *Optical System Contamination: Effects, Measurements, and Control 2008*, edited by S. A. Straka (SPIE, Bellingham, WA, 2008), Vol. 7069, p. 706902.

7. W.-J. Kong *et al.*, Chin. Phys. Lett. **22**, 1757 (2005).

8. W. Kong *et al.*, Microelectron. Eng. **83**, 1426 (2006).

9. B. Ashe, K. L. Marshall, C. Giacofei, A. L. Rigatti, T. J. Kessler, A. W. Schmid, J. B. Oliver, J. Keck, and A. Kozlov, in *Laser-Induced Damage in Optical Materials: 2006*, edited by G. J. Exarhos *et al.* (SPIE, Bellingham, WA, 2007), Vol. 6403, p. 64030O.

10. B. Ashe, C. Giacofei, G. Myhre, A. W. Schmid, in *Laser-Induced Damage in Optical Materials: 2007*, edited by G. J. Exarhos *et al.* (SPIE, Bellingham, WA, 2007), Vol. 6720, p. 67200N.

11. S. Chen *et al.*, High Power Laser Part. Beams **23**, 2106 (2011).

12. S. Chen *et al.*, in *5th International Symposium on Advanced Optical Manufacturing and Testing Technologies: Advanced Optical Manufacturing Technologies*, edited by L. Yang *et al.* (SPIE, Bellingham, WA, 2010), Vol. 7655, p. 765522.

13. J. A. Britten *et al.*, U.S. Patent Application No. US 2008/0062522 A1 (13 March 2008).

14. B. Xu *et al.*, in *Proceedings of the 50th Annual Technical Conference of the Society of Vacuum Coaters* (Society of Vacuum Coaters, Louisville, KY, 2007), pp. 369–376.

15. Y. Hong *et al.*, Vacuum **45**, 25 (2008).

16. A. Bodere *et al.*, Mater. Sci. Eng. B **28**, 293 (1994).

17. H. T. Nguyen, C. C. Larson, and J. A. Britten, in *Laser-Induced Damage in Optical Materials: 2010*, edited by G. J. Exarhos *et al.* (SPIE, Bellingham, WA, 2010), Vol. 7842, p. 78421H.

18. J. Britten, C. Larson, M. Feit, and H. Nguyen, presented at the ICUIL 2010 Conference, Watkins, Glen, NY, 26 September–1 October 2010.

19. J. Neauport *et al.*, Opt. Express **15**, 12508 (2007).

20. H. Howard, J. C. Lambropoulos, and S. Jacobs, in *Optical Fabrication and Testing*, OSA Technical Digest (online) (Optical Society of America, Washington, DC, 2012), Paper OW3D.3.

21. J. B. Oliver, T. J. Kessler, H. Huang, J. Keck, A. L. Rigatti, A. W. Schmid, A. Kozlov, and T. Z. Kosc, in *Laser-Induced Damage in Optical Materials: 2005*, edited by G. J. Exarhos *et al.* (SPIE, Bellingham, WA, 2005), Vol. 5991, pp. 402–408.

22. W. Beck *et al.*, U.S. Patent No. 3,900,337 (19 August 1975).

23. G. W. Gale, R. J. Small, and K. A. Reinhardt, in *Handbook of Silicon Wafer Cleaning Technology*, 2nd ed., edited by K. A. Reinhardt and W. Kern, Materials Science & Process Technology Series (William Andrew, Norwich, NY, 2008), pp. 201–265.

24. D. W. Burns, in *MEMS Materials and Processes Handbook*, edited by R. Ghodssi and P. Lin (Springer, New York, 2011), Chap. 8, pp. 457–665.

Magnetic-Field Generation by Rayleigh–Taylor Instability in Laser-Driven Planar Plastic Targets

Target designs predicted to achieve ignition by inertial confinement fusion (ICF) rely on understanding Rayleigh–Taylor (RT) instability.[1–3] When an ICF capsule is imploded, the ablation front during the acceleration phase and the pusher–fuel interface during the deceleration and stagnation phases are RT unstable.[4,5] At the unstable interface, spikes of higher-density plasma penetrate into lower-density plasma and bubbles of lower-density plasma rise through the higher-density plasma. Understanding RT instability is important because it can amplify capsule perturbations and destroy implosion uniformity.

Previous theoretical work showed that a plasma subject to RT instability should generate spontaneous magnetic fields.[6,7] These fields may exist in inertial fusion plasmas and modify electron thermal transport.[8,9] If present and unaccounted for, these fields may degrade implosion performance compared to theoretical predictions.[10–12] Magnetic fields can be generated in high-energy-density plasmas by many different mechanisms,[13] including the thermoelectric effect,[14,15] anisotropic hot-electron velocity distributions,[16] and thermoelectric instability.[17] Recently the first measurement of RT-induced magnetic fields was reported,[18] which showed RT-induced magnetic fields in laser-accelerated targets with preimposed target-surface modulations from experiments on the OMEGA Laser System.[19] Magnetic fields with strengths of up to 0.1 MG were inferred in the linear growth phase of RT instability using face-on monoenergetic proton radiography.[20] The monoenergetic protons were generated from D–^{3}He fusion inside an imploding capsule.

This article reports on magnetic-field generation during the nonlinear growth phase of RT instability in an ablatively driven plasma using ultrafast laser-driven proton radiography.[21] Thin plastic foils were irradiated with ~4-kJ, 2.5-ns laser pulses focused to ~10^{14} W/cm^2 on LLE's OMEGA EP Laser System.[22] The driven foils were probed with an ultrafast proton beam that revealed the magnetohydrodynamic (MHD) evolution of the target. The target modulations were seeded by laser nonuniformities and amplified during the target-acceleration phase. These experiments show, for the first time, MG-level magnetic fields inside a laser-driven foil broken apart by RT instability. The experimental results are consistent with two-dimensional (2-D) MHD calculations using the code *DRACO*.[23,24]

Figure 131.18 shows a schematic of the experimental setup. Two long-pulse beams irradiated a 15- or 25-μm-thick CH foil.
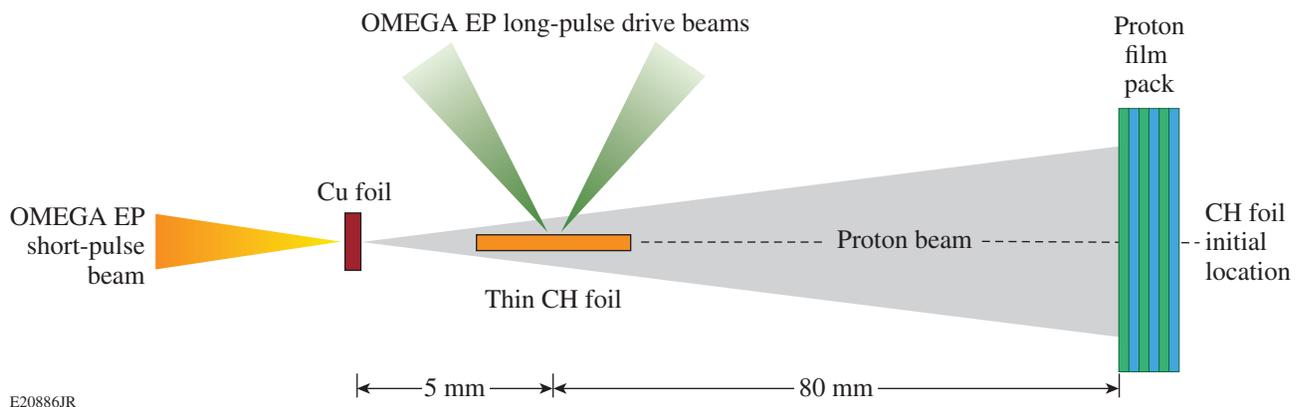

E20886JR

Figure 131.18
Experimental setup.

The foil area was 5×5 mm^2. Only a central ~1-mm-diam part of the foil was driven. Each laser beam delivered an ~2-kJ pulse with a wavelength of 351 nm and a 2.5-ns square temporal profile at 23° to the target normal. The laser beams were focused to ~850-μm-diam focal spots using distributed phase plates.[25] The average overlapped intensity was ~4×10^{14} W/cm^2.

The CH foil was probed in a direction orthogonal to the main interaction with an ultrafast proton beam.[26,27] The proton source was generated by irradiating a planar, 20-μm-thick Cu foil with an ~1-kJ, 10-ps pulse at a wavelength of 1.053 μm. The laser pulse was focused with a 1-m-focal-length, $f/2$ off-axis parabolic mirror onto the Cu foil at normal incidence, providing an intensity of ~5×10^{18} W/cm^2. The relative timing between the long-pulse and short-pulse beams was measured with an x-ray streak camera. Protons were accelerated from the surface of the Cu foil to tens of MeV by target normal sheath acceleration (TNSA).[28] The TNSA mechanism generated a highly laminar proton beam with a micron-scale virtual source size,[29] providing high spatial resolution for probing the main interaction with point-projection radiography.[21]

Combining a filtered stack detector with time-of-flight dispersion provided a multiframe imaging capability.[30] The high-energy protons that passed through the driven CH target were detected with a stack of radiochromic film interleaved with aluminum filters. Soft x rays were filtered with an additional aluminum foil on the front surface of the stack. Each film layer recorded a different probe time because the transit time for protons to the CH foil varied with energy. Protons with different energies deposited energy inside various film layers corresponding to their energy-dependent Bragg peak. The temporal coverage obtained in these experiments on a single shot was ~120 ps, with spatial and temporal resolutions of ~5 to 10 μm and ~10 ps, respectively. The image magnification $M = (L + l)/l$, where l is the distance from the proton-source foil to the CH target and L is the distance from the CH target to the radiochromic film detector. For these experiments, M was ~17 to 20, depending on the radiochromic film layer.

Figure 131.19 shows a typical proton radiograph of a 25-μm-thick CH foil unbroken by instability formation. This radiograph was obtained with 13-MeV protons at time $t = t_0 +$ 2.56 ns, where t_0 is the arrival time of the long-pulse beams at the target surface. The undriven foil horizon is indicated. The long-pulse beams irradiated the target from the left and the blowoff plasma accelerated the central part of the foil toward the right. The driven foil had a transverse size comparable with the laser focal spot. At this time, the foil had a velocity

E20888JR
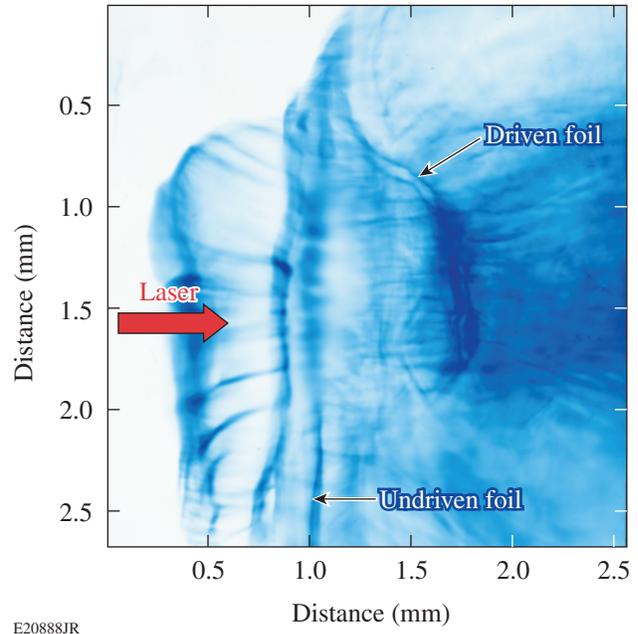
Figure 131.19
Proton radiograph of a 25-μm-thick CH foil taken with 13-MeV protons at $t = t_0 + 2.56$ ns. The laser drive, the undriven foil horizon, and the bow-shaped driven foil are indicated.

of $(3\pm1) \times 10^7$ cm/s, calculated from the measured driven-foil trajectory history.

Thinner-foil targets were broken by instability formation during the acceleration phase. Figure 131.20 shows proton radiographs for a 15-μm-thick CH foil driven with the same laser conditions as the 25-μm-thick foil case. These data were obtained with 13-MeV protons. The relative timing with respect to t_0 was varied from 2.11 ns to 2.56 ns. At $t = t_0 + 2.56$ ns, the foil has traveled a greater distance than the 25-μm-thick foil because less mass was accelerated. In this case, bubble-like structures are observed in the proton radiographs. These perturbations grow in time and show that the target has broken apart during the acceleration phase. Larger-scale structures at $t = t_0 + 2.56$ ns indicate this growth.

Further evidence for the broken foil is provided by the appearance of plasma beyond the driven target. Figure 131.20 shows a plasma sheath ahead of the RT-unstable region. Hot plasma in the laser-ablation region has fed through the compromised foil and formed a halo around the unstable expanding matter. A sheath electric field forms at the plasma/vacuum interface and is detected in the proton radiographs. This effect is not observed in the radiographs of the stable, 25-μm-thick foil, uncompromised by instability growth (see Fig. 131.19).
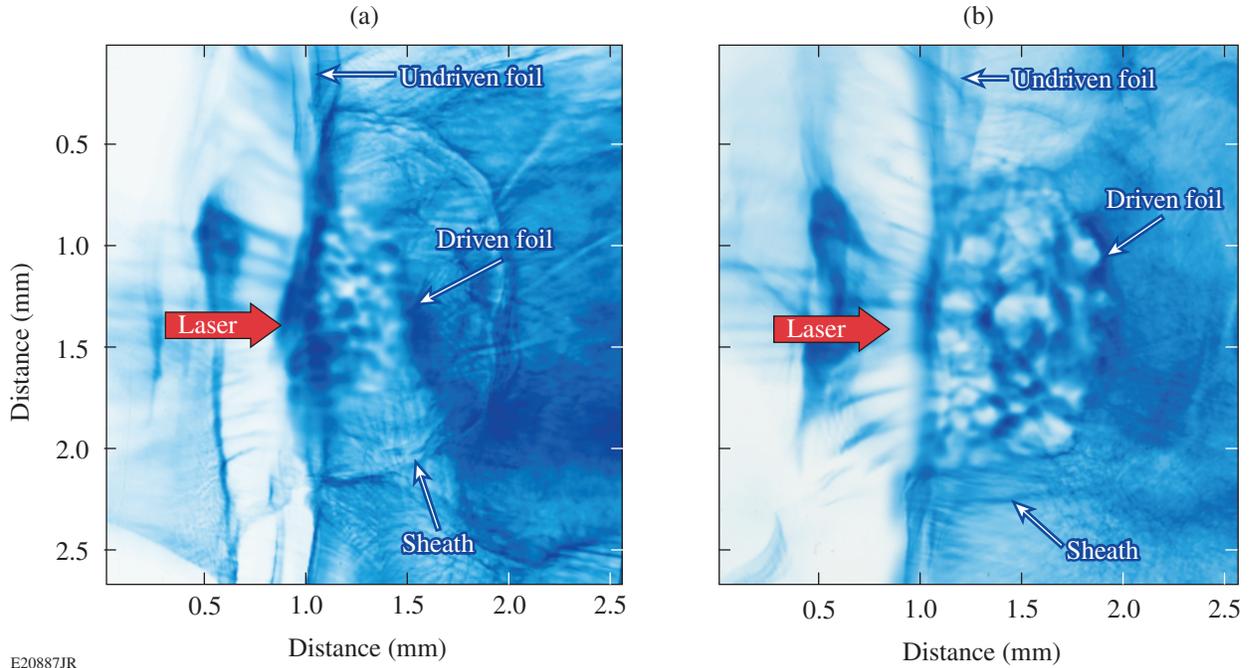
E20887JR

Figure 131.20
Proton radiographs of a 15-μm-thick CH foil taken with 13-MeV protons at (a) $t = t_0 + 2.11$ ns and (b) $t = t_0 + 2.56$ ns. The laser drive, the undriven foil horizon, the RT-unstable plasma, and the sheath field formed by hot-plasma feedthrough are indicated.

The main observation from these data is the electromagnetic fields that are generated during the RT-instability growth. In proton radiography, proton beam density modulations are caused by deflections from electromagnetic fields and by collisional scattering and stopping inside the probed target. For these experiments, collisional scattering and proton stopping are small. For example, collisional energy losses for 13-MeV protons passing through ~30-μm-thick solid CH are $\Delta E/E < 1\%$. Electromagnetic fields must play a dominant role in generating the bubble-like structures observed in the radiography data. The broken foil is revealed in the data by electromagnetic fields that are generated at the RT-unstable interface.

This interpretation is supported by numerical modeling with the 2-D resistive MHD code *DRACO*.[23,24] *DRACO* has a 2-D cylindrical geometry. The equation governing the magnetic field is

$$\frac{\partial \vec{B}}{\partial t} = \nabla \times (\vec{V} \times \vec{B})$$
$$+ \frac{c}{e} \left[\nabla \times \left(\frac{\nabla p_e}{n_e} \right) - \nabla \frac{(\nabla \times \vec{B}) \times \vec{B}}{4\pi n_e} - \nabla \times \frac{\vec{R_T} + \vec{R_u}}{n_e} \right], \quad (1)$$

where $\vec{B}$ is the magnetic induction, p_e is the electron pressure, n_e is the electron number density, e is the fundamental unit of charge, $\vec{V}$ is the flow velocity, and $\vec{R_T}$ and $\vec{R_u}$ are the thermal and frictional forces,[8] respectively. The second term on the right-hand side of Eq. (1) is the thermoelectric source term that is driven by nonparallel density and temperature gradients. The nonuniform ∇p_e force induces poloidal current loops that wrap around the magnetic toroids. The full Braginskii transport coefficients,[8] including the Nernst term[31] and cross-gradient thermal fluxes, were used to calculate $\vec{R_T}$ and $\vec{R_u}$. The temporal evolution of the laser power was provided by experimental measurements. The seeds for the growth of RT instability in the calculations were pre-imposed surface perturbations with a 50-μm wavelength and a 1-μm peak-to-valley amplitude.

The *DRACO* calculations show a 15-μm-thick foil broken apart by RT instability, generating MG-level magnetic fields at the RT-unstable interface. Figure 131.21(a) shows the calculated target-density profile at $t = t_0 + 2.1$ ns. Density perturbations that have grown by RT instability are greater in extent than the target thickness, breaking the foil apart. Large density and temperature gradients form in this unstable plasma and spontaneously generate MG-level magnetic fields. Figure 131.21(b) shows the predicted magnetic-field distribution at $t = t_0 + 2.1$ ns.

(a) Density (g/cm^3)

(b) Magnetic induction
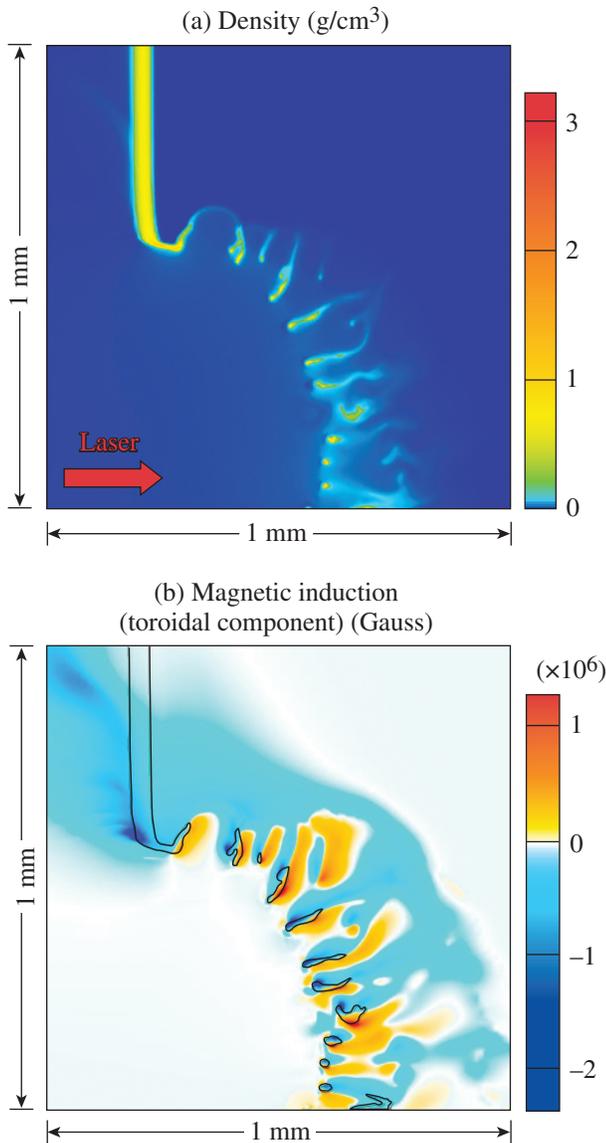(toroidal component) (Gauss)

E20889JR

Figure 131.21

(a) Simulated density profile at $t = t_0 + 2.1$ ns. The modeled target is axisymmetric about the horizontal axis. (b) Self-generated magnetic-field distribution at $t = t_0 + 2.1$ ns. The density contour for $\rho = 0.05$ g/cm^3 is overlaid.

Overlaid on this field distribution is the calculated density contour for $\rho = 0.05$ g/cm^3, indicating the position of the target. Magnetic fields generated at the ablation surface are convected toward the lower-density corona by the ablated plasma and to higher-density regions by hot electrons that carry the heat flux (the Nernst effect).[31] In our case, the Nernst convection significantly overperforms the convection by the ablation flow.

Magnetic fields of up to 2 MG are observed in these conditions beyond the coronal plasma and inside the driven foil.

DRACO simulations show that the dynamic effect of the generated magnetic fields on the RT instability is negligible in the linear and the moderately nonlinear stages of its evolution. The fields begin to enhance the RT growth in the highly nonlinear stages when the spike sizes are comparable to and larger than the perturbation wavelengths. The *DRACO* calculations reproduce the measured foil velocity to within experimental error, indicating that the gross hydrodynamics of the driven foil are as predicted. For a 25-μm-thick target, *DRACO* calculations show that the RT instability does not break the foil apart and no significant small-scale magnetic fields are generated.

The magnitude of the generated magnetic fields is estimated by measuring the angular deflection θ of protons from their original trajectory while passing through the field region. When the apparent displacement of protons is δ in the target plane, the angular deflection θ is calculated by $\tan\theta = M\delta/D$, where M is the geometric magnification and D is the distance between the main target and the radiochromic film detector. The proton-path–integrated B field caused by the Lorentz force acting upon the proton probe beam is $\int \vec{B} \times d\vec{l} = m_p v \sin\theta / e$, where m_p is the proton mass and v is the proton speed. In our experiments, the protons are deflected by azimuthal magnetic fields generated around the RT spikes. At $t = t_0 + 2.11$ ns, a δ of 25 μm results in a deflection angle θ of 0.31°. Assuming an integration path length slightly larger than the target thickness ($L \sim 25$ μm) gives a magnetic-field strength of ~1.4 MG, which is in good agreement with the *DRACO* simulations.

At the RT-unstable interface, narrow spikes are formed where the dense matter falls through the light matter, and bubbles are generated when the light material rises into the dense material.[3] This process generates magnetic fields that wrap around the troughs of the spikes. The growth of the spatial scale length of the perturbed features is caused by magnetic-field evolution as the RT instability develops. The magnetic-field topology in *DRACO* is different from the real three-dimensional (3-D) situation. In 3-D RT instability, azimuthal magnetic fields are formed around single spikes and bubbles. The magnitude and the predominant wavelength of the magnetic fields, however, are expected to be accurate.

A proton ray-tracing code using electromagnetic field distributions from the 2-D *DRACO* calculations supports

the dominant role of magnetic fields in deflecting protons in these experiments. The initial proton-source details and the radiography geometry were taken from the experiments. The accumulated proton numbers were monitored in the ray-tracing code at a simulated detector plane. Figure 131.22 shows the effect of electric and magnetic fields in this process. The predicted proton distribution is unchanged when electric fields are turned off in the calculations, while few proton deflections are observed when magnetic fields are turned off. Self-generated magnetic fields at the RT-unstable interface are the dominant cause for proton-beam deflections in these experiments. Two-dimensional Fourier analysis of the measured proton radiographs shows that the characteristic spatial scale length of the bubble-like features at $t = t_0 + 2.11$ ns is ~82 μm, growing to ~115 to 230 μm at $t = t_0 + 2.56$ ns. Broadly consistent with this experimental trend, Fourier analysis of the proton distribution in Fig. 131.22 gives a characteristic spatial scale length of ~93 μm, growing to ~220 μm at the latest time.
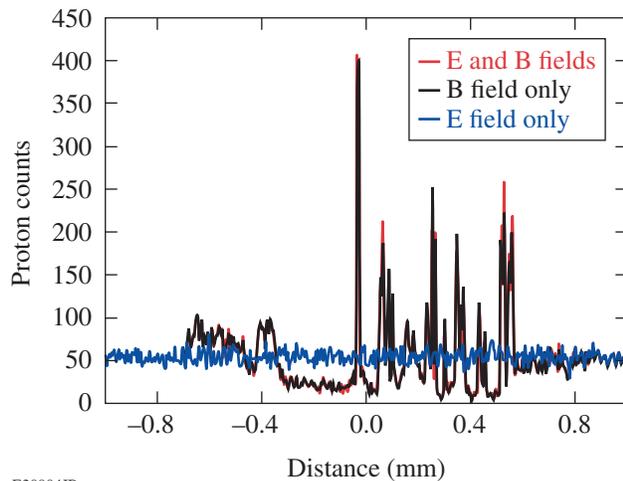
E20904JR

Figure 131.22
Proton tracking code results. Proton deflections are modeled based on electromagnetic field distributions predicted by 2-D *DRACO* calculations.

In summary, magnetic-field generation during the nonlinear growth of target perturbations by RT instability in ablatively driven foils was studied. Measurements of MG-level magnetic fields were supported by recovering characteristic spatial scale lengths of the proton deflections using a particle ray-tracing code that incorporates electromagnetic-field distributions from a 2-D MHD model. Electric fields were found to be negligible compared to the generated magnetic fields in producing the modulated patterns in the proton radiography beam profile. Simulations suggest that the dynamic effect of these magnetic fields on RT growth is not significant.

ACKNOWLEDGMENT

REFERENCES

1. Lord Rayleigh, Proc. London Math Soc. **XIV**, 170 (1883).

2. G. Taylor, Proc. R. Soc. London Ser. A **201**, 192 (1950).

3. R. Betti and J. Sanz, Phys. Rev. Lett. **97**, 205002 (2006).

4. J. D. Lindl, Phys. Plasmas **2**, 3933 (1995).

5. R. L. McCrory, D. D. Meyerhofer, S. J. Loucks, S. Skupsky, R. Betti, T. R. Boehly, T. J. B. Collins, R. S. Craxton, J. A. Delettrez, D. H. Edgell, R. Epstein, K. A. Fletcher, C. Freeman, J. A. Frenje, V. Yu. Glebov, V. N. Goncharov, D. R. Harding, I. V. Igumenshchev, R. L. Keck, J. D. Kilkenny, J. P. Knauer, C. K. Li, J. Marciante, J. A. Marozas, F. J. Marshall, A. V. Maximov, P. W. McKenty, S. F. B. Morse, J. Myatt, S. Padalino, R. D. Petrasso, P. B. Radha, S. P. Regan, T. C. Sangster, F. H. Séguin, W. Seka, V. A. Smalyuk, J. M. Soures, C. Stoeckl, B. Yaakobi, and J. D. Zuegel, J. Phys. IV France **133**, 59 (2006).

6. J. A. Stamper *et al.*, Phys. Rev. Lett. **26**, 1012 (1971).

7. K. Mima, T. Tajima, and J. N. Leboeuf, Phys. Rev. Lett. **41**, 1715 (1978).

8. S. I. Braginskii, in *Reviews of Plasma Physics*, edited by Acad. M. A. Leontovich (Consultants Bureau, New York, 1965), Vol. 1, p. 205.

9. M. G. Haines, Phys. Rev. Lett. **78**, 254 (1997).

10. J. A. Stamper, Laser Part. Beams **9**, 841 (1991).

11. R. G. Evans, Plasma Phys. Control. Fusion **28**, 1021 (1986).

12. B. Srinivasan, G. Dimonte, and X.-Z. Tang, Phys. Rev. Lett. **108**, 165002 (2012).

13. M. G. Haines, Can. J. Phys. **64**, 912 (1986).

14. J. A. Stamper and B. H. Ripin, Phys. Rev. Lett. **34**, 138 (1975).

15. D. G. Colombant and N. K. Winsor, Phys. Rev. Lett. **38**, 697 (1977).

16. K. Estabrook, Phys. Rev. Lett. **41**, 1808 (1978).

17. M. G. Haines, Phys. Rev. Lett. **47**, 917 (1981).

18. M. J. E. Manuel, C. K. Li, F. H. Séguin, J. Frenje, D. T. Casey, R. D. Petrasso, S. X. Hu, R. Betti, J. D. Hager, D. D. Meyerhofer, and V. A. Smalyuk, Phys. Rev. Lett. **108**, 255006 (2012).

19. T. R. Boehly, D. L. Brown, R. S. Craxton, R. L. Keck, J. P. Knauer, J. H. Kelly, T. J. Kessler, S. A. Kumpan, S. J. Loucks, S. A. Letzring, F. J. Marshall, R. L. McCrory, S. F. B. Morse, W. Seka, J. M. Soures, and C. P. Verdon, Opt. Commun. **133**, 495 (1997).

20. C. K. Li, F. H. Séguin, J. A. Frenje, J. R. Rygg, R. D. Petrasso, R. P. J. Town, P. A. Amendt, S. P. Hatchett, O. L. Landen, A. J. Mackinnon, P. K. Patel, V. A. Smalyuk, T. C. Sangster, and J. P. Knauer, Phys. Rev. Lett. **97**, 135003 (2006).

21. M. Borghesi *et al.*, Phys. Rev. Lett. **92**, 055003 (2004).

22. L. J. Waxer, D. N. Maywar, J. H. Kelly, T. J. Kessler, B. E. Kruschwitz, S. J. Loucks, R. L. McCrory, D. D. Meyerhofer, S. F. B. Morse, C. Stoeckl, and J. D. Zuegel, Opt. Photonics News **16**, 30 (2005).

23. D. Keller, T. J. B. Collins, J. A. Delettrez, P. W. McKenty, P. B. Radha, B. Whitney, and G. A. Moses, Bull. Am. Phys. Soc. **44**, 37 (1999).

24. I. V. Igumenshchev, F. J. Marshall, J. A. Marozas, V. A. Smalyuk, R. Epstein, V. N. Goncharov, T. J. B. Collins, T. C. Sangster, and S. Skupsky, Phys. Plasmas **16**, 082701 (2009).

25. *LLE Review Quarterly Report* **33**, 1, Laboratory for Laser Energetics, University of Rochester, Rochester, NY, LLE Document No. DOE/DP/40200-65, NTIS Order No. DE88008065 (1987).

26. E. L. Clark *et al.*, Phys. Rev. Lett. **85**, 1654 (2000).

27. R. A. Snavely, M. H. Key, S. P. Hatchett, T. E. Cowan, M. Roth, T. W. Phillips, M. A. Stoyer, E. A. Henry, T. C. Sangster, M. S. Singh, S. C. Wilks, A. MacKinnon, A. Offenberger, D. M. Pennington, K. Yasuike, A. B. Langdon, B. F. Lasinski, J. Johnson, M. D. Perry, and E. M. Campbell, Phys. Rev. Lett. **85**, 2945 (2000).

28. S. C. Wilks, A. B. Langdon, T. E. Cowan, M. Roth, M. Singh, S. Hatchett, M. H. Key, D. Pennington, A. MacKinnon, and R. A. Snavely, Phys. Plasmas **8**, 542 (2001).

29. T. E. Cowan *et al.*, Phys. Rev. Lett. **92**, 204801 (2004).

30. A. J. Mackinnon, P. K. Patel, M. Borghesi, R. C. Clarke, R. R. Freeman, H. Habara, S. P. Hatchett, D. Hey, D. G. Hicks, S. Kar, M. H. Key, J. A. King, K. Lancaster, D. Neely, A. Nikkro, P. A. Norreys, M. M. Notley, T. W. Phillips, L. Romagnani, R. A. Snavely, R. B. Stephens, and R. P. J. Town, Phys. Rev. Lett. **97**, 045001 (2006).

31. A. Nishiguchi, T. Yabe, and M. G. Haines, Phys. Fluids **28**, 3683 (1985).

High-Resolution Spectroscopy Used to Measure Inertial Confinement Fusion Neutron Spectra on OMEGA

Introduction

Nuclear diagnostics are essential to interpreting the condition of the DT fuel during compression in inertial confinement fusion (ICF) experiments.[1] Measurable parameters that determine the performance of ICF implosions include the ion temperature (T_i), areal density (ρR), and the primary DT neutron yield (Y_n) (Ref. 2). To achieve thermonuclear ignition, the alpha-particle heating must exceed the energy losses from the hot spot.[3] The DT fuel in the hot spot must have an areal density high enough to stop the alpha particles leaving the hot spot (typically >300 mg/cm^2), which boosts the core temperature into the ignition regime.[4]

A number of scaling laws have been developed where measurable parameters represent the progress toward fuel conditions necessary for ignition. The simplest of these laws depends on the T_i and ρR described by the 1-D parameter

$$\chi_{1\text{-}D} \approx \rho R^{0.8} \text{ g/cm}^2 \left(\frac{T_i}{4.4} \text{ keV}\right)^{1.8}, \qquad (1)$$

where $\chi_{1\text{-}D} > 1$ defines the ignition threshold.[5] A similar scaling law called ITFX, used on the National Ignition Facility (NIF), gives the probability of ignition as a function of experimental observables.[6,7]

A first approach to infer the areal density from cryogenic DT implosions was to measure the knock-on deuterons and tritons in the colder, dense shell, elastically scattered from the primary neutrons produced in the fusion reaction.[8,9] This technique has an increased uncertainty when the areal density approaches ~200 mg/cm^2 (Ref. 10). Advances in cryogenic implosions, such as using low-adiabat pulses and highly symmetric laser irradiation, have increased the areal density. The higher ρR results in a "leveling off" in the amount of knock-ons that leave the colder, dense shell as a result of the energy loss of the charged particles. An alternative method to infer the areal density in DT cryogenic implosions uses the primary neutrons that elastically scatter off the deuterons and tritons in the dense shell surrounding the hot spot.[1]

The magnetic recoil spectrometer (MRS) was one of the first methods to infer an areal density of >200 mg/cm^2 by measuring the forward-scattered neutron spectrum between 10 to 12 MeV (Ref. 11). This measurement is achieved by placing a plastic foil, either CH or CD, as close as possible to the DT implosion target. The neutrons from the reaction produce recoil protons (or deuterons) that are projected through a focusing magnet. The magnetic field deflects the recoiled protons (deuterons) onto an array of detectors according to their energy. This diagnostic has been successful for areal-density measurements on both OMEGA and the NIF.[12]

Neutron time-of-flight (nTOF) techniques have also been used to measure the areal density on the NIF using the elastically scattered neutron spectrum between 10 and 12 MeV (Ref. 13). These nTOF detectors use a liquid scintillation fluid with special properties to mitigate the long light-afterglow component.[14] Two identical detectors for two separate lines of sight have been calibrated on the OMEGA Laser System before installation on the NIF. The nTOF diagnostics have been successful in measuring the areal density on a large number of NIF cryogenic DT implosions and the results compare favorably with the MRS.

This article reports on a novel nTOF detector that was used for the first time to measure high-resolution, elastically scattered neutron spectra in the 1- to 6-MeV region on cryogenic DT implosions. A well-collimated, 13.4-m line of sight, designed with the aid of the Monte Carlo neutron transport code, and an nTOF detector with low-afterglow liquid scintillator compound were crucial to achieving a high-enough signal to background in the neutron spectrum at these energies. This new diagnostic is able to measure the areal density in the region from 50 to 250 mg/cm^2—typical values achieved in recent experiments where re-scattering of the scattered neutrons was negligible. Future experiments will result in higher areal densities (<1 g/cm^2). Less than 1% of the backscattered neutrons are being re-scattered even at these high areal densities, which will not reduce the accuracy of the areal-density measurements with this diagnostic. Multiple scattering becomes relevant only with areal densities well above 1 g/cm^2. Furthermore, simultane-

ous areal-density measurements from the MRS and the nTOF, which view the target from different directions, will allow for the study of asymmetric implosions on OMEGA.

The ICF neutron energy spectrum of cryogenic DT implosions and the method used to infer the areal density from the elastically scattered neutrons will be described in the next section. The remaining sections will (1) describe the nTOF diagnostic design along with an improved shielded environment with a collimated line of sight that will minimize unwanted neutron scattering; (2) discuss the detector calibration method and the approach used to infer the areal density; and (3) present a summary and a short outlook on future work.

Inferring ρR from the ICF Neutron Energy Spectrum

The primary DT neutrons are generated from the fusion reaction[4]

$$D + T \longrightarrow He^4(3.53\,\text{MeV}) + n(14.06\,\text{MeV}). \qquad (2)$$
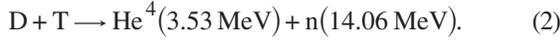
A small fraction of the primary DT neutrons elastically scatter off the dense shell consisting of deuterons and tritons:

$$\begin{aligned}
n + D &\longrightarrow n'(1.56 - 14.06\,\text{MeV}) + D'(<12.50\,\text{MeV}), \\
n + T &\longrightarrow n'(3.53 - 14.06\,\text{MeV}) + T'(<10.53\,\text{MeV}).
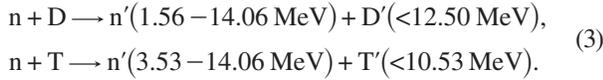\end{aligned} \qquad (3)$$

Specifically, the number of down-scattered neutrons is given by

$$Y_{n'} = Y_n(r) \int_0^\infty \int_0^R (\sigma_d n_d + \sigma_t n_t)\,dr\,dt, \qquad (4)$$

where $Y_n(r)$ is the quantity of 14.06-MeV neutrons at the radius r, σ_d and σ_t are the total elastic cross sections for the (n,d) and (n,t) interactions, with n_d and n_t the fuel ion density distributions. A simple derivation relates the areal density $\langle \rho R \rangle$ to the down-scattered neutrons' fraction[9]

$$\langle \rho R \rangle = 5 \frac{m_p}{(\sigma_d + \sigma_t)} \frac{Y_{n'}}{Y_n}\,\text{mg/cm}^2, \qquad (5)$$

where m_p is the mass of the proton and σ_d and σ_t are the cross sections for neutron scattering off deuterium and tritium, respectively. The areal density is proportional to total down-scattered neutron fraction $Y_{n'}$ over the DT primary neutron yield Y_n. For average areal densities of <0.3 g/cm², typical for experiments on OMEGA, the primary neutrons typically experience no more than a single scatter event while leaving the compressed shell; double scattering is negligible. The kinematic

end point of these neutrons scattered from the dense DT shell is 3.53 MeV and 1.56 MeV, for scattering off the triton and deuteron, respectively, as calculated from[15]

$$\frac{E_{n'}}{E_n} = \frac{4A}{(1+A)^2} \cos^2\theta, \qquad (6)$$

where $E_{n'}$ is the energy of the neutron after scattering, A is the atomic mass of the target nuclei (i.e., D to T), and θ is the recoil angle of the nucleus in the lab frame. The kinematic edge is defined by the value of $E_{n'}$ for $\theta = 0$, or the point at which maximum energy transfer occurs.

An example of the calculated neutron spectrum for a cryogenic DT implosion with an areal density of 220 mg/cm² and a T_i of 2.4 keV is shown in Fig. 131.23.
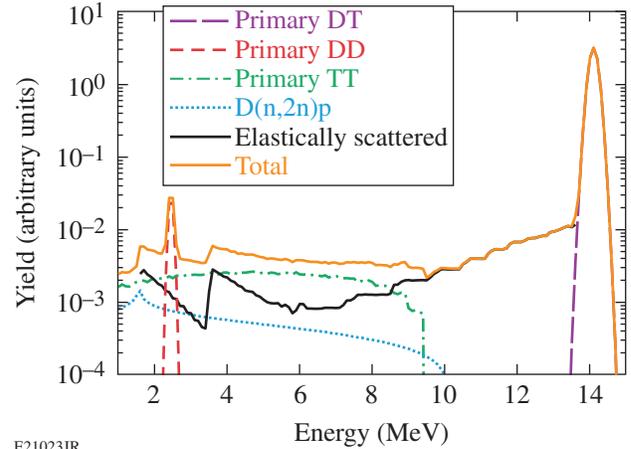
E21023JR

Figure 131.23
The neutron spectrum of a cryogenic DT implosion is generated from 1-D *LILAC* hydrodynamic simulations using the Monte Carlo postprocessor *IRIS*. This spectrum includes the primary DT peak (purple), DD peak (red), and TT neutron feature (green). A fraction (black) of the primary DT neutrons elastically scatter off the dense DT shell. The deuteron breakup reaction (light blue) becomes relevant below 2 MeV. These individual reactions result in the total neutron energy spectrum (orange).

This spectrum was generated using 1-D *LILAC* simulations and post-processed in *IRIS*.[16] The largest contribution to the neutron spectrum comes from the primary D–T fusion reaction at 14.06 MeV. A second primary peak is the D–D fusion reaction at 2.45 MeV followed by the T–T fusion reaction, which is assumed isotropic, and shows a broad energy distribution with a range from 0 to 9.8 MeV (Ref. 17). The elastically scattered neutrons span the entire energy spectrum from 1 to 14.06 MeV.

The deuteron breakup, D(n,2n)p reaction, becomes important below 2 MeV.

The nD and nT elastic cross sections have been measured recently with high accuracy on OMEGA using DT-filled, thin-glass targets.[18] For DT cryogenic implosions, the backscattered neutrons probe the fuel assembly in the 1- to 6-MeV region (150° to 180°).

Setup of the Neutron Time-of-Flight Detector

A time-of-flight spectrum (Fig. 131.24) for a detector at 13.4 m from the target was generated from the neutron energy distribution discussed in the previous section.
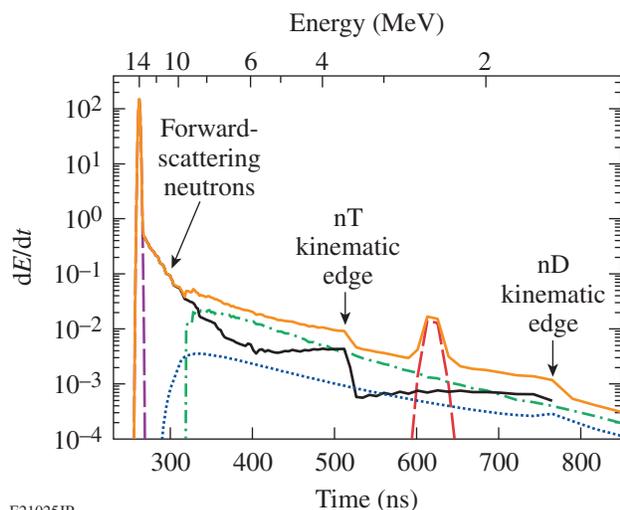
Figure 131.24

A neutron time-of-flight spectrum generated for cryogenic DT implosions on OMEGA with a detector positioned 13.4 m from target chamber center. The primary DT peak (purple), primary DD peak (red), and TT spectrum (green) are generated by fusion reactions. The elastically scattered primary neutrons (black) extend ~10^5 down from the primary DT peak. Below 2 MeV (~700 ns) the deuteron breakup (blue) inelastic reaction becomes relevant. The total neutron spectrum (orange) is the combination of these individual contributions.

The time-of-flight spectrum in Fig. 131.24 illustrate a number of difficulties when trying to measure neutrons over a dynamic range of 10^5 while maintaining sensitivity in the instrument. One issue is the dominant DT peak that accounts for more than 90% of the neutron energy deposited in the detector. Such a large impulse will saturate the photomultiplier tube (PMT) and produce a long light-afterglow component in the scintillator.[13] The lower-energy neutrons in the detector are masked by the afterglow component from the primary peak that is still present from the scintillation process. Another consideration for high-yield DT implosions is the neutron scat-

tering from the target chamber walls and surrounding concrete structures. Three crucial innovations were needed to achieve high-resolution measurements of the neutron energy spectrum.

A gated PMT was used to exclude the primary DT peak from the time-of-flight signal, similar to the detector setup used for fast-ignitor experiments.[13] The microchannel plate (MCP) PMT is gated by applying a positive voltage to the photocathode. The photoelectrons are attracted back toward the photocathode and will not reach the MCP.[19] Once the primary peak has passed, the bias returns to normal and the PMT generates a signal.

Even with the DT peak gated out of the detector, remnants of the scintillation light from the primary DT signal are still evident. To mitigate the long light-afterglow component, advanced scintillating compounds were developed. Oxygenated xylene has been used to reduce the long light-afterglow component by a factor of 10^5 approximately 100 ns after the primary peak.[14]

These modifications led to the construction of a second-generation time-of-flight diagnostic. A computer-aided drawing (CAD) (shown in Fig. 131.25) illustrates the components of the nTOF detector's final design. A significant modification from the first-generation nTOF detector used for the fast-ignitor campaign is a stainless-steel housing lined with gold. The liner is intended to eliminate any possible reaction from the oxygenated xylene that would alter the sensitivity of the detector. The cavity for the nTOF detector is 15 cm in diameter and 5 cm deep. Scintillation
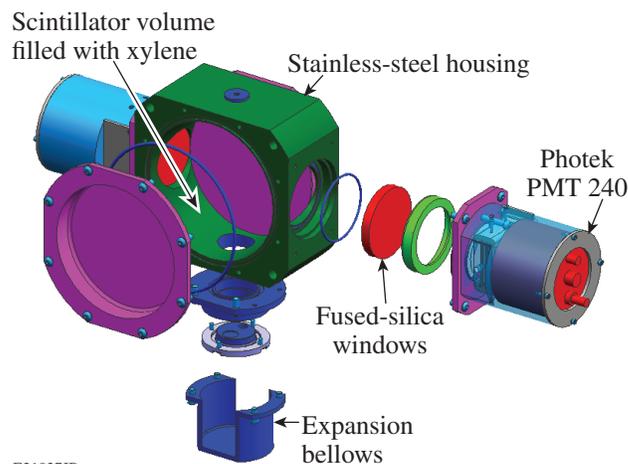
Figure 131.25

A computer-aided design (CAD) of the nTOF detector shows a cavity for the scintillation fluid, the fused-silica windows, and the photomultiplier tube (PMT) mounts. The detector is mounted to the ceiling underneath the Target Bay in a shielded environment to minimize unwanted neutron scattering similar to the setup used in the fast-ignitor experiment.

light from the incident neutrons is viewed through fused-silica windows where the light is coupled to two 40-mm-diam PMT's.

The instrument must be positioned close enough to target chamber center to achieve high neutron statistics but far enough away to interpret the individual components of the energy spectrum. On OMEGA, the maximum distance available for time-of-flight experiments is 13.4 m from the target chamber center. The final necessary modification was to improve the collimation along the line of sight. A Monte Carlo code (MCNP)[20] is used to model the relevant structures in the OMEGA Target Bay and the area underneath the Target Bay. MCNP, developed by the Los Alamos Monte Carlo Group, is used extensively in the nuclear community. This code was cross checked with Geant4 to ensure that the neutron cross sections were in agreement.[21] The simulations showed that the signal to background can be improved by the introduction of a mid-beam collimator. A diagram of the current nTOF detector and mid-beam collimator is shown in Fig. 131.26. The mid-beam collimator has a 60-cm-sq cross section and is ~70 cm in length. It is constructed from high-density polyethylene with a density of ~0.95 g/cm^3. It is mounted on a stand located in the OMEGA Target Bay with semi-permanent mounts. Comparison of data from experiments with and without the mid-beam collimator shows an increase in signal to background by a factor of 2, as shown in Fig. 131.27.

It was determined that a part of the large background was a result of the primary DT neutrons scattering off the target chamber walls. The mid-beam collimator reduced the field of view as seen by the nTOF from the target chamber to provide

Figure 131.27
Simulations identify the large background resulting from the primary DT neutrons scattering from the target chamber. The models in MCNP included a simulation with (red) and without (blue) a mid-beam collimator. These results were then compared with experimental results (black symbols). The signal to background was in good agreement between simulations and data.

an improved signal to background used to measure the DD and backscattered neutron spectra. A second collimator has been considered for placement inside the target chamber to further reduce neutron scattering from the structures (diagnostics) surrounding the cryogenic target. This will be modeled in MCNP to simulate the effects of this additional collimation needed to further improve the signal to background.

The signals from the PMT's are recorded by a 1-GHz Tektronix DPO-7104 digital oscilloscope. Measurements from recent cryogenic DT experiments are shown in Fig. 131.28. The combination of a gated PMT, an advanced scintillation fluid, and the mid-beam collimator in the clear line of sight made it possible to measure a high-resolution neutron spectrum with good signal to background. The DT peak at ~260 ns is suppressed by the gate. A check of the influence of the gating of PMT's on the nTOF signal was performed by adjusting the timing offset of the gate signals on two nominally identical PMT's. The time-of-flight spectrum indicates that after 50 ns the PMT's are fully recovered.

ρR Measurements Using BackScattered Neutron Yields

The nTOF detector must be calibrated before each use on cryogenic DT campaigns since there is evidence that the scintillating fluid exhibits a depletion of oxygen. A loss of oxygen in the xylene affects the sensitivity of the light-emission process and results in an increased long light-afterglow component. This combination of enhanced sensitivity and longer light decay
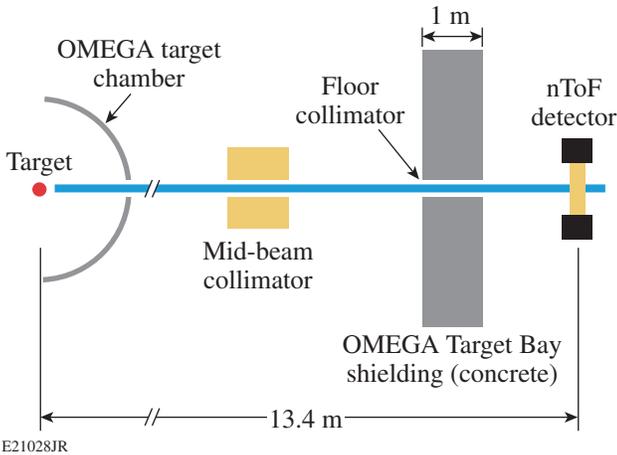

Figure 131.26
A schematic of the target chamber shows the concrete shielding, the nTOF detector's clear line of sight, and the mid-beam collimator. It was determined that the primary DT neutrons scatter off the target chamber walls and produce a large background signal in the nTOF.
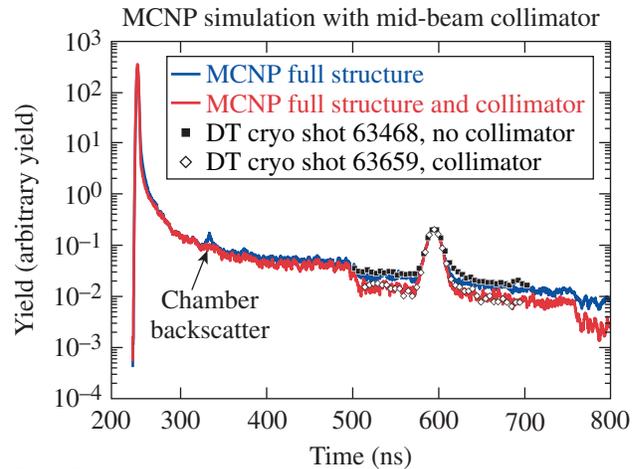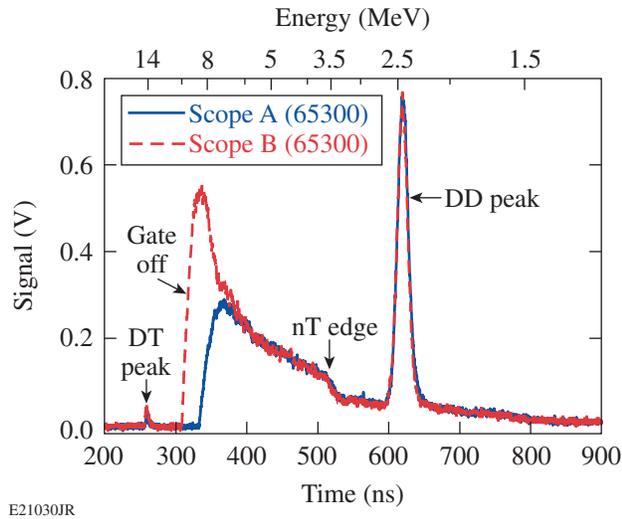
Figure 131.28
To suppress the DT neutron peak, a timing gate is applied to the PMT. The gate recovery has been measured using two PMT 240's, where the time was purposefully offset: PMT A (blue) and PMT B (red). It is clear both PMT's are recovered within 50 ns after the gating is switched off.

will impact the accuracy of the neutron-yield measurement. For this calibration, two D_2-filled targets were imploded with yields that differ by a factor of ~10 to check the linearity of the nTOF detector. A separate detector located in the Target Bay accurately measures the primary neutron yield. Over a six-month period the detector calibration factor changed by ~20%. At this time, it is unclear what causes the xylene to lose the oxygen pressure inside the detector volume.

Recent cryogenic DT implosions have produced neutron yields approaching 1×10^{13} using improved target-positioning procedures and optimized laser pulse shapes on OMEGA.[22] To extract quantitative information from the nTOF signal, the observed spectra are fitted using two of the theoretical components outlined in Fig. 131.24. The first component is the TT spectrum, which is well approximated by a decaying exponential $A \exp(-t/\tau)$ at energies below 6 MeV. The contribution of the TT primary reaction is dependent on the reactivity rate and increases as a function of T_i^4. For this analysis, the overall shape of the spectrum is assumed to be fixed, while the amplitude is scaled from the 1-D simulations where an ion temperature of 2.4 keV was used.

The second component is the down-scattered spectrum that includes both the nT and nD contributions. Since tritium has a half-life of 12.3 years, the fuel D:T ratio changes by ~5% per year. Therefore, it is required to change the nT and nD contributions according to the changing deuterium/tritium fraction

in the DT fuel. This scattered neutron contribution is used to infer the areal density in the nTOF detector. The nT kinematic edge is clearly visible and provides a well-defined region for an accurate fit. An additional background is used to account for the remaining neutron scattering from surrounding structures and remnants of scintillator light decay. The background was found to be quite stable over a number of shots spanning several months. The shape of the background is assumed to be a constant exponential decay, where the amplitude is scaled with the primary DT neutron yield.

This method provides a very good fit to the nTOF spectrum using 1-D simulations as a basis. A number of measurement uncertainties must be considered to obtain an estimate on the accuracy of this analysis. The primary DT neutron yield, needed to adjust the background component, is measured to an accuracy of 5% (Ref. 23). The light output from the scintillator is assumed to be proportional to the energy of the incident neutrons. Given the finite thickness of the scintillator, up to 50% of the incident neutrons pass through the scintillator without any interaction. Since the interaction cross section of neutrons with the scintillator material is a function of the neutron energy, a small correction for the changing interaction probability must be applied to obtain a more-accurate description of the light output. Preliminary simulations of this effect using MCNP with the current xylene nTOF detector indicate that the proportionality assumption introduces an error of ~5%. The best fit to nTOF data is obtained by performing minimization of the error sum to optimize the TT and down-scattered components. The error associated with this method is approximately 2% according to a χ^2 analysis. The high accuracy of this fit is due in part to the large number of neutrons measured by the detector in this region. Below 6 MeV, the nTOF detectors measure above 1×10^5 elastically scattered neutrons (typical on OMEGA cryogenic DT implosions), which introduces a statistical error of ~2%. Errors in the nD and nT elastic scattering cross sections also affect these areal-density measurements. Recent measurements improved the accuracy of the differential nD and nT cross sections, especially at a scattering angle of 180°, to ~10% (Ref. 18). Adding these errors in quadrature gives an estimated total error of ~15%.

However, a number of other error sources have not yet been quantified. The shape of the TT neutron spectrum is not yet well known, which introduces some uncertainty in the fit component. A third theoretical component of the neutron energy spectrum, not included in the fit, is the deuteron breakup reaction D(n,2n)p. This nuclear component will affect the fit primarily in the region below 2 MeV (~700 ns) as seen in Fig. 131.29.
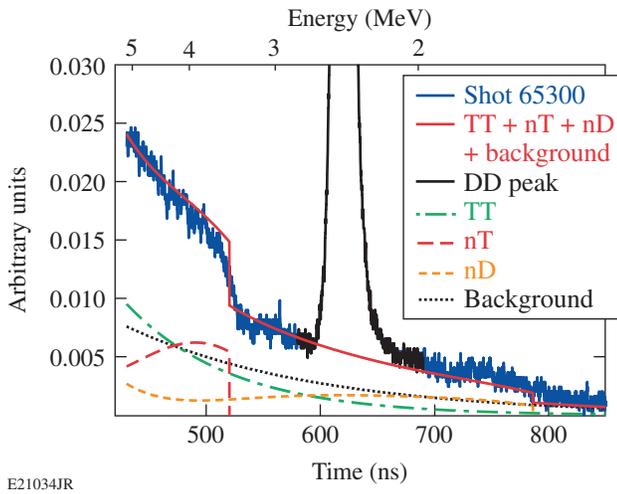
Figure 131.29
Recent nTOF neutron spectra from a DT cryogenic implosion (blue). The DD peak is excluded in this analysis (black). The TT spectrum (green) and the down-scattered component, a combination of the nT and nD spectra (red) are fitted to the experimental data. An additional background component is used that includes any remaining scintillator light decay and neutron scattering (dotted black line). The solid red line illustrates the best fit to this data.

The scattered neutron nTOF diagnostic measured the areal density on a number of recent cryogenic DT implosions on OMEGA. Table 131.V compares the MRS and nTOF data. The comparison between the MRS and nTOF measurements shows

Table 131.V: Predicted ρR obtained from 1-D simulations compared with experimental results from MRS and nTOF. The values from the MRS and nTOF show good agreement. The large ρR difference between nTOF and MRS seen in shots 65578 and 65889 is most likely a result of a target position offset and a misfire on a single beam.

Shot number	1-D prediction (mg/cm^2)	MRS (mg/cm^2)	nTOF (mg/cm^2)
64668	215	163±33	160±32
64669	235	216±30	200±40
65300	210	162±20	160±32
65576	208	155±17	150±30
65578	215	153±15	100±20
65883	190	182±20	160±32
65884	220	126±25	120±24
65887	223	158±21	130±26
65889	216	197±15	140±28

good agreement except for some discrepancies in shots 65578 and 65889. The disagreement in the areal density is most likely a result of the target offset and the misfire of a single laser beam causing significant ρR asymmetry. These asymmetries are possible because the MRS and nTOF probe different regions of the shell's areal density.

Summary

High-resolution neutron time-of-flight spectroscopy has been developed at LLE to measure the areal density of OMEGA cryogenic DT implosions. The time-of-flight spectrum of the elastically scattered neutrons is fitted with theoretical spectral components from well-known nuclear processes to infer the areal density. Increased shielding and collimation have significantly reduced the background in nTOF detectors. Initial results indicate the neutron diagnostics (nTOF's) perform very well and have good agreement with the MRS.

A number of improvements are planned for the scattered neutron nTOF system: A new liquid scintillator nTOF detector housing has been designed with a larger scintillator volume and dual PMT's mounted closer to the scintillation fluid than the current design. An additional collimator installed inside the target chamber is under consideration to further reduce the neutron scattering from inside the target chamber. This will be modeled in MCNP to see how much improvement the additional collimation will provide in the signal to background. The increased scintillator volume and better collimation will potentially allow for higher forward- and backscattered neutron statistics with one detector in a single line of sight. For these measurements one of the two PMT's shown in Fig. 131.25 will be replaced with a less-sensitive PMT-140. This PMT-140 will be used to measure the forward-scattered neutrons close to the primary peak. The remaining PMT-240 will measure the lower-energy backscattered neutron spectrum. Additionally, a joint effort between LLNL and LLE is underway to qualify bibenzyl for use in an nTOF detector. Bibenzyl is a new organic scintillator material that shows significantly reduced light-afterglow decay components. Finally, implosion experiments are planned with pure tritium fill to improve the accuracy of the TT fusion neutron energy spectrum.

REFERENCES

1. V. Yu. Glebov, D. D. Meyerhofer, T. C. Sangster, C. Stoeckl, S. Roberts, C. A. Barrera, J. R. Celeste, C. J. Cerjan, L. S. Dauffy, D. C. Eder, R. L. Griffith, S. W. Haan, B. A. Hammel, S. P. Hatchett, N. Izumi, J. R. Kimbrough, J. A. Koch, O. L. Landen, R. A. Lerche, B. J. MacGowan, M. J. Moran, E. W. Ng, T. W. Phillips, P. M. Song, R. Tommasini, B. K. Young, S. E. Caldwell, G. P. Grim, S. C. Evans, J. M. Mack, T. Sedillo, M. D. Wilke, D. C. Wilson, C. S. Young, D. Casey, J. A. Frenje, C. K. Li, R. D. Petrasso, F. H. Séguin, J. L. Bourgade, L. Disdier, M. Houry, I. Lantuejoul, O. Landoas, G. A. Chandler, G. W. Cooper, R. J. Lepeer, R. E. Olson, C. L. Ruiz, M. A. Sweeney, S. P. Padalino, C. Horsfield, and B. A. Davis, Rev. Sci. Instrum. **77**, 10E715 (2006).

2. C. D. Zhou and R. Betti, Phys. Plasmas **15**, 102707 (2008).

3. T. C. Sangster, R. Betti, R. S. Craxton, J. A. Delettrez, D. H. Edgell, L. M. Elasky, V. Yu. Glebov, V. N. Goncharov, D. R. Harding, D. Jacobs-Perkins, R. Janezic, R. L. Keck, J. P. Knauer, S. J. Loucks, L. D. Lund, F. J. Marshall, R. L. McCrory, P. W. McKenty, D. D. Meyerhofer, P. B. Radha, S. P. Regan, W. Seka, W. T. Shmayda, S. Skupsky, V. A. Smalyuk, J. M. Soures, C. Stoeckl, B. Yaakobi, J. A. Frenje, C. K. Li, R. D. Petrasso, F. H. Séguin, J. D. Moody, J. A. Atherton, B. D. MacGowan, J. D. Kilkenny, T. P. Bernat, and D. S. Montgomery, Phys. Plasmas **14**, 058101 (2007).

4. S. Atzeni and J. Meyer-ter-Vehn, *The Physics of Inertial Fusion: Beam Plasma Interaction, Hydrodynamics, Hot Dense Matter*, International Series of Monographs on Physics (Clarendon Press, Oxford, 2004).

5. R. Betti, P. Y. Chang, B. K. Spears, K. S. Anderson, J. Edwards, M. Fatenejad, J. D. Lindl, R. L. McCrory, R. Nora, and D. Shvarts, Phys. Plasmas **17**, 058102 (2010).

6. S. W. Haan, J. D. Lindl, D. A. Callahan, D. S. Clark, J. D. Salmonson, B. A. Hammel, L. J. Atherton, R. C. Cook, M. J. Edwards, S. Glenzer, A. V. Hamza, S. P. Hatchett, M. C. Herrmann, D. E. Hinkel, D. D. Ho, H. Huang, O. S. Jones, J. Kline, G. Kyrala, O. L. Landen, B. J. MacGowan, M. M. Marinak, D. D. Meyerhofer, J. L. Milovich, K. A. Moreno, E. I. Moses, D. H. Munro, A. Nikroo, R. E. Olson, K. Peterson, S. M. Pollaine, J. E. Ralph, H. F. Robey, B. K. Spears, P. T. Springer, L. J. Suter, C. A. Thomas, R. P. Town, R. Vesey, S. V. Weber, H. L. Wilkens, and D. C Wilson, Phys. Plasmas **18**, 051001 (2011).

7. M. J. Edwards, J. D. Lindl, B. K. Spears, S. V. Weber, L. J. Atherton, D. L. Bleuel, D. K. Bradley, D. A. Callahan, C. J. Cerjan, D. Clark, G. W. Collins, J. E. Fair, R. J. Fortner, S. H. Glenzer, S. W. Haan, B. A. Hammel, A. V. Hamza, S. P. Hatchett, N. Izumi, B. Jacoby, O. S. Jones, J. A. Koch, B. J. Kozioziemski, O. L. Landen, R. Lerche, B. J. MacGowan, A. J. MacKinnon, E. R. Mapoles, M. M. Marinak, M. Moran, E. I. Moses, D. H. Munro, D. H. Schneider, S. M. Sepke, D. A. Shaughnessy, P. T. Springer, R. Tommasini, L. Bernstein, W. Stoeffl, R. Betti, T. R. Boehly, T. C. Sangster, V. Yu. Glebov, P. W. McKenty, S. P. Regan, D. H. Edgell, J. P. Knauer, C. Stoeckl, D. R. Harding, S. Batha, G. Grim, H. W. Herrmann, G. Kyrala, M. Wilke, D. C. Wilson, J. Frenje, R. Petrasso, K. Moreno, H. Huang, K. C. Chen, E. Giraldez, J. D. Kilkenny, M. Mauldin, N. Hein, M. Hoppe, A. Nikroo, and R. J. Leeper, Phys. Plasmas **18**, 051003 (2011).

8. S. Skupsky and S. Kacenjar, J. Appl. Phys. **52**, 2608 (1981).

9. C. K. Li, F. H. Séguin, D. G. Hicks, J. A. Frenje, K. M. Green, S. Kurebayashi, R. D. Petrasso, D. D. Meyerhofer, J. M. Soures, V. Yu.

Glebov, R. L. Keck, P. B. Radha, S. Roberts, W. Seka, S. Skupsky, C. Stoeckl, and T. C. Sangster, Phys. Plasmas **8**, 4902 (2001).

10. J. A. Frenje, C. K. Li, F. H. Séguin, D. T. Casey, R. D. Petrasso, T. C. Sangster, R. Betti, V. Yu. Glebov, and D. D. Meyerhofer, Phys. Plasmas **16**, 042704 (2009).

11. J. A. Frenje, D. T. Casey, C. K. Li, J. R. Rygg, F. H. Séguin, R. D. Petrasso, V. Yu. Glebov, D. D. Meyerhofer, T. C. Sangster, S. Hatchett, S. Haan, C. Cerjan, O. Landen, M. Moran, P. Song, D. C. Wilson, and R. J. Leeper, Rev. Sci. Instrum. **79**, 10E502 (2008).

12. J. A. Frenje, D. T. Casey, C. K. Li, F. H. Séguin, R. D. Petrasso, V. Yu. Glebov, P. B. Radha, T. C. Sangster, D. D. Meyerhofer, S. P. Hatchett, S. W. Haan, C. J. Cerjan, O. L. Landen, K. A. Fletcher, and R. J. Leeper, Phys. Plasmas **17**, 056311 (2010).

13. C. Stoeckl, M. Cruz, V. Yu. Glebov, J. P. Knauer, R. Lauck, K. Marshall, C. Mileham, T. C. Sangster, and W. Theobald, Rev. Sci. Instrum. **81**, 10D302 (2010).

14. R. Lauck *et al.*, IEEE Trans. Nucl. Sci. **56**, 989 (2009).

15. G. F. Knoll, *Radiation Detection and Measurement*, 3rd ed. (Wiley, New York, 2000).

16. J. Delettrez, R. Epstein, M. C. Richardson, P. A. Jaanimagi, and B. L. Henke, Phys. Rev. A **36**, 3926 (1987); P. B. Radha, J. A. Delettrez, R. Epstein, S. Skupsky, J. M. Soures, S. Cremer, and R. D. Petrasso, Bull. Am. Phys. Soc. **44**, 194 (1999).

17. G. R. Caughlan and W. A. Fowler, At. Data Nucl. Data Tables **40**, 283 (1988).

18. J. A. Frenje, C. K. Li, F. H. Séguin, D. T. Casey, R. D. Petrasso, D. P. McNabb, P. Navratil, S. Quaglioni, T. C. Sangster, V. Yu. Glebov, and D. D. Meyerhofer, Phys. Rev. Lett. **107**, 122502 (2011).

19. Photek Ltd., St. Leonards-on-Sea, East Sussex, TN38 9NS, United Kingdom.

20. Los Alamos Monte Carlo Group, "MCNP-A General Monte Carlo N-Particle Transport Code Version 5," Los Alamos National Laboratory Vols. I-III, April, 2003. Available from Radiation Safety Information Computational Center at Oak Ridge National Laboratory as CCC-740.

21. S. Agostinelli *et al.*, Nucl. Instrum. Methods Phys. Res. A 506, 250 (2003).

22. T. C. Sangster, V. N. Goncharov, R. Betti, T. R. Boehly, D. T. Casey, T. J. B. Collins, R. S. Craxton, J. A. Delettrez, D. H. Edgell, R. Epstein, K. A. Fletcher, J. A. Frenje, V. Yu. Glebov, D. R. Harding, S. X. Hu, I. V. Igumenshchev, J. P. Knauer, S. J. Loucks, C. K. Li, J. A. Marozas, F. J. Marshall, R. L. McCrory, P. W. McKenty, D. D. Meyerhofer, P. M. Nilson, S. P. Padalino, R. D. Petrasso, P. B. Radha, S. P. Regan, F. H. Séguin, W. Seka, R. W. Short, D. Shvarts, S. Skupsky, V. A. Smalyuk, J. M. Soures, C. Stoeckl, W. Theobald, and B. Yaakobi, Phys. Plasmas **17**, 056312 (2010).

23. O. Landoas, V. Yu. Glebov, B. Rossé, M. Briat, L. Disdier, T. C. Sangster, T. Duffy, J. G. Marmouget, C. Varignon, X. Ledoux, T. Caillaud, I. Thfoin, and J.-L. Bourgade, Rev. Sci. Instrum. **82**, 073501 (2011).

Experimental Validation of the Two-Plasmon–Decay Common-Wave Process

Direct-drive inertial confinement fusion (ICF) requires multiple overlapping laser beams that can then drive two-plasmon–decay (TPD) instability. TPD creates large-amplitude electron plasma waves in the region near quarter-critical density.[1] These plasma waves can lead to anomalous absorption and hot-electron generation[2,3] that can preheat the fusion fuel and reduce the compression efficiency. Understanding the behavior of TPD is critical to mitigating it in ICF experiments.

TPD instability consists of the decay of an electromagnetic wave into two electron plasma waves.[4,5] Phase matching, energy conservation, and the dispersion relations of the waves limit the instability to a small region near quarter-critical density. Stability calculations of a single-plane electromagnetic wave show that the spatial growth rate of instability is proportional to the quantity IL_n/T_e, where I is the laser-beam intensity, L_n is the plasma density scale length, and T_e is the electron temperature of the plasma.[6,7] When the instability is driven to nonlinear saturation, a broad spectrum of large-amplitude plasma waves is generated.[8] The large electrostatic fields associated with these electron plasma waves can accelerate electrons to high energies (~100 keV) (Ref. 9).

When multiple overlapping laser beams with polarization smoothing were used,[10] the total energy in hot electrons was shown to scale with the overlapped intensity (I_Σ), defined as the sum of the intensity of each beam.[11] This scaling would not be expected if the beams drive the TPD independently, according to the growth rates of the single plane waves. A model is proposed where different laser beams share a common electron wave.[12] As the plasma wave is driven by multiple electromagnetic waves, the TPD growth rate can be larger than when driven by an individual beam. This was observed in nonlinear Zakharov simulations.[8]

This article describes the first experimental validation of the common-wave process [Fig. 131.30(a)], where the total energy in hot electrons was measured to be similar when one or two polarized beams were used at the same overlapped intensity and significantly reduced when four beams with the same

overlapped intensity were used. Hot electrons generated by four beams are shown to be similar in total energy to the sum of the hot-electron energies generated by the six possible two-beam interactions [Fig. 131.30(b)]. A theoretical description of the common-wave process shows that multiple laser beams can share an electron-plasma wave in the region bisecting the electromagnetic wave vectors. For two beams, this region defines a plane [Fig. 131.30(a)]; for four beams, it defines a line
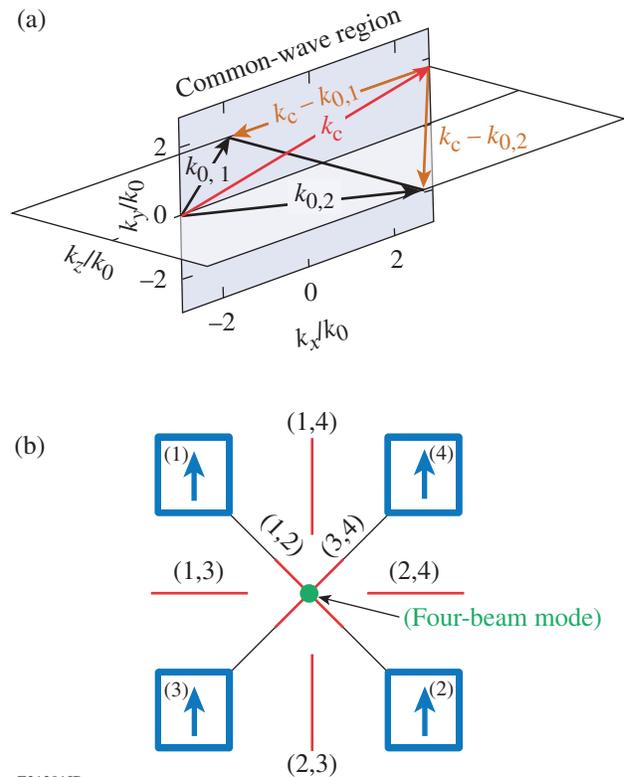
Figure 131.30
(a) Schematic of the common-wave region for two beams. Two laser beams of wave vectors $k_{0,1}$ and $k_{0,2}$ share the common plasma wave k_c located in the bisecting plane, fulfilling the necessary condition $\left| k_c - k_{0,1} \right| = \left| k_c - k_{0,2} \right|$ independent of the polarizations of the laser beams. (b) Schematic of the seven common-wave regions when four beams were used: six two-beam common-wave planes (red lines) and one four-beam common-wave line (green point).

[Fig. 131.30(b)]. In this region, the temporal growth rate and convective gain of the dominant mode are proportional to the overlapped intensity, a factor that depends on the geometry, the polarization, and the relative intensity of the laser beams.

The experiments were conducted on OMEGA EP,[13] where the four 351-nm beams were polarized vertically and intersected the target at an angle of 23° with respect to the target normal [Fig. 131.30(b)]. The beams were spatially overlapped to within 20 μm and used 2-ns flattop laser pulses that were co-timed to within 50 ps. Two sets of distributed phase plates[10] were used (890-μm diameter for Beams 1 and 2 and 840-μm diameter for Beams 3 and 4) to produce an ~1-mm-diam super-Gaussian intensity distribution profile. A maximum single-beam energy of 2 kJ (2.6 kJ) was used on Beams 1 and 2 (3 and 4), which provided a single-beam $I_{max} = 1.6 \times 10^{14}$ W/cm^2 ($I_{max} = 2.4 \times 10^{14}$ W/cm^2). The relative error in intensities of less than 5% was dominated by the shot-to-shot power measurements on each beam. This resulted in a maximum error of 10% in overlapped intensity.

The laser beams illuminated a 30-μm-thick CH layer deposited on 30 μm of Mo and backed with an additional 30 μm of CH. Hydrodynamic simulations using the two-dimensional (2-D) code *DRACO*[14] indicate that the laser light interacted with the first layer, producing a CH plasma with density and temperature profiles that depend only on the overlapped laser intensity. For the experimental conditions presented here, the hydrodynamic profiles near quarter-critical density reached a steady state after about 1.5 ns. After this time, the calculated quantity $I_{\Sigma,q} L_n / T_e$ varied by less than 10%, where $I_{\Sigma,q}$ is the overlapped intensity at the quarter-critical density. When the overlapped laser intensity was increased from 1.5×10^{14} W/cm^2 to 7×10^{14} W/cm^2, L_n increased from 260 μm to 360 μm, T_e increased from 1.5 keV to 2.5 keV, and, due to absorption, the laser intensity at quarter-critical density was about equal to half of the vacuum intensity; the ratio L_n / T_e was nearly constant ($\approx$160 μm/keV).

Two principal diagnostics were used to determine the amount of laser energy converted to hot electrons: the x-ray spectrometer (XRS)[15–17] and the hard x-ray detector (HXRD).[18] The XRS measured the energy emitted into the Mo K$_\alpha$ emission line $\left(E_{K_\alpha}\right)$ using an absolutely calibrated planar LiF crystal spectrometer that viewed the target from the laser incident side at an angle of 63° from the target normal.[17] Monte Carlo (MC) simulations using the code EGSnrc[19] show that electrons with energies less than 120 keV are stopped in the Mo. The 17.5-keV Mo K$_\alpha$ line was sufficiently energetic so that

photoexcitation from the 2.5-keV coronal plasma region did not contribute to the K$_\alpha$-emission measurement. The relative error in E_{K_α} was less than 5% (Ref. 17).

The HXRD consists of a three-channel scintillator that measures the x-ray radiation generated by hot electrons in the Mo above ~40 keV, ~60 keV, and ~80 keV (Ref. 18). It allows one to estimate the hot-electron temperature using the exponentially decreasing x-ray energy in each channel. The relative error in the measurement of the hot-electron temperature was 20%. MC simulations were used to determine the total hot-electron energy (E_e) given the measured hot-electron temperature (T_{hot}) and the total energy in the K$_\alpha$ emission.[17] The relative error of 25% is dominated by measurement errors. Figure 131.31(a) shows that the dependence of the hot-electron temperature with the total energy in K$_\alpha$ was comparable when one, two, or four beams were used.

Figure 131.31(b) shows that the total laser energy (E_l) converted into hot electrons $\left(f_{hot} = E_e / E_l\right)$ as a function of the overlapped intensity was similar when one or two beams were used in the horizontal, vertical, or diagonal configuration and increased exponentially as a function of the overlapped intensity. These results show that TPD growth was caused by the interplay between the two beams through a common-wave process. If the hot electrons were generated by two independent single-beam processes, each with an intensity of $I_\Sigma / 2$, the total hot-electron energy would be the sum of the hot-electron energy generated by each beam. This would be significantly smaller than the hot-electron energy generated by a single beam with I/I_Σ (due to the measured exponential increase of the hot-electron energy with the laser intensity). The fact that the two beams produced a total hot-electron fraction similar to that of a single beam shows that the common-wave process is very efficient.

When comparing the four-beam and single-beam results, Fig. 131.31(b) shows a significant decrease in the hot-electron energy for a given overlapped intensity (up to two orders of magnitude for $I_\Sigma \sim 2 \times 10^{14}$ W/cm^2). This reduction in the four-beam experiments can be explained heuristically on the basis of the two-beam experimental results. The addition of hot-electron fractions measured for six possible two-beam configurations (two horizontal configurations, two vertical configurations, and two diagonal configurations), plotted at twice the overlapped intensity, was consistent with the fraction of hot electrons measured when four beams were employed [see open symbols in Fig. 131.31(b)]. This suggests that the hot electrons generated by four beams were the result of the sum of hot electrons generated by six independent two-beam

interactions; i.e., the hot electrons generated by the interaction between all four beams were not dominant.
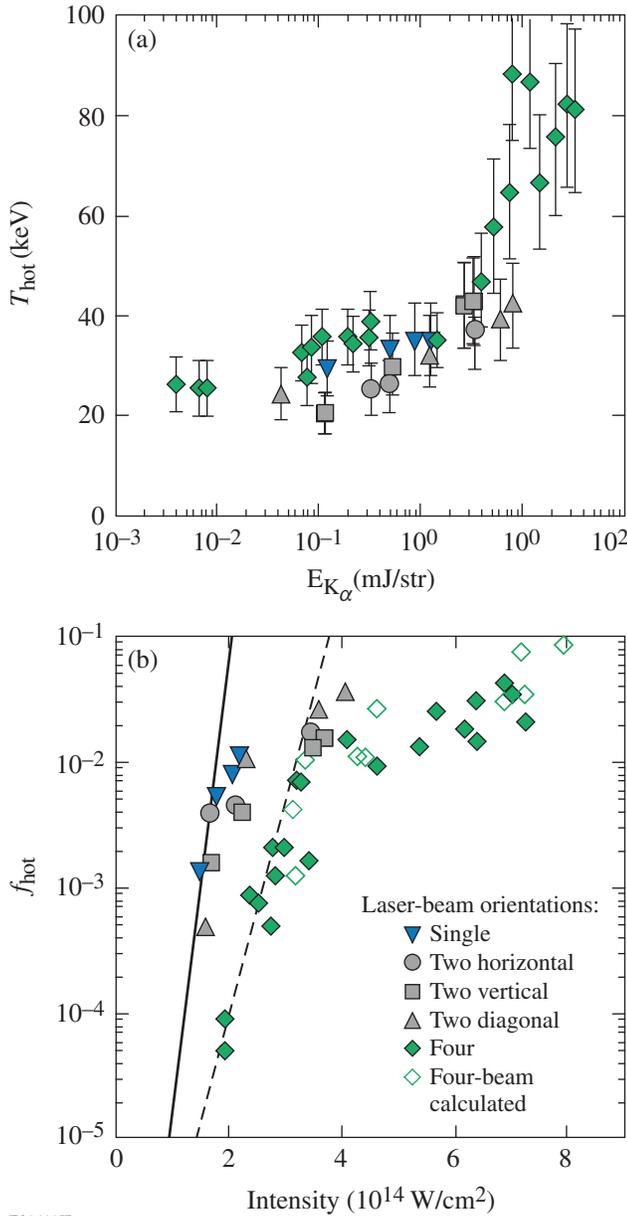
E21411JR

Figure 131.31
(a) The measured hot-electron temperature is plotted as a function of the measured total energy in K_α for the five laser-beam orientations tested. (b) The fraction of laser energy converted to hot electrons (f_{hot}) is plotted as a function of the overlapped intensity. The four-beam hot-electron generation was estimated (open diamonds) by multiplying the measured two-beam total hot-electron energy fraction by 6 and plotting the results at twice the two-beam intensity. The dashed line is a fit to the four-beam data $\left[f_{hot} = 3 \times 10^{-8} \, e^{(8I_\Sigma/2)} \right]$. The solid line is scaled from the fit, assuming the four-beam results are dominated by the six two-beam common-wave modes driven at half of the intensity $\left[f_{hot} = 1 \times 10^{-8} \, e^{(8I_\Sigma)} \right]$.

The well-known theory of TPD[4,5] is based on the dispersion relation for the two electron plasma waves with frequency and wave vectors $(\omega, \mathbf{k})$ and $(\omega - \omega_0, \mathbf{k} - \mathbf{k}_0)$, where ω_0 and $\mathbf{k}_0$ are the frequency and wave vector of the initial electromagnetic wave, respectively.[4,5] In the case of multiple laser beams driving a common electron plasma wave $(\omega_c, \mathbf{k}_c)$, the dispersion relation is $\omega_c^2 = \omega_{pe}^2 + 3\mathbf{k}_c^2 v_{th,e}^2$ and for the corresponding daughter waves $(\omega_c - \omega_0)^2 = \omega_{pe}^2 + 3(\mathbf{k}_c - \mathbf{k}_{0,i})^2 v_{th,e}^2$, where $v_{th,e}$ is the electron thermal velocity, ω_{pe} is the plasma frequency, and $\mathbf{k}_{0,i}$ (with a norm k_0 independent of i) is the wave vector of beam i. A mathematical definition for the region where a resonant common-wave process exists is determined by satisfying the dispersion relations for all laser beams, $\cos(\mathbf{k}_c, \mathbf{k}_{0,i}) = $ const, for $i = 1...n$. For a two-beam configuration, this defines a plane in k-space bisecting the wave vectors of the two laser beams [Fig. 131.30(a)]. For more than two laser beams, this condition either restricts the resonant common waves to a line or eliminates them, depending on the laser beam's symmetry. The four-beam growth rate in this experiment is restricted to a line [Fig. 131.30(b)].

The dispersion relation for the common-wave process is derived following the TPD linear theory[4,5] for conditions where the collision frequency is much smaller than the growth rate, satisfied for our experimental parameters:

$$D\left(\omega_c, \gamma, |\mathbf{k}_c|\right) = -\sum_i \frac{\gamma_{0,i}^2}{D\left(\omega_c - \omega_0, \gamma, |\mathbf{k}_c - \mathbf{k}_{0,i}|\right)},$$

where γ is the temporal growth rate,

$$D\left(\omega, \gamma, |\mathbf{k}|\right) = \left\{ \left[1 - \frac{\omega_{pe}^2}{\omega^2}\left(1 + 3k^2\lambda_{De}^2\right) \right] \frac{\omega}{2} + i\gamma \right\}$$

is the dispersion relation, and $\lambda_{De} = v_{th,e}/\omega_{pe}$ is the Debye length. The single-beam homogeneous growth rate calculated in the common-wave region $\gamma_{0,i}^2 = \left(\gamma_0^2\right)_{max}^{SB} \cos^2(\alpha_i) f_c \beta_i$, where α_i is the angle between the polarization vector and the common-wave vector,

$$f_c = \left[k_c^2 - \left(\mathbf{k}_c - \mathbf{k}_{0,i}\right)^2 \Big/ k_{0,i} | \mathbf{k}_c - \mathbf{k}_{0,i} | \right]^2,$$

$\beta_i = I_i/I_\Sigma$, I_i is the intensity of the laser beam i,

$$\left(\gamma_0^2\right)_{max}^{SB} = 2 \Big/ cn_c m_e \left(k_0/2\right)^2 I_\Sigma$$

is the maximum single-beam homogeneous growth rate squared calculated for the overlapped intensity, c is the light velocity, m_e is the electron mass, $n_c = m_e \omega_0^2 / 4\pi e^2$ is the critical density, and e is the electron charge. To evaluate the maximum value of the growth rate, the minimum value of $D\left(\omega, \gamma, |\mathbf{k}_c - \mathbf{k}_{0,i}|\right)$ is determined by ensuring that the dispersion relations for all daughter waves are satisfied. It follows that $D\left(\omega, \gamma, |\mathbf{k}_c - \mathbf{k}_{0,i}|\right) = i\gamma = \text{const}$ and the resonant common-wave growth rate is given by $\left(\gamma_0^2\right)^{\text{MB}} = \sum_i \gamma_{0,i}^2$. A geometric function is given by normalizing the multiple-beam growth rate squared to the maximum single-beam growth rate squared:

$$\left(\Gamma_0^2\right)^{\text{MB}} = \frac{\left(\gamma_0^2\right)^{\text{MB}}}{\left(\gamma_0^2\right)_{\text{max}}^{\text{SB}}} = f_c \sum_i \cos^2(\alpha_i) \beta_i.$$

The dominant mode is determined by the maximum of the geometric function, which is a geometric factor $f_g = \left(\Gamma_0^2\right)_{\text{max}}^{\text{SB}}$ that depends only on the geometry of the laser beams, their polarizations, and their intensities relative to the overlapped intensity.

Figures 131.32(a) and 131.32(b) show the calculated geometric functions for two beams, $\left(\Gamma_0^2\right)^{2\text{B}}$, polarized perpendicular and parallel to the plane defined by the laser beams $(\mathbf{k}_{0,1}, \mathbf{k}_{0,2})$. The geometric functions calculated in k-space are significantly

different as a result of the difference in the polarization vectors relative to the common-wave plane, although the geometric factor is similar for the two cases, $\left(\Gamma_0^2\right)_{\text{max}}^{2\text{B}} \sim 1$. The fact that the growth rates are the same explains why the total hot-electron energy is measured to be similar in the horizontal and vertical laser-beam configurations. For the configuration with two horizontal beams [Fig. 131.32(a)], the geometric function in the common-wave planes forms two modified hyperbolas defined by

$$\left(k_y/k_0\right)^2 = \left(k_x/k_0\right)\left[\left(k_x/k_0\right)/\cos(\theta/2)^2 - 1\right],$$

where θ is the angle between the two laser beams. The maximum value is located in the backward direction $(-\mathbf{k}_x)$ for small wave vectors. For the configuration with two vertical beams [Fig. 131.32(b)], the maximum value of the geometric function is located at the intersection $\left(k_y/k_0 = 0\right)$ of the two hyperbolas of maximum single-beam growth rates (that are in the polarization plane of each beam). The geometric function decreases rapidly with k_y/k_0, corresponding to the rapid decrease in the single-beam growth rates.

Figure 131.32(c) shows the four-beam geometric function $\left(\Gamma_0^2\right)^{4\text{B}}$ plotted along the four-beam common-wave region located along the line bisecting the laser beams [Fig. 131.30(b)]. The maximum value is reached for $k_x/k_0 \sim 1.3$
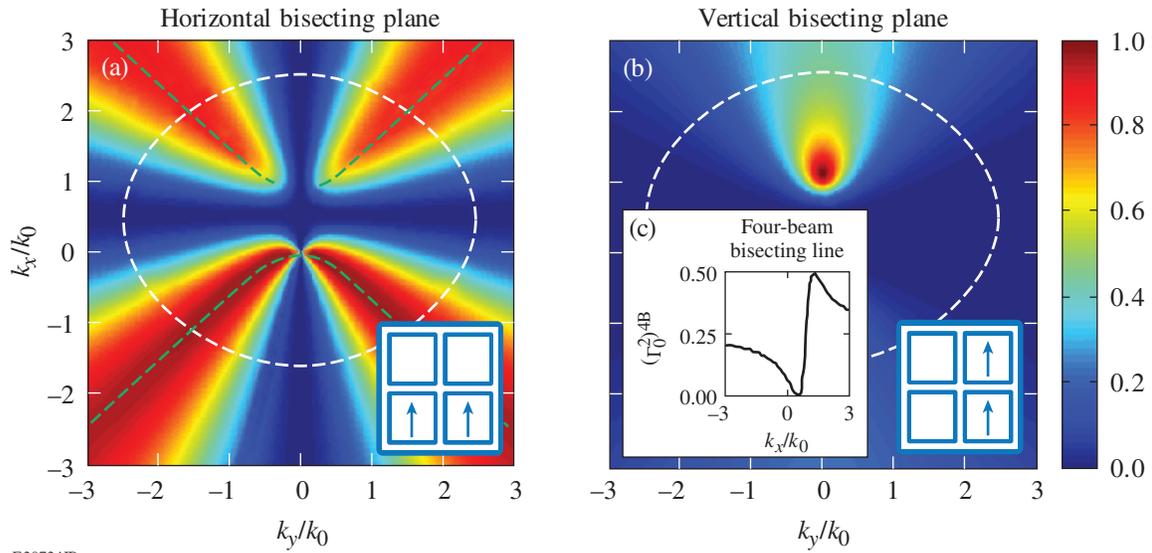
Figure 131.32
Calculation of $\left(\Gamma_0^2\right)^{2\text{B}}$ in the common-wave plane for (a) two beams polarized perpendicular and (b) parallel to the plane $(\mathbf{k}_{0,1}, \mathbf{k}_{0,2})$. The dashed white lines correspond to the Landau cutoff $\left[k_{\text{max}}\lambda_{\text{De}} = 0.25\right.$, where $k_{\text{max}} = \max\left(k_c, |\mathbf{k}_c - \mathbf{k}_{0,i}|\right)]$ calculated for $T_e = 1.6$ keV, which defines the maximum wave vector for TPD.[21] The dashed green lines correspond to the two modified hyperbolas of maximum $\left(\Gamma_0^2\right)^{2\text{B}}$. (c) Calculation of $\left(\Gamma_0^2\right)^{4\text{B}}$ along the four-beam common-wave line. $\mathbf{k}_x$ is along the projection of $\mathbf{k}_{0,i}$ in the common-wave region, $\mathbf{k}_y$ is perpendicular to $\mathbf{k}_x$, and k_0 is calculated at quarter-critical density.

and $k_y / k_0 \sim 0.3$, where $\left(\Gamma_0^2\right)_{\text{max}}^{4B} = 0.5$. For the same overlapped intensity, the single-beam and two-beam homogeneous growth rates for the dominant mode are similar: $\left(\Gamma_0^2\right)_{\text{max}}^{2B} = 1$, whereas the four-beam homogeneous growth rate for the dominant mode is decreased by a factor of 2: $\left(\Gamma_0^2\right)_{\text{max}}^{4B} = 0.5$. These calculations support the experimental findings [Fig. 131.31(b)], where the single and two-beam hot-electron fractions are comparable, while the four-beam hot-electron fraction is smaller.

To estimate the common-wave convective gain (in intensity), the maximum common-wave homogeneous growth rate was used in the formalism derived in Refs. 6 and 20,

$$G = \left(16\pi / 9\right)\left(v_{\text{th,e}}^2 / c^2\right)^{-1} k_0 L \left[\left(\gamma_0^2\right)_{\text{max}}^{\text{MB}} / \omega_0\right]^2 .$$
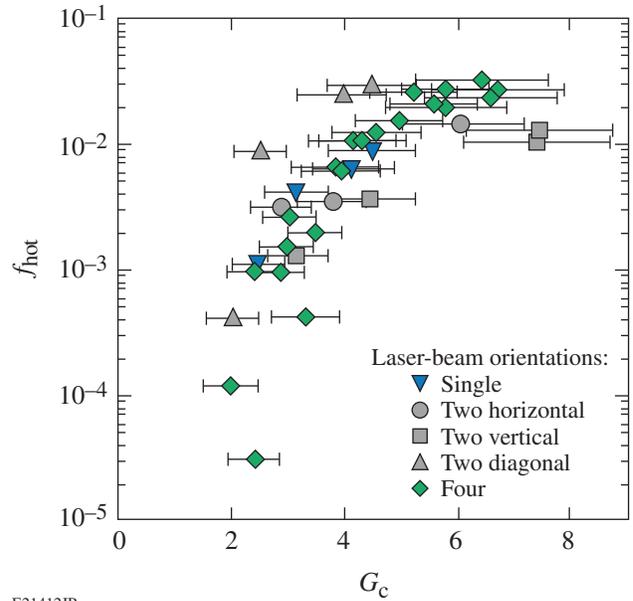
The maximum common-wave gain for each configuration is

$$G_c = 6 \times 10^{-2} \frac{I_{\Sigma,q} L_n \lambda_0}{T_e} f_g ,$$

where T_e is in keV, $I_{\Sigma,q}$ is in 10^{14} W/cm^2, and L_n and λ_0 are in microns. For a given laser-beam configuration (relative beam angle and polarization), the common-wave gain is proportional to $I_{\Sigma,q} L_n / T_e$.

Figure 131.33 shows the hot-electron fraction as a function of the calculated common-wave gain for the dominant mode [Eq. (2)]. When there are multiple common-wave regions, the dominant mode corresponds to the maximum common-wave gain. For all laser-beam configurations, except for two diagonal beams, the hot-electron fraction as a function of the gain is similar. For diagonal beams, the calculations underestimate the value of the gain.

In summary, when maintaining an overlapped-laser-beam intensity, the total energy in hot electrons is measured to be similar when using one or two polarized beams and significantly reduced with four polarized beams. In four-beam experiments, the hot-electron energy was shown to be the result of hot electrons generated by the six possible two-beam interactions; i.e., the hot electrons generated by the interaction between all four beams does not dominate. A linear common-wave model is consistent with these observations, where the homogeneous growth rate for the dominant mode was calculated for beams that share a common plasma wave. The model shows that for two beams, the resonant common electron plasma wave was restricted to the plane bisecting the beams. For more than two beams, the resonant common wave was restricted to a line or could not occur. In this region, the homogeneous growth rate and the convective gain are shown to be proportional to the overlapped intensity and a geometric factor that depends on the geometry, the polarization, and the relative intensity of the laser beams. This is consistent with previous experimental results where hot-electron generation was shown to scale with overlapped intensity.[11] For ignition designs, these results suggest that the common-wave process can be reduced by limiting the number of beams that are symmetric to one another or by reducing the geometric factor.

Figure 131.33
The total hot-electron energy divided by the laser energy plotted as a function of the common-wave gain (G_c) for the dominant mode.

E21412JR

REFERENCES

1. H. A. Baldis and C. J. Walsh, Phys. Rev. Lett. **47**, 1658 (1981).

2. N. A. Ebrahim *et al.*, Phys. Rev. Lett. **45**, 1179 (1980).

3. R. L. Keck, L. M. Goldman, M. C. Richardson, W. Seka, and K. Tanaka, Phys. Fluids **27**, 2762 (1984).

4. M. V. Goldman, Ann. Phys. **38**, 117 (1966).

5. C. S. Liu and M. N. Rosenbluth, Phys. Fluids **19**, 967 (1976).

6. M. N. Rosenbluth, Phys. Rev. Lett. **29**, 565 (1972).

7. A. Simon, R. W. Short, E. A. Williams, and T. Dewandre, Phys. Fluids **26**, 3107 (1983).

8. J. F. Myatt, J. Zhang, J. A. Delettrez, A. V. Maximov, R. W. Short, W. Seka, D. H. Edgell, D. F. DuBois, D. A. Russell, and H. X. Vu, Phys. Plasmas **19**, 022707 (2012).

9. D. H. Froula, B. Yaakobi, S. X. Hu, P.-Y. Chang, R. S. Craxton, D. H. Edgell, R. Follett, D. T. Michel, J. F. Myatt, W. Seka, R. W. Short, A. Solodov, and C. Stoeckl, Phys. Rev. Lett. **108**, 165003 (2012).

10. T. J. Kessler, Y. Lin, J. J. Armstrong, and B. Velazquez, in *Laser Coherence Control: Technology and Applications*, edited by H. T. Powell and T. J. Kessler (SPIE, Bellingham, WA, 1993), Vol. 1870, pp. 95–104.

11. C. Stoeckl, R. E. Bahr, B. Yaakobi, W. Seka, S. P. Regan, R. S. Craxton, J. A. Delettrez, R. W. Short, J. Myatt, A. V. Maximov, and H. Baldis, Phys. Rev. Lett. **90**, 235002 (2003).

12. R. W. Short and J. F. Myatt, Bull. Am. Phys. Soc. **56**, 329 (2011).

13. J. H. Kelly, L. J. Waxer, V. Bagnoud, I. A. Begishev, J. Bromage, B. E. Kruschwitz, T. J. Kessler, S. J. Loucks, D. N. Maywar, R. L. McCrory, D. D. Meyerhofer, S. F. B. Morse, J. B. Oliver, A. L. Rigatti, A. W. Schmid, C. Stoeckl, S. Dalton, L. Folnsbee, M. J. Guardalben, R. Jungquist, J. Puth, M. J. Shoup III, D. Weiner, and J. D. Zuegel, J. Phys. IV France **133**, 75 (2006).

14. P. B. Radha, T. J. B. Collins, J. A. Delettrez, Y. Elbaz, R. Epstein, V. Yu. Glebov, V. N. Goncharov, R. L. Keck, J. P. Knauer, J. A. Marozas, F. J. Marshall, R. L. McCrory, P. W. McKenty, D. D. Meyerhofer, S. P. Regan, T. C. Sangster, W. Seka, D. Shvarts, S. Skupsky, Y. Srebro, and C. Stoeckl, Phys. Plasmas **12**, 056307 (2005).

15. B. Yaakobi, C. Stoeckl, T. Boehly, D. D. Meyerhofer, and W. Seka, Phys. Plasmas **7**, 3714 (2000).

16. B. Yaakobi, T. R. Boehly, T. C. Sangster, D. D. Meyerhofer, B. A. Remington, P. G. Allen, S. M. Pollaine, H. E. Lorenzana, K. T. Lorenz, and J. A. Hawreliak, Phys. Plasmas **15**, 062703 (2008).

17. B. Yaakobi, P.-Y. Chang, A. A. Solodov, C. Stoeckl, D. H. Edgell, R. S. Craxton, S. X. Hu, J. F. Myatt, F. J. Marshall, W. Seka, and D. H. Froula, Phys. Plasmas **19**, 012704 (2012).

18. C. Stoeckl, V. Yu. Glebov, D. D. Meyerhofer, W. Seka, B. Yaakobi, R. P. J. Town, and J. D. Zuegel, Rev. Sci. Instrum. **72**, 1197 (2001).

19. I. Kawrakow *et al.*, NRC, Ottawa, Canada, NRCC Report PIRS-701 (May 2011).

20. R. Yan, A. V. Maximov, and C. Ren, Phys. Plasmas **17**, 052701 (2010).

21. W. Seka, D. H. Edgell, J. F. Myatt, A. V. Maximov, R. W. Short, V. N. Goncharov, and H. A. Baldis, Phys. Plasmas **16**, 052701 (2009).

# A Reflective Optical Transport System for Ultraviolet Thomson Scattering on OMEGA

Introduction

Thomson scattering has become a routine diagnostic in high-energy-density laser–plasma experiments[1–4] for characterizing the electron and ion temperatures by scattering 2ω ($\lambda_{2\omega}$ = 0.527 μm) or 4ω ($\lambda_{4\omega}$ = 0.263 μm) light from ion-acoustic waves.[3,5] Recently the electron density was measured[6] on OMEGA[7] by scattering 2ω light from electron plasma waves, but scattering with a 2ω probe limits these measurements to relatively low densities ($n_e \approx 5 \times 10^{20}$ cm^{-3}).

A reflective optical transport system recently implemented on the OMEGA Thomson-scattering system enables one to diagnose light from 190 nm to 850 nm. Improved spectral sensitivity at lower wavelengths allows for the observation of electron plasma wave scattering using a 4ω probe beam. The spectral range is limited by air attenuation in the UV and photocathode sensitivity in the IR. This extends the peak density from which electron plasma waves can be measured by an order of magnitude ($n_e \approx 2.0 \times 10^{21}$ cm^{-3}) (Fig. 131.34). A high-quality imaging system provides localized measurement of the plasma conditions and reduces the unwanted emission (typically bremsstrahlung and scattering from laser beams other than the probe beam). A localized measurement is obtained by overlapping the image of light scattered from the probe beam ($\sim$60-μm diameter) with a 100-μm-diam pinhole located at the entrance of the spectrometer (Fig. 131.35). When accounting for the magnification of the optical transport system (m = 1.4), light is collected from a 60-μm $\times$ 70-μm $\times$ 70-μm volume (Thomson-scattering volume).

The system consists of a reflective telescope mounted in a ten-inch manipulator (TIM) that collects scattered light and directs it along the TIM-6 line of sight to an instrument cart located approximately 8 m away from the target. A set of Pfund telescopes focus the scattered light into three independently configurable target diagnostics. To measure the ion-acoustic features, a 1-m Czerny–Turner spectrometer (3600 ll/mm grating) is coupled to a Rochester Optical Streak System (ROSS), resulting in a measured spectral resolution of 0.02 nm over a 4-nm spectral range and a pulse-front–limited time resolution

of $\sim$200 ps (Ref. 8). A 0.3-m spectrometer (600 ll/mm grating) coupled to a second ROSS is used to measure the electron plasma features. This system has a measured resolution of 0.5 nm over a 90-nm spectral range and a pulse-front–limited
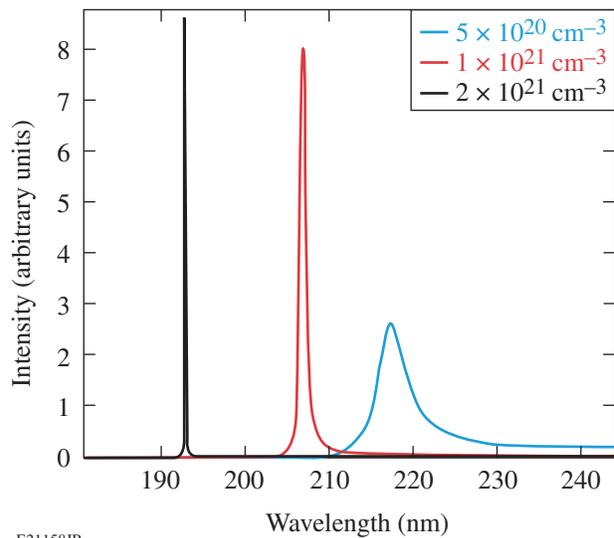
E21158JR

Figure 131.34
A series of calculated Thomson-scattering spectra obtained by assuming a 0.263-μm probe beam is scattered from three densities: 5×10^{20} cm^{-3}, 1×10^{21} cm^{-3}, and 2×10^{21} cm^{-3}. The scattering angle is 60° with an electron temperature of 1.8 keV.
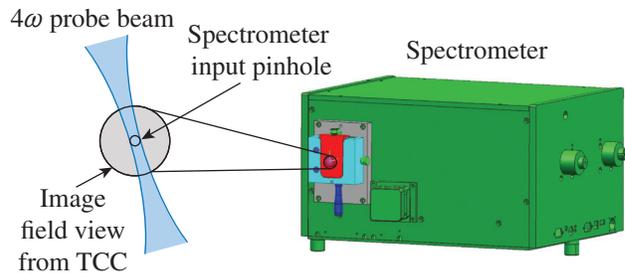
E20937JR

Figure 131.35
The spectrometer entrance slit is replaced with a pinhole assembly. TCC: target chamber center.

time resolution of ~50 ps. An intensified gated charge-coupled–device (CCD) camera captures two-dimensional (2-D) images with a 1.5-mm field of view and a 10-μm spatial resolution in the plasma plane. The minimum gate duration for the camera is 3 ns.

Optical Transport

1. Collection System

The TIM-mounted telescope is based on a Schwarzschild objective that uses two concentric spherical mirrors to provide diffraction-limited imaging across all reflected wavelengths.[9] The telescope was built using an f/10 off-axis segment of a traditional f/1.25 Schwarzschild objective [Fig. 131.36(a)]. The unobstructed configuration allows one to collect light at a higher f number while maintaining the geometry inherent to a Schwarzschild that eliminates third-order aberrations. This allows one to mount the primary and secondary mirrors without a diffraction-inducing support structure common to many reflective objectives. The telescope produces a 19-mm-diam collimated beam.

2. Collimated Transport System

Flat aluminum mirrors are used to direct collected light over an approximately 8-m distance from the OMEGA target chamber to the instrumentation cart. Beamlines for the three separate instruments are produced using uncoated wedge pickoffs or semi-aluminumized beam splitters. Each optical path has provisions to include filtering in the collimated beam to control signal level and spectral throughput.

3. Focusing System

Images are formed for each diagnostic using reflective Pfund telescopes [Fig. 131.36(b)]. Collimated light strikes a flat primary mirror with a central through-hole and is directed toward a concave, spherical secondary mirror. Light reflected

off the secondary mirror is focused back through the hole of the primary mirror, allowing one to align the system on its optical axis. The primary mirror through-hole is counter sunk at a 45° angle to prevent clipping of the focusing beam on the rear surface of the mirror.

The minimum through-hole diameter is determined by the required field angle needed to image the entire Thomson-scattered volume at the desired working f number. The 1-m and 0.3-m systems use a 5-mm through-hole that provides a 350-μm field of view at target chamber center (TCC) with a magnification of 1.4×. Full coupling of the probe beam's waist can be accomplished with a spectrometer input image of 100 μm. Approximately 7% of the overall signal is lost through the hole in the primary mirror.

Optical Performance

Historically, efforts to observe the electron plasma wave features on OMEGA with a 4ω probe beam have been limited by the performance of the existing optical transport.[10] Previously, scattered light was collected using a fused-silica and calcium-fluoride doublet and focused with a Pfund telescope. The rapidly changing index of refraction of the doublet glasses across the deep UV spectrum introduced an 8-mm focal plane shift between focus at 265 nm and 200 nm [Fig. 131.37(a)]. As a result, the detection efficiency of the system drops significantly at wavelengths below 240 nm [Fig. 131.37(b)]. This is a result of a reduction in the signal intensity as the defocused spot size increases and the reappearance of the central through-hole in the Pfund telescope as a far-field image is presented to the spectrometer.

The reflective system has a 100-μm focal shift from 265 nm to 200 nm. The slight chromatic shift is caused by a 3-mm-thick fused-silica blast window located in front of the Schwarzschild
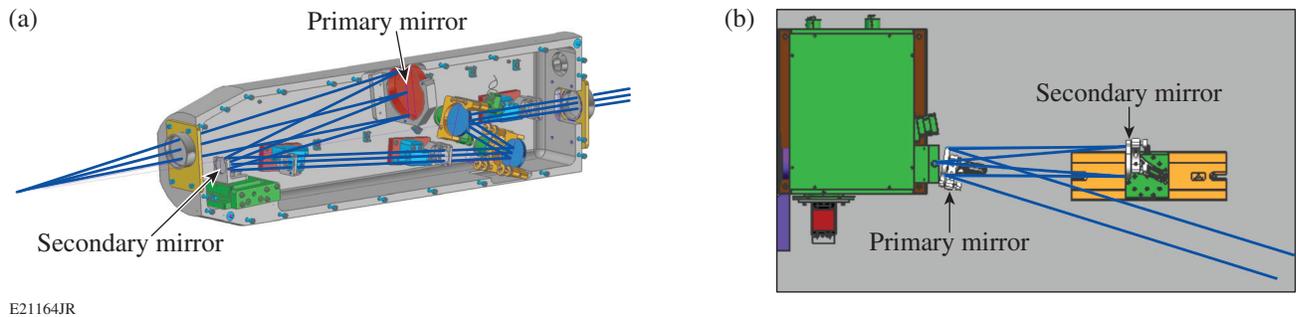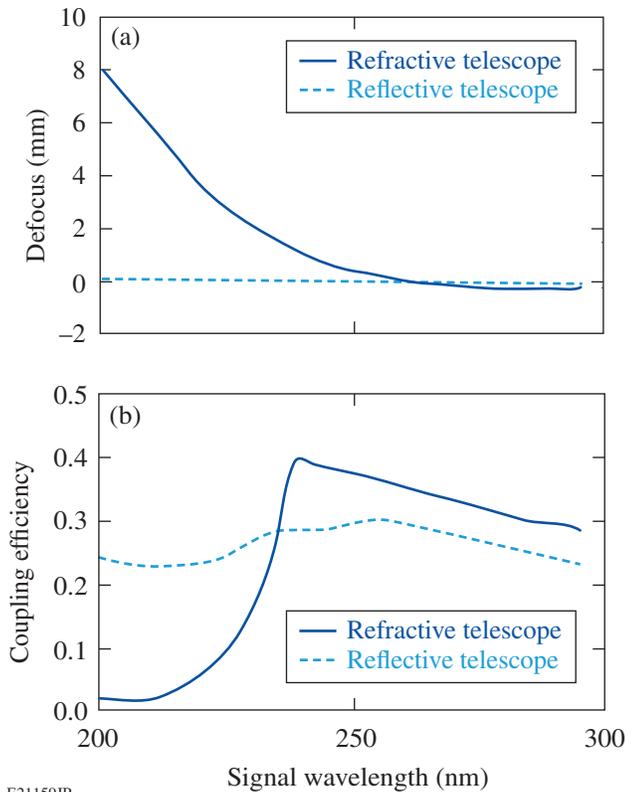

E21164JR

Figure 131.36
(a) An f/10 off-axis section of a Schwarzschild objective is used to collect scattered light. (b) A Pfund telescope focuses the scattered light to the diagnostic.

Figure 131.37

(a) Focal shift of the image plane at the spectrometer input for the refractive Thomson-scattering system. (b) Calculated transmission of an on-axis point source through the 100-μm spectrometer pinhole for the refractive system (solid curve) and the reflective system (dashed curve).

objective used to protect the primary mirror from target debris. The maximum transmission of the reflective system is slightly reduced compared to the refractive system because of the addition of four aluminum mirror elements required to collect and steer scattered light from TCC to the instrument cart. Air attenuation of deep UV signals limits the reflective systems transmission to 190 nm.

Summary

A reflective optical transport system has been designed for the Thomson-scattering system on OMEGA to provide suitable performance from 190 nm to 850 nm. This will enable the operator to perform Thomson-scattering measurements of UV light scattered from electron plasma waves.

REFERENCES

1. D. H. Froula, S. H. Glenzer, N. C. Luhmann, and J. Sheffield, *Plasma Scattering of Electromagnetic Radiation: Theory and Measurement Techniques*, 2nd ed. (Academic Press, Burlington, MA, 2011).

2. S. H. Glenzer *et al.*, Phys. Rev. Lett. **79**, 1277 (1997).

3. A. J. Mackinnon, S. Shiromizu, G. Antonini, J. Auerbach, K. Haney, D. H. Froula, J. Moody, G. Gregori, C. Constantin, C. Sorce, L. Divol, R. L. Griffith, S. Glenzer, J. Satariano, P. K. Whitman, S. N. Locke, E. L. Miller, R. Huff, K. Thorp, W. Armstrong, W. Bahr, W. Seka, G. Pien, J. Mathers, S. Morse, S. Loucks, and S. Stagnitto, Rev. Sci. Instrum. **75**, 3906 (2004).

4. D. H. Froula, J. S. Ross, L. Divol, N. Meezan, A. J. MacKinnon, R. Wallace, and S. H. Glenzer, Phys. Plasmas **13**, 052704 (2006).

5. D. H. Froula, J. S. Ross, L. Divol, and S. H. Glenzer, Rev. Sci. Instrum. **77**, 10E522 (2006).

6. J. L. Ross, S. H. Glenzer, P. Amendt, R. Berger, L. Divol, N. L. Kugland, O. L. Landen, C. Plechaty, B. Remington, D. Ryutov, W. Rozmus, D. H. Froula, G. Fiksel, C. Sorce, Y. Kuramitsu, T. Morita, Y. Sakawa, H. Takabe, R. P. Drake, M. Grosskopf, C. Kuranz, G. Gregori, J. Meinecke, C. D. Murphy, M. Koenig, A. Pelka, A. Ravasio, T. Vinci, E. Liang, R. Presura, A. Spitkovsky, F. Miniati, and H.-S. Park, Phys. Plasmas **19**, 056501 (2012).

7. J. H. Kelly, L. J. Waxer, V. Bagnoud, I. A. Begishev, J. Bromage, B. E. Kruschwitz, T. J. Kessler, S. J. Loucks, D. N. Maywar, R. L. McCrory, D. D. Meyerhofer, S. F. B. Morse, J. B. Oliver, A. L. Rigatti, A. W. Schmid, C. Stoeckl, S. Dalton, L. Folnsbee, M. J. Guardalben, R. Jungquist, J. Puth, M. J. Shoup III, D. Weiner, and J. D. Zuegel, J. Phys. IV France **133**, 75 (2006).

8. A. Visco, R. P. Drake, D. H. Froula, S. H. Glenzer, and B. B. Pollock, Rev. Sci. Instrum. **79**, 10F545 (2008).

9. M. J. Riedl, *Optical Design Fundamentals for Infrared Systems*, 2nd ed., Tutorial Texts in Optical Engineering, Vol. TT48 (SPIE Press, Bellingham, WA, 2001).

10. J. S. Ross, L. Divol, C. Sorce, D. H. Froula, and S. H. Glenzer, J. Inst. **6**, P08004 (2011).

Publications and Conference Presentations

Publications

M. A. Barrios, T. R. Boehly, D. G. Hicks, D. E. Fratanduono, J. H. Eggert, G. W. Collins, and D. D. Meyerhofer, "Precision Equation-of-State Measurements on National Ignition Facility Ablator Materials from 1 to 12 Mbar Using Laser-Driven Shock Waves," J. Appl. Phys. **111**, 093515 (2012).

J. Bromage, C. Dorrer, and R. K. Jungquist, "Temporal Contrast Degradation at the Focus of Ultrafast Pulses from High-Frequency Spectral Phase Modulation," J. Opt. Soc. Am. B **29**, 051125 (2012).

T. Caillaud, O. Landoas, M. Briat, S. Kime, B. Rossé, I. Thfoin, J. L. Bourgade, L. Disdier, V. Yu. Glebov, F. J. Marshall, and T. C. Sangster, "Development of the Large Neutron Imaging System for Inertial Confinement Fusion Experiments," Rev. Sci. Instrum. **83**, 033502 (2012).

D. A. Callahan, N. B. Meezan, S. H. Glenzer, A. J. MacKinnon, L. R. Benedetti, D. K. Bradley, J. R. Celeste, P. M. Celliers, S. N. Dixit, T. Döppner, E. G. Dzentitis, S. Glenn, S. W. Haan, C. A. Haynam, D. G. Hicks, D. E. Hinkel, O. S. Jones, O. L. Landen, R. A. London, A. G. MacPhee, P. A. Michel, J. D. Moody, J. E. Ralph, H. F. Robey, M. D. Rosen, M. B. Schneider, D. J. Strozzi, L. J. Suter, R. P. J. Town, K. Widmann, E. A. Williams, M. J. Edwards, B. J. MacGowan, J. D. Lindl, L. J. Atherton, G. A. Kyrala, J. L. Kline, R. E. Olson, D. Edgell, S. P. Regan, A. Nikroo, H. Wilkins, J. D. Kilkenny, and A. S. Moore, "The Velocity Campaign for Ignition on NIF," Phys. Plasmas **19**, 056305 (2012).

T. J. B. Collins, J. A. Marozas, R. L. McCrory, P. B. Radha, D. R. Harding, P. W. McKenty, R. S. Craxton, A. Shvydky, V. N. Goncharov, S. Skupsky, and J. D. Zuegel, R. Betti, F. J. Marshall, J. A. Delettrez, K. S. Anderson, and D. D. Meyerhofer, "A Polar-Drive–Ignition Design for the National Ignition Facility," Phys. Plasmas **19**, 056308 (2012).

K. Falk, S. P. Regan, J. Vorberger, M. A. Barrios, T. R. Boehly, D. E. Fratanduono, S. H. Glenzer, D. G. Hicks, S. X. Hu, C. D. Murphy, P. B. Radha, S. Rothman, A. P. Jephcoat, J. S. Wark, D. O. Gericke, and G. Gregori, "Self-Consistent Measurement of the Equation of State of Liquid Deuterium," High Energy Density Phys. **8**, 76 (2012).

G. Fiksel, S. X. Hu, V. N. Goncharov, D. D. Meyerhofer, T. C. Sangster, V. A. Smalyuk, B. Yaakobi, M. J. Bonino, and R. Jungquist, "Experimental Reduction of Laser Imprinting and Rayleigh–Taylor Growth in Spherically Compressed, Medium-Z–Doped Plastic Targets," Phys. Plasmas **19**, 062704 (2012).

D. H. Froula, B. Yaakobi, S. X. Hu, P.-Y. Chang, R. S. Craxton, D. H. Edgell, R. Follett, D. T. Michel, J. F. Myatt, W. Seka, R. W. Short, A. A. Solodov, and C. Stoeckl, "Saturation of the Two-Plasmon Decay Instability in Long-Scale-Length Plasmas Relevant to Direct-Drive Inertial Confinement Fusion," Phys. Rev. Lett. **108**, 165003 (2012).

S. H. Glenzer, D. A. Callahan, A. J. MacKinnon, J. L. Kline, G. Grim, E. T. Alger, R. L. Berger, L. A. Bernstein, R. Betti, D. L. Bleuel, T. R. Boehly, D. K. Bradley, S. C. Burkhart, R. Burr, J. A. Caggiano, C. Castro, D. T. Casey, C. Choate, D. S. Clark, P. Celliers, C. J. Cerjan, G. W. Collins, E. L. Dewald, P. DiNicola, J. M. DiNicola, L. Divol, S. Dixit, T. Döppner, R. Dylla-Spears, E. Dzenitis, M. Eckart, G. Erbert, D. Farley, J. Fair, D. Fittinghoff, M. Frank, L. J. A. Frenje, S. Friedrich, D. T. Casey, M. Gatu Johnson, C. Gibson, E. Giraldez, V. Glebov, S. Glenn, N. Guler, S. W. Haan, B. J. Haid, B. A. Hammel, A. V. Hamza, C. A. Haynam, G. M. Heestand, M. Hermann, H. W. Hermann, D. G. Hicks, D. E. Hinkel, J. P. Holder, D. M. Holunda, J. B. Horner, W. W. Hsing, H. Huang, N. Izumi, M. Jackson, O. S. Jones, D. H. Kalantar, R. Kauffman, J. D. Kilkenny, R. K. Kirkwood, J. Klingmann, T. Kohut, J. P. Knauer, J. A. Koch, B. Kozioziemski, G. A.

Kyrala, A. L. Kritcher, J. Kroll, K. La Fortune, L. Lagin, O. L. Landen, D. W. Larson, D. LaTray, R. J. Leeper, S. Le Pape, J. D. Lindl, R. Lowe-Webb, T. Ma, J. McNaney, A. G. MacPhee, T. N. Malsbury, E. Mapoles, C. D. Marshall, N. B. Meezan, F. Merrill, P. Michel, J. D. Moody, A. S. Moore, M. Moran, K. A. Moreno, D. H. Munro, B. R. Nathan, A. Nikroo, R. E. Olson, C. D. Orth, A. E. Pak, P. K. Patel, T. Parham, R. Petrasso, J. E. Ralph, H. Rinderknecht, S. P. Regan, H. F. Robey, J. S. Ross, M. D. Rosen, R. Sacks, J. D. Salmonson, R. Saunders, J. Sater, C. Sangster, M. B. Schneider, F. H. Séguin, M. J. Shaw, B. K. Spears, P. T. Springer, W. Stoeffl, L. J. Suter, C. A. Thomas, R. Tommasini, R. P. J. Town, C. Walters, S. Weaver, S. V. Weber, P. J. Wegner, P. K. Whitman, K. Widmann, C. C. Widmayer, C. H. Wilde, D. C. Wilson, B. Van Wonterghem, B. J. MacGowan, L. J. Atherton, M. J. Edwards, and E. I. Moses, "Cryogenic Thermonuclear Fuel Implosions on the National Ignition Facility," Phys. Plasmas **19**, 056318 (2012).

A. J. Harvey-Thompson, S. V. Lebedev, S. Patankar, S. N. Bland, G. Burdiak, J. P. Chittenden, A. Colaitis, P. De Grouchy, H. W. Doyle, G. N. Hall, E. Khoory, M. Hohenberger, L. Pickworth, F. Suzuki-Vidal, R. A. Smith, J. Skidmore, L. Suttle, and G. F. Swadling, "Optical Thomson Scattering Measurements of Plasma Parameters in the Ablation Stage of Wire Array *Z* Pinches," Phys. Rev. Lett. **108**, 145002 (2012).

M. Hohenberger, P.-Y. Chang, G. Fiksel, J. P. Knauer, D. D. Meyerhofer, R. Betti, F. J. Marshall, F. H. Séguin, and R. D. Petrasso, "Inertial Confinement Fusion Implosions with Imposed Magnetic Field Compression Using the OMEGA Laser," Phys. Plasmas **19**, 056306 (2012).

S. X. Hu, G. Fiksel, V. N. Goncharov, S. Skupsky, D. D. Meyerhofer, and V. A. Smalyuk, "Mitigating Laser Imprint in Direct-Drive Inertial Confinement Fusion Implosions with High-*Z* Dopants," Phys. Rev. Lett. **108**, 195003 (2012).

I. V. Igumenshchev, W. Seka, D. H. Edgell, D. T. Michel, D. H. Froula, V. N. Goncharov, R. S. Craxton, L. Divol, R. Epstein, R. Follett, J. H. Kelly, T. Z. Kosc, A. V. Maximov, R. L. McCrory, D. D. Meyerhofer, P. Michel, J. F. Myatt, T. C. Sangster, A. Shvydky, S. Skupsky, and C. Stoeckl, "Crossed-Beam Energy Transfer in Direct-Drive Implosions," Phys. Plasmas **19**, 056314 (2012).

I. Iñiguez-de-la-Torre, H. Rodilla, J. Mateos, T. González, H. Irie, and R. Sobolewski, "Monte Carlo Studies of the Intrinsic Time-Domain Response of Nanoscale Three-Branch Junctions," J. Appl. Phys. **111**, 084511 (2012).

O. S. Jones, C. J. Cerjan, M. M. Marinak, J. L. Milovich, H. F. Robey, P. T. Springer, L. R. Benedetti, D. L. Bleuel, E. J. Bond, D. K. Bradley, D. A. Callahan, J. A. Caggiano, P. M. Celliers, D. S. Clark, S. M. Dixit, T. Doppner, R. J. Dylla-Spears, E. G. Dzentitis, D. R. Farley, S. M. Glenn, S. H. Glenzer, S. W. Haan, B. J. Haid, C. A. Haynam, D. G. Hicks, B. J. Kozioziemski, K. N. LaFortune, O. L. Landen, E. R. Mapoles, A. J. MacKinnon, J. M. McNaney, N. B. Meezan, P. A. Michel, J. D. Moody, M. J. Moran, D. H. Munro, M. V. Patel, T. G. Parham, J. D. Sater, S. M. Sepke, B. K. Spears, R. P. J. Town, S. V. Weber, K. Widmann, C. C. Widmayer, E. A. Williams, L. J. Atherton, M. J. Edwards, J. D. Lindl, B. J. MacGowan, L. J. Suter, R. E. Olson, H. W. Herrmann, J. L. Kline, G. A. Kyrala, D. C. Wilson, J. Frenje, T. R. Boehly, V. Glebov, J. P. Knauer, A. Nikroo, H. Wilkens, and J. D. Kilkenny, "A High-Resolution Integrated Model of the National Ignition Campaign Cryogenic Layered Experiments," Phys. Plasmas **19**, 056315 (2012).

Y. Kim, J. M. Mack, H. W. Herrmann, C. S. Young, G. M. Hale, S. Caldwell, N. M. Hoffman, S. C. Evans, T. J. Sedillo, A. McEvoy, J. Langenbrunner, H. H. Hsu, M. A. Huff, S. Batha, C. J. Horsfield, M. S. Rubery, W. J. Garbett, W. Stoeffl, E. Grafil, L. Bernstein, J. A. Church, D. B. Sayre, M. J. Rosenberg, C. Waugh, H. G. Rinderknecht, M. Gatu Johnson, A. B. Zylstra, J. A. Frenje, D. T. Casey, R. D. Petrasso, E. K. Miller, V. Yu Glebov, C. Stoeckl, and T. C. Sangster, "D-T Gamma-to-Neutron Branching Ratio Determined from Inertial Confinement Fusion Plasmas," Phys. Plasmas **19**, 056313 (2012).

Y. Kim, J. M. Mack, H. W. Herrmann, C. S. Young, G. M. Hale, S. Caldwell, N. M. Hoffman, S. C. Evans, T. J. Sedillo, A. McEvoy, J. Langenbrunner, H. H. Hsu, M. A. Huff, S. Batha, C. J. Horsfield, M. S. Rubery, W. J. Garbett, W. Stoeffl, E. Grafil, L. Bernstein, J. A. Church, D. B. Sayre, M. J. Rosenberg, C. Waugh, H. G. Rinderknecht, M. Gatu Johnson, A. B. Zylstra, J. A. Frenje, D. T. Casey, R. D. Petrasso, E. K. Miller, V. Yu Glebov, C. Stoeckl, and T. C. Sangster, "Determination of the Deuterium-Tritium Branching Ratio Based on Inertial Confinement Fusion Implosions," Phys. Rev. C **85**, 061601(R) (2012).

A. J. Mackinnon, J. L. Kline, S. N. Dixit, S. H. Glenzer, M. J. Edwards, D. A. Callahan, N. B. Meezan, S. W. Haan, J. D. Kilkenny, T. Döppner, D. R. Farley, J. D. Moody, J. E. Ralph, B. J. MacGowan, O. L. Landen, H. F. Robey, T. R. Boehly, P. M. Celliers, J. H. Eggert, K. Krauter, G. Frieders, G. F. Ross, D. G. Hicks, R. E. Olson, S. V. Weber, B. K. Spears, J. D. Salmonsen,

P. Michel, L. Divol, B. Hammel, C. A. Thomas, D. S. Clark, O. S. Jones, P. T. Springer, C. J. Cerjan, G. W. Collins, V. Y. Glebov, J. P. Knauer, C. Sangster, C. Stoeckl, P. McKenty, J. M. McNaney, R. J. Leeper, C. L. Ruiz, G. W. Cooper, A. G. Nelson, G. G. A. Chandler, K. D. Hahn, M. J. Moran, M. B. Schneider, N. E. Palmer, R. M. Bionta, E. P. Hartouni, S. LePape, P. K. Patel, N. Izumi, R. Tommasini, E. J. Bond, J. A. Caggiano, R. Hatarik, G. P. Grim, F. E. Merrill, D. N. Fittinghoff, N. Guler, O. Drury, D. C. Wilson, H. W. Herrmann, W. Stoeffl, D. T. Casey, M. G. Johnson, J. A. Frenje, R. D. Petrasso, A. Zylestra, H. Rinderknecht, D. H. Kalantar, J. M. Dzenitis, P. Di Nicola, D. C. Eder, W. H. Courdin, G. Gururangan, S. C. Burkhart, S. Friedrich, D. L. Blueuel, A. Bernstein, M. J. Eckart, D. H. Munro, S. P. Hatchett, A. G. Macphee, D. H. Edgell, D. K. Bradley, P. M. Bell, S. M. Glenn, N. Simanovskaia, M. A. Barrios, R. Benedetti, G. A. Kyrala, R. P. J. Town, E. L. Dewald, J. L. Milovich, K. Widmann, A. S. Moore, G. LaCaille, S. P. Regan, L. J. Suter, B. Felker, R. C. Ashabranner, M. C. Jackson, R. Prasad, M. J. Richardson, T. R. Kohut, P. S. Datte, G. W. Krauter, J. J. Klingman, R. F. Burr, T. A. Land, M. R. Hermann, D. A. Latray, R. L. Saunders, S. Weaver, S. J. Cohen, L. Berzins, S. G. Brass, E. S. Palma, R. R. Lowe-Webb, G. N. McHalle, P. A. Arnold, L. J. Lagin, C. D. Marshall, G. K. Brunton, D. G. Mathisen, R. D. Wood, J. R. Cox, R. B. Ehrlich, K. M. Knittel, M. W. Bowers, R. A. Zacharias, B. K. Young, J. P. Holder, J. R. Kimbrough, T. Ma, K. N. La Fortune, C. C. Widmayer, M. J. Shaw, G. V. Erbert, K. S. Jancaitis, J. M. DiNicola, C. Orth, G. Heestand, R. Kirkwood, C. Haynam, P. J. Wegner, P. K. Whitman, A. Hamza, E. G. Dzenitis, R. J. Wallace, S. D. Bhandarkar, T. G. Parham, R. Dylla-Spears, E. R. Mapoles, B. J. Kozioziemski, J. D. Sater, C. F. Walters, B. J. Haid, J. Fair, A. Nikroo, E. Giraldez, K. Moreno, B. Vanwonterghem, R. L. Kauffman, S. Batha, D. W. Larson, R. J. Fortner, D. H. Schneider, J. D. Lindl, R. W. Patterson, L. J. Atherton, and E. I. Moses, "Assembly of High-Areal-Density Deuterium-Tritium Fuel from Indirectly Driven Cryogenic Implosions," Phys. Rev. Lett. **108**, 215005 (2012).

M. J. E. Manuel, C. K. Li, F. H. Séguin, J. Frenje, D. T. Casey, R. D. Petrasso, S. X. Hu, R. Betti, J. D. Hager, D. D. Meyerhofer, and V. A. Smalyuk, Phys. Rev. Lett. **108**, 255006 (2012).

A. V. Okishev, "Highly Efficient Room-Temperature Yb:YAG Ceramic Laser and Regenerative Amplifier," Opt. Lett. **37**, 1199 (2012).

S. P. Regan, R. Epstein, B. A. Hammel, L. J. Suter, J. Ralph, H. Scott, M. A. Barrios, D. K. Bradley, D. A. Callahan, C. J. Cerjan, G. W. Collins, S. N. Dixit, T. Doeppner, M. J. Edwards, D. R. Farley, S. Glenn, S. H. Glenzer, I. E. Golovkin, S. W. Haan, A. Hamza, D. G. Hicks, N. Izumi, J. D. Kilkenny, J. L. Kline, G. A. Kyrala, O. L. Landen, T. Ma, J. J. MacFarlane, R. C. Mancini, R. L. McCrory, N. B. Meezan, D. D. Meyerhofer, A. Nikroo, K. J. Peterson, T. C. Sangster, P. Springer, and R. P. J. Town, "Hot-Spot Mix in Ignition-Scale Implosions on the NIF," Phys. Plasmas **19**, 056307 (2012).

H. F. Robey, P. M. Celliers, J. L. Kline, A. J. Mackinnon, T. R. Boehly, O. L. Landen, J. H. Eggert, D. Hicks, S. Le Pape, D. R. Farley, M.W. Bowers, K. G. Krauter, D. H. Munro, O. S. Jones, J. L. Milovich, D. Clark, B. K. Spears, R. P. J. Town, S. W. Haan, S. Dixit, M. B. Schneider, E. L. Dewald, K. Widmann, J. D. Moody, T. D. Döppner, H. B. Radousky, A. Nikroo, J. J. Kroll, A.V. Hamza, J. B. Horner, S. D. Bhandarkar, E. Dzenitis, E. Alger, E. Giraldez, C. Castro, K. Moreno, C. Haynam, K. N. LaFortune, C. Widmayer, M. Shaw, K. Jancaitis, T. Parham, D. M. Holunga, C. F. Walters, B. Haid, T. Malsbury, D. Trummer, K. R. Coffee, B. Burr, L. V. Berzins, C. Choate, S. J. Brereton, S. Azevedo, H. Chandrasekaran, S. Glenzer, J. A. Caggiano, J. P. Knauer, J. A. Frenje, D. T. Casey, M. Gatu Johnson, F. H. Séguin, B. K. Young, M. J. Edwards, B. M. Van Wonterghem, J. Kilkenny, B. J. MacGowan, J. Atherton, J. D. Lindl, D. D. Meyerhofer, and E. Moses, "Precision Shock Tuning on the National Ignition Facility," Phys. Rev. Lett. **108**, 215004 (2012).

J. E. Schoenly, W. Seka, J. D. B. Featherstone, and P. Rechmann, "Near-UV Laser Treatment of Extrinsic Dental Enamel Stains," Lasers Surg. Med. **44**, 339 (2012).

A. J. Visco, R. P. Drake, S. H. Glenzer, T. Döppner, G. Gregori, D. H. Froula, and M. J. Grosskopf, "Measurement of Radiative Shock Properties by X-Ray Thomson Scattering," Phys. Rev. Lett. **108**, 145001 (2012).

A. B. Zylstra, J. A. Frenje, F. H. Séguin, M. J. Rosenberg, H. G. Rinderknecht, M. Gatu Johnson, D. T. Casey, N. Sinenian, M. J.-E. Manuel, C. J. Waugh, H. W. Sio, C. K. Li, R. D. Petrasso, S. Friedrich, K. Knittel, R. Bionta, M. McKernan, D. Callahan, G. W. Collins, E. Dewald, T. Döppner, M. J. Edwards, S. Glenzer, D. G. Hicks, O. L. Landen, R. London, A. Mackinnon, N. Meezan, R. R. Prasad, J. Ralph, M. Richardson, J. R. Rygg, S. Sepke, S. Weber, R. Zacharias, E. Moses, J. Kilkenny, A. Nikroo, T. C. Sangster, V. Glebov, C. Stoeckl, R. Olson, R. J. Leeper, J. Kline, G. Kyrala, and D. Wilson, "Charged-Particle Spectroscopy for Diagnosing Shock ρR and Strength in NIF Implosions," Rev. Sci. Instrum. **83**, 10D901 (2012).

Forthcoming Publications

B. Beeman, A. G. MacPhee, J. R. Kimbrough, G. A. Lacaille, M. A. Barrios, J. Emig, J. R. Hunter, E. K. Miller, and W. R. Donaldson, "Mach–Zehnder Modulator Performance Using the Comet Laser Facility and Implications for Use on NIF," to be published in the Proceedings of SPIE.

J. Bromage, C. Dorrer, M. Millecchia, J. Bunkenburg, R. Jungquist, and J. D. Zuegel, "A Front End for Ultra-Intense OPCPA," to be published in AIP Conference Proceedings.

D. T. Casey, J. A. Frenje, M. Gatu Johnson, M. J.-E. Manuel, N. Sinenian, A. B. Zylstra, F. H. Séguin, C. K. Li, R. D. Petrasso, V. Yu Glebov, P. B. Radha, D. D. Meyerhofer, T. C. Sangster, D. P. McNabb, P. A. Amendt, R. N. Boyd, S. P. Hatchett, S. Quaglioni, J. R. Rygg, I. J. Thompson, A. D. Bacher, H. W. Herrmann, and Y. H. Kim, "Measurements of the $T(t,2n)^4$He Neutron Spectrum at Low Reactant Energies from Inertial Confinement Implosions," to be published in Physical Review Letters.

G. Fiksel, F. J. Marshall, C. Mileham, and C. Stoeckl, "Spatial Resolution of Fuji BAS TR and SR Imaging," to be published in Review of Scientific Instruments.

L. Gao, P. M. Nilson, I. V. Igumenshchev, J. R. Davies, S. X. Hu, C. Stoeckl, M. G. Haines, D. H. Froula, R. Betti, and D. D. Meyerhofer, "Magnetic-Field Generation by Rayleigh–Taylor Instability in Laser-Driven Planar Plastic Targets," to be published in Physical Review Letters.

R. Q. Gram, A. She, R. S. Craxton, and D. R. Harding, "Thermal Conductivity of Solid Deuterium by the 3ω Method," to be published in Journal of Applied Physics.

J. D. Hager, V. A. Smalyuk, S. X. Hu, J. P. Knauer, D. D. Meyerhofer, and T. C. Sangster, "Study of Rayleigh–Taylor Growth in Directly Driven Cryogenic Deuterium Targets," to be published in Physics of Plasmas.

S. X. Hu, V. N. Goncharov, and S. Skupsky, "Burning Plasmas with Ultrashort X-Ray Flashing," to be published in Physics of Plasmas.

M. Mikulics, J. Zhang, J. Serafini, R. Adam, D. Grützmacher, and R. Sobolewski, "Subpicosecond Electron-Hole Recombination Time and Terahertz-Bandwidth Photoresponse in Freestanding GaAs Epitaxial Mesoscopic Structures," to be published in Applied Physics Letters.

J. B. Oliver, P. Kupinski, A. L. Rigatti, A. W. Schmid, J. C. Lambropoulos, S. Papernov, A. Kozlov, S. Smith, and R. D. Hand, "Stress Compensation in Hafnia/Silica Optical Coatings by Inclusion of Alumina Layers," to be published in Optics Express.

P. B. Radha, J. A. Marozas, F. J. Marshall, A. Shvydky, T. J. B. Collins, V. N. Goncharov, R. L. McCrory, P. W. McKenty, D. D. Meyerhofer, T. C. Sangster, and S. Skupsky, "OMEGA Polar-Drive Target Designs," to be published in Physics of Plasmas.

H. G. Rinderknecht, M. Gatu Johnson, A. B. Zylstra, N. Sinenian, M. J. Rosenberg, J. A. Frenje, C. J. Waugh, C. K. Li, F. H. Séguin, R. D. Petrasso, J. R. Rygg, J. R. Kimbrough, A. MacPhee, G. W. Collins, D. Hicks, A. Mackinnon, P. Bell, R. Bionta, T. Clancy, R. Zacharias, T. Döppner, H. S. Park, S. LePape, O. Landen, N. Meezan, E. I. Moses, V. U. Glebov, C. Stoeckl, T. C. Sangster, R. Olson, J. Kline, and J. Kilkenny, "A Novel Particle Time of Flight Diagnostic for Measurements of Shock- and Compression-Bang Times in D^{3}He and DT Implosions at the NIF," to be published in Review of Scientific Instruments.

Conference Presentations

The following presentations were made at the 2012 Materials Research Society Spring Meeting and Exhibit, San Francisco, CA, 9–13 April 2012:

K. Mehrotra, H. P. Howard, S. D. Jacobs, and J. C. Lambropoulos, "Mechanical Characterization of 'Blister' Defects on Optical Oxide Multilayers Using Nanoindentation."

K. Mehrotra, H. P. Howard, S. D. Jacobs, and J. C. Lambropoulos, "Nanoindentation Probing of High-Aspect-Ratio Pillar Structures on Optical Multilayer Dielectric Diffraction Gratings."

The following presentations were made at the Omega Laser Facility Users Group Workshop, Rochester, NY, 25–27 April 2012:

D. Canning, "Omega EP Facility Update and Progress on OLUG Recommendations."

G. Fiksel, P.-Y. Chang, M. Hohenberger, R. Betti, M. J. Shoup III, C. Taylor, T. Duffy, D. Lonobile, and W. Bittle, "Developing Magnetic Platforms for Inertial Confinement Fusion and Basic High-Energy-Density Science."

D. H. Froula, R. Boni, M. Bedzyk, R. Brown, R. S. Craxton, T. Duffy, F. Ehrne, S. Ivancic, R. Jungquist, N. Kugland, J. Puth, R. G. Roides, M. C. Rushford, W. Seka, M. J. Shoup III, W. Theobald, and D. Weiner, "Optical Diagnostic Suite (Schlieren, Interferometry, and Grid Refractometry) on OMEGA EP Using a 10-ps, 263-nm Probe Beam."

R. Jungquist, "Laser Retroreflected and Reflected Light Management."

J. Katz, R. Boni, D. Froula, G. Gates, A. Nauss, J. Szczepanski, M. Shoup, and T. Agliata, "OMEGA Thomson-Scattering System Upgrade."

J. Kwiatkowski, S. Stagnitto, S. F. B. Morse, M. Labuzeta, and V. Guiliano, "Characterizing Debris-Shield Transmission Degradation and Estimating On-Target Energy."

S. F. B Morse, "Omega Facility Updates: Progress on OLUG Recommendations."

G. Pien and J. Puth, "Omega Experimental Systems Performance and Improvements Since OLUG 2011."

S. P. Regan, G. Gregori, P. B. Radha, S. X. Hu, T. R. Boehly, B. Crowley, S. H. Glenzer, O. L. Landen, D. O. Gericke, T. Doeppner, D. D. Meyerhofer, C. D. Murphy, T. C. Sangster, and J. Vorberger, "X-Ray Thomson Scattering: An Incisive Probe for Warm, Dense Matter."

W. T. Shmayda, "Isotope Separation System and Gas Chromatograph Support Non-Standard Fills."

C. Sorce, M. Millecchia, D. Mastrosimone, A. Sorce, J. Katz, S. Ingraham, A. Pruyne, R. Bahr, D. Hassett, and D. Guy, "Omega Facility Diagnostic Highlights."

S. Stagnitto, W. R. Donaldson, E. Hill, M. Labuzeta, and M. Millecchia, "OMEGA Performance Metrics and Status Update on OLUG Recommendations."

C. Stoeckl, G. Fiksel, R. Jungquist, P. M. Nilson, and W. Theobald, "Spherical Crystal X-Ray Imaging for OMEGA and OMEGA EP."

———————

The following presentations were made at the 19th Topical Conference on High-Temperature Plasma Diagnostics, Monterey, CA, 6–10 May 2012:

M. A. Barrios, A. MacPhee, S. P. Regan, J. Kimbrough, S. R. Nagel, L. R. Benedetti, S. F. Khan, D. Bradley, P. Bell, D. H. Edgell, and G. W. Collins, "X-Ray Bang-Time Measurements at the National Ignition Facility (NIF) Using a Polar Diamond Detector."

W. R. Donaldson, C. Zhao, L. Ji, R. G. Roides, K. Miller, and B. Beeman, "A Single-Shot, Multiwavelength Electro-Optic Data-Acquisition System for ICF Applications" (invited).

D. H. Edgell, A. MacPhee, D. K. Bradley, E. Bond, S. Burns, J. Celeste, M. J. Eckart, V. Yu. Glebov, D. S. Hey, G. Lacaille, J. D. Kilkenny, J. R. Kimbrough, A. J. Mackinnon, J. Magoon, J. Parker, T. C. Sangster, M. J. Shoup III, C. Stoeckl, and T. Thomas, "South Pole Bang-Time Diagnostic on the NIF."

C. J. Forrest, V. Yu. Glebov, V. N. Goncharov, A. Pruyne, J. P. Knauer, P. B. Radha, M. Romanofsky, T. C. Sangster, M. J. Shoup III, C. Stoeckl, D. T. Casey, M. Gatu-Johnson, and S. Gardner, "High-Resolution Spectroscopy Used to Measure ICF Neutron Spectra on OMEGA."

D. H. Froula, R. Boni, M. Bedzyk, R. Brown, R. S. Craxton, T. Duffy, F. Ehrne, S. Ivancic, R. Jungquist, N. Kugland, J. Puth, R. G. Roides, M. C. Rushford, W. Seka, M. J. Shoup III, W. Theobald, and D. Weiner, "Optical Diagnostic Suite (Schlieren, Interferometry, and Grid-Image Refractometry) on OMEGA EP Using a 10-ps, 263-nm Probe Beam."

V. Yu. Glebov, C. Forrest, J. P. Knauer, A. Pruyne, M. Romanofsky, T. C. Sangster, M. J. Shoup III, C. Stoeckl, J. A. Caggiano, M. L. Carman, T. J. Clancy, R. Hatarik, J. McNaney, and N. P. Zautseva, "Testing a New NIF Neutron Time-of-Flight Detector with a Bibenzyl Scintillator on OMEGA."

J. Katz, R. Boni, M. J. Shoup III, R. Follett, and D. H Froula, "A Reflective Optical Transport for Streaked Thomson Scattering and Gated Imaging on OMEGA."

J. P. Knauer, V. Yu. Glebov, C. Forrest, C. Stoeckl, T. C. Sangster, D. D. Meyerhofer, J. A. Caggiano, M. J. Moran, R. Hatarik, J. M. McNaney, S. Friedrich, E. J. Bond, M. J. Eckart, S. J. Padalino, and J. D. Kilkenny, "Neutron Spectra from 1 to 15 MeV Measured with Time-of-Flight Detectors at the National Ignition Facility."

F. J. Marshall, "Compact Kirkpatrick–Baez Microscope Mirrors for Imaging Laser–Plasma X-Ray Emission."

D. T. Michel, C. Sorce, R. Epstein, N. Whiting, I. V. Igumenshchev, R. Jungquist, and D. H. Froula, "Shell-Trajectory Measurements from Direct-Drive Experiments."

M. Millecchia, S. P. Regan, C. Sorce, R. E. Bahr, C. M. Romanofsky, and "Streaked X-Ray Spectrometer (SXS) Having a Discrete Selection of Bragg Geometries for Omega."

P. M. Nilson, C. Stoeckl, G. Fiksel, P. A. Jaanimagi, C. Mileham, W. Theobald, J. R. Davies, J. F. Myatt, A. A. Solodov, D. H. Froula, R. Betti, and D. D. Meyerhofer, "Streaked X-Ray Imaging of Ultrafast Ionization Waves Inside a Metal."

C. Stoeckl, J. A. Delettrez, G. Fiksel, D. Guy, R. Jungquist, C. Mileham, P. M. Nilson, T. C. Sangster, M. J. Shoup III, and W. Theobald, "Soft X-Ray Backlighting of Direct-Drive Implosions Using a Spherical Crystal Imager on OMEGA."

———

The following presentations were made at CLEO 2012, San Jose, CA, 6–11 May 2012:

J. Bromage, C. Dorrer, and R. K. Jungquist, "Temporal Contrast Degradation at the Focus of Ultrashort Pulses from High-Frequency Spectral Phase Noise."

J. Bromage, C. Dorrer, M. Millecchia, J. Bunkenburg, R. Jungquist, and J. D. Zuegel, "A Front End for Ultra-Intense OPCPA."

J. Bromage, M. Millecchia, J. Bunkenburg, R. K. Jungquist, C. Dorrer, and J. D. Zuegel, "A Cylindrical Öffner Stretcher for Reduced Chromatic Aberrations and Improved Temporal Contrast."

C. Dorrer, "Broadband Operation of High-Damage-Threshold Phase and Polarization Binary Beam Shapers."

C. Dorrer, A. V. Okishev, R. G. Roides, R. Cuffney, W. Bittle, and J. D. Zuegel, "Fiber Front End for an OMEGA EP Demonstration of Beam-Smoothing Techniques for NIF Polar-Drive Ignition."

J. Qiao, P. A. Jaanimagi, R. Boni, J. Bromage, and E. Hill, "Beam-Homogenization and Space-Charge–Broadening Calibration for Accurately Measuring High-Intensity Laser Pulses Using a High-Speed Streak Camera."

M. Statt, M. Vargas, J. B. Oliver, S. H. Chen, K. L. Marshall, and C. Dorrer, "High-Damage-Threshold Components for Radially and Azimuthally Polarized Beam Generation."

R. Xin and J. D. Zuegel, "A Negative-Feedback-Stabilization System for an All-Fiber Regenerative Amplifier."

———

The following presentations were made at the 20th Target Fabrication Meeting, Santa Fe, NM, 20–24 May 2012:

Z. Bei, G. Randall, T. B. Jones, and D. R. Harding, "Implementation of Dielectrophoretic Droplet Centering in a Miniaturized Centering Cell for ICF Foam Capsule."

M. J. Bonino, F. J. Marshall, D. H. Froula, S. P. Regan, D. Turner, D. R. Harding, S. G. Noyes, J. Fooks, and E. Giraldez, "Overview of the Requirements and Construction of Targets for Experiments on OMEGA and OMEGA EP."

R. Q. Gram, D. R. Harding, and T. B. Jones, "Dielectrophoresis of Liquid Deuterium for IFE Target Filling."

D. R. Harding, M. D. Wittman, and D. H. Edgell, "Considerations and Requirements for Providing Cryogenic Targets for Direct-Drive Inertial Fusion Implosions at the National Ignition Facility."

W. T. Shmayda, D. R. Harding, M. J. Bonino, V. Versteeg, A. Greenwood, and M. Farrel, "Mitigating Defects on Cryotargets."

D. Turner, M. J. Bonino, D. R. Harding, S. G. Noyes, and B. Rice, "Properties and Performance of Target Mounts for Cryogenic Experiments on OMEGA."

———

S. X. Hu, V. N. Goncharov, S. Skupsky, L. A. Collins, M. J. N. Dijokap, A. F. Starace, and B. I. Schneider, "Probing Ultrafast Processes in Intense Laser–Matter Interactions," presented at the 43rd Annual APS Division of Atomic, Molecular, and Optical Physics Meeting, Anaheim, CA, 4–8 June 2012.

––––––––––

The following presentations were made at the OSA Topical Meeting on Optical Fabrication and Testing, Monterey, CA, 24–28 June 2012:

H. P. Howard, J. C. Lambropoulos, and S. D. Jacobs, "Dependence of Thermal Stresses on Substrate Thickness During Wet Processing of Large Coated Optics."

J.C. Lambropoulos, K. Mehrotra, H. P. Howard, and S. D. Jacobs, "Glass Ductility and Fracture at the 50- to 100-nm Scale."

––––––––––

The following presentations were made at the 42nd Annual Anomalous Absorption Conference, Key West, FL, 25–29 June 2012:

D. H. Edgell, P. B. Radha, D. H. Froula, V. N. Goncharov, I. V. Igumenshchev, J. F. Myatt, and W. Seka, "Mitigation of Cross-Beam Energy Transfer in Polar-Drive Implosions."

R. K. Follett, D. T. Michel, J. F. Myatt, S. X. Hu, B. Yaakobi, and D. H. Froula, "Thomson-Scattering Measurements of Ion-Acoustic Wave Amplitudes Driven by the Two-Plasmon Decay."

D. H. Froula, I. V. Igumenshchev, D. T. Michel, D. H. Edgell, R. Follett, V. Yu. Glebov, V. N. Goncharov, J. Marozas, P. B. Radha, W. Seka, C. Sorce, and C. Stoeckl, "Mitigation of Cross-Beam Energy Transfer in Direct-Drive Plasmas."

L. Gao, P. M. Nilson, I. V. Igumenshchev, J. R. Davies, S. X. Hu, C. Stoeckl, M. G. Haines, D. H. Froula, R. Betti, and D. D. Meyerhofer, "Magnetohydrodynamic Effects in Ablatively Driven High-Energy-Density System Experiments."

S. X. Hu, D. H. Edgell, D. H. Froula, V. N. Goncharov, D. T. Michel, S. Skupsky, and B. Yaakobi, "Analyses of Long-Scale-Length Plasma Experiments with Different Ablator Materials on the OMEGA EP Laser System."

A. V. Maximov, J. F Myatt, R. W Short, I. V. Igumenshchev, D. H. Edgell, and W. Seka, "Interaction of Multiple Laser Beams via Common Waves and Beam Energy Transfer."

D. T. Michel, A. V. Maximov, B. Yaakobi, S. X. Hu, J. F. Myatt, A. A. Solodov, R. W. Short, and D. H. Froula, "Experimental Validation of the Two-Plasmon-Decay Common-Wave Process."

J. F. Myatt, J. Zhang, V. N. Goncharov, A. V. Maximov, R. W. Short, D. F. DuBois, D. A. Russell, and H. X. Vu, "The Mitigating Effect of Wave Dissipation on Hot-Electron Generation Caused by the Two-Plasmon Decay in Inhomogeneous Plasmas."

D. A. Russell, H. X. Vu, D. F. DuBois, and J. F. Myatt, "Two-Plasmon-Decay Turbulence Driven by the Shared-Wave Triad of Two Crossed Beams."

W. Seka, D. H. Edgell, D. H. Froula, J. Katz, J. F. Myatt, J. Zhang, R. W. Short, T. D. Michel, A. V. Maximov, and V. N. Goncharov, "Half-Integer Harmonic Images and Spectra Point Toward Localized, Multibeam Two-Plasmon Decay."

R. W. Short, J. Myatt, A. Maximov, T. Michel, and D. Froula, "The Effects of Beam Polarization on Convective and Absolute Two-Plasmon Decay Driven by Multiple Laser Beams."

A. A. Solodov, K. S. Anderson, W. Theobald, A. Shvydky, R. Betti, J. F. Myatt, and C. Stoeckl, "Simulations of Cone-in-Shell Targets for Integrated Fast-Ignition Experiments on OMEGA."

H. X. Vu, D. Russell, D. F. DuBois, and J. F. Myatt, "Hot-Electron Generation by 'Cavitating' Langmuir Turbulence in the Nonlinear Stage of the Two Plasmon Decay Instability."

––––––––––

A. V. Okishev, C. Dorrer, B. E. Kruschwitz, J. H. Kelly, E. Hill, A. Consentino, G. Balonek, J. A. Marozas, M. Hohenberger, A. Shvydky, R. G. Roides, R. Cuffney, W. Bittle, and J. D. Zuegel, "Multifrequency Smoothing by Spectral Dispersion on OMEGA EP for NIF Polar-Drive Implosions," presented at Laser Optics 2012, St. Petersburg, Russia, 25–29 June 2012 (invited).